Okinawa Institute of Science and Technology Graduate University

Energy Materials and Surface Sciences Unit

Thesis submitted for the degree

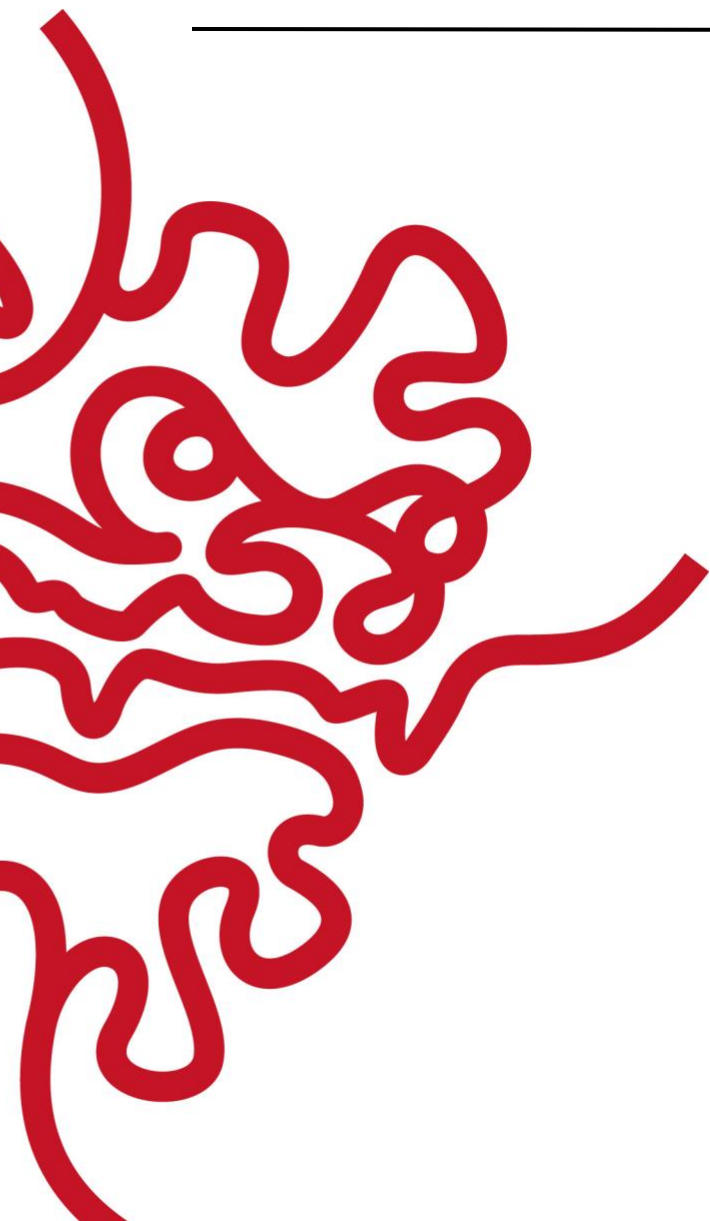**Doctor of Philosophy**

Surface Science Studies of Perovskite Solar Cells: Spiro-MeOTAD Hole Transport Material and Perovskite Absorber

by

Zafer Hawash

Supervisor: **Prof. Yabing Qi**

October, 2017

Declaration of Original and Sole Authorship

I, Zafer Hawash, declare that this thesis entitled "**Surface Science Studies of Perovskite Solar Cells: Spiro-MeOTAD Hole Transport Material and Perovskite Absorber**" and the data presented in it are original and my own work.

I confirm that:

- No part of this work has previously been submitted for a degree at this or any other university.
- References to the work of others have been clearly acknowledged. Quotations from the work of others have been clearly indicated, and attributed to them.
- In cases where others have contributed to part of this work, such contribution has been clearly acknowledged and distinguished from my own work.
- The work presented in this dissertation was presented and published as following:

Publications:

[4] Hawash, Z.†; Ono, L. K.†; Qi, Y. B.,* Recent Advances in Spiro-MeOTAD Hole Transport Material and Its Applications in Organic-inorganic Halide Perovskite Solar Cells. *Adv. Mater. Interfaces,* 2017. (Invited review article, accepted)

[3] Hawash, Z.; Ono, L. K.; Raga, S. R.; Son, D.Y.; Park, N.G.;* Qi, Y. B.,* Interfacial Modification of Perovskite Solar Cells Using an Ultrathin MAI Layer Leads to Enhanced Energy Level Alignment, Efficiencies, and Reproducibility, *J. Phys. Chem. Lett.* 2017, 8 (17), 3947.

[2] <u>Hawash, Z</u>; Ono, L. K.; Qi, Y. B.,* Moisture and Oxygen Enhance Conductivity of LiTFSI-Doped Spiro-MeOTAD Hole Transport Layer in Perovskite Solar Cells. *Adv. Mater. Interfaces* 2016, 3, 1600117.

[1] <u>Hawash, Z.</u>; Ono, L. K.; Raga, S. R.; Lee, M. V.; Qi, Y. B.,* Air-Exposure Induced Dopant Redistribution and Energy Level Shifts in Spin-Coated Spiro-MeOTAD Films. *Chem. Mater.* 2015, 27, 562.

Conferences:

[6] Feb. 2017: **Poster presentation**, <u>Hawash, Z.</u>; Ono, L. K.; Raga, S. R.; Lee, M. V.; Qi, Y. B.,* "*Enhancement of Electrical and Electronic Properties of LiTFSI Doped Spiro-MeOTAD Hole Transport Layer upon Different Environmental Conditions*", Asia-Pacific Hybrid and Organic Photovoltaics (AP-HOPV17), Yokohama-shi, Japan.

[5] Nov. 2016: **Oral presentation**, <u>Hawash, Z.</u>; Ono, L. K.; Qi, Y. B.,* "*The Effects of Ambient Exposure on Charge Transport Properties of LiTFSI Doped Spiro-MeOTAD HTL in Perovskite Solar Cells*", Materials Research Society (MRS) 2016, fall meeting, Boston, USA.

[4] Mar. 2016: **Poster presentation**, <u>Hawash, Z.</u>; Ono, L. K.; Qi, Y. B.,* "*Moisture and Oxygen Induced Enhancement of the Conductivity in LiTFSI Doped spiro-MeOTAD films*", The Japan Society of Applied Physics (JSAP), Tokyo Inst. of Tech, Tokyo, Japan.

[3] Jan. 2016: **Invited oral presentation,** <u>Hawash, Z.</u>; Ono, L. K.; Qi, Y. B.,* "*Moisture and Oxygen Induced Enhancement of the Conductivity in LiTFSI Doped Spiro-MeOTAD Films*", International Symposium on Functional Materials (ISFM 2016), OIST, Okinawa, Japan.

[2] May 2015: **Poster presentation**, <u>Hawash, Z.</u>; Ono, L. K.; Raga, S. R.; Lee, M. V.; Qi, Y. B.,* "*Air Exposure Effects on Spin Coated Spiro-MeOTAD Films and Implication on Perovskite Solar Cell Stability*", International Conference on Hybrid Inorganic-Organic Photovoltaics (HOPV15), Rome, Italy.

[1] Jun. 2014: **Poster presentation**, <u>Hawash, Z.</u>; Ono, L. K.; Qi, Y. B.,* *"Air Exposure Induced Oxidation of Doped Spiro-MeOTAD Based Hole Transport Layer: Implications on Perovskite Solar Cell Devices"* Challenges to open up the new era of organic photonics and electronics from material to market - from Asian perspective, Institute of Physical Chemistry, Polish Academy of Sciences, Department of Photochemistry and Spectroscopy, Warsaw, Poland.

Date: October, 2017

Signature:

Abstract

Surface Science Studies of Perovskite Solar Cells: Spiro-MeOTAD Hole Transport Material and Perovskite Absorber

The past few years have witnessed an emergence of an outstanding class of thin film solar cells, which are based on organic-inorganic light absorbers, namely, perovskite solar cells (PSCs). PSCs possess energy conversion efficiencies (PCEs) comparable to traditional silicon and other solar cell technologies. To achieve high efficiencies, typically perovskite materials are sandwiched between selective contacts, which significantly facilitate charge carries extraction. These contacts are made of either electron or hole selective material and are called electron transport material (ETM) and hole transport material (HTM). This thesis discusses surface science aspects of the doping mechanism of spiro-MeOTAD HTM, and an engineering approach of the perovskite/spiro-MeOTAD HTM interface for enhanced energy level alignment, efficiency, and reproducibility.

In this thesis surface science techniques (i.e., photoemission spectroscopy (PES), atomic force microscopy (AFM), and scanning electron microscopy(SEM)) combined with current-density voltage (J-V) measurements on hole only devices and PSCs are employed. PES measurements revealed that ambient air-exposure results in the migration of the commonly used Li-salt dopants from the bottom to the bulk (including top surface) of the spiro-MeOTAD HTM film. AFM and SEM images revealed the presence of pinholes with an average diameter of ~135 nm, with a density of ~3.72 holes/μm^2, and these pinholes form channels wiggling across the doped spiro-MeOTAD film. Under controlled environments of H_2O (relative humidity 90%) and dry O_2, PES measurements revealed that H_2O is the constituent component in ambient air that leads to the

redistribution of the LiTFSI dopants. In addition, the J-V measurement results on hole only devices revealed that H_2O vapor exposure results in an irreversible enhancement of LiTFSI-doped HTM conductivity due to redistribution of the LiTFSI dopants across the HTM film, which was examined by PES measurements. On the contrary, O_2 exposure results in a reversible enhancement of the HTM film under applied bias, in which this enhancement is mainly due to O_2 doping, which was confirmed by PES measurements.

In addition, to achieve better energy level alignment between the HTM and the perovskite absorber, an intentional deposition of an ultrathin layer of methylammonium iodide (MAI) on top of a methylammonium lead iodide (MAPI) perovskite film was implemented. Using PES measurements, it was found that the deposition of small amount of MAI on top of MAPI results in an interfacial, favorable, energy-level tuning of the MAPI film. XPS measurements revealed that the enhanced energy-level tuning was from MAI dissociated species, not the MAI itself. Furthermore, the optimized energetics were verified using perovskite solar cells. Substantially enhanced stabilized-PCE and reproducibility was achieved (from $15 \pm 2\%$ to $17.2 \pm 0.4\%$).

To my parents

Mahmoud Hawash and Yusra Hijjazi

To my wife

Marwa Shouli

Acknowledgements

First of all, I would like to thank Okinawa Institute of Science and Technology Graduate University for the academic and financial support that I received during my PhD.

I would like to express my sincere gratitude to Professor Yabing Qi for being my supervisor and providing me with all I needed during my PhD. He helped me to develop my career, character and experience.

Special thanks and deepest gratitude to our group leader at Energy Materials and Surface Sciences Unit (EMSSU), Dr. Luis K. Ono. I will miss our interesting and long-lasting chats discussing research, experiments, and life.

I would like to thank Professor Nam-Gyu Park and Dr. Dae-Yong Son for providing me with all needed support and help during my visit to their laboratory in South Korea.

In addition, I would like to thank all the current and former members of EMSSU, Dr. Sonia Raga, Dr. Michael V. Lee, Dr. Shenghao Wang, Dr. Min-Cherl Jung, Dr. Matthew R. Leyden, Dr. Emilio J. Juarez-Perez, Dr. Yan Jiang, Dr. Robin Ohmann, Dr. Mikas Remeika, Dr. Longbin Qiu, Dr. Taehoon Kim, Dr. Lingqiang Meng, Dr. Zhifang Wu, Dr. Jeremy Hieulle, Mr. Collin Chandler Stecker, and Ms. Naoko Ogura-Gayler.

List of Abbreviations

AFM	Atomic force microscopy
AM 1.5G	Solar spectral irradiance according to American Society for Testing Materials, ASTM G-173-03
ASF	Atomic sensitivity factor
BE	Binding energy
CBM	Conduction band minimum
DEE	Diethyl ether
DMF	N, N - dimethylformamide
DMSO	Dimethylsulfoxide
DSSC	Dye sensitized solar cells
EA	Electron affinity
E_F	Fermi energy
E_K	Kinetic energy
ESCA	Electron spectroscopy for chemical analysis
E_V	Vacuum level
ETL	Electron transport layer
ETM	Electron transport material
FF	Fill factor
FK209	Tris(2-(1H-pyrazol-1-yl)-4-tert-butylpyridine)cobalt(III) bis(tri-fluoromethylsulphonyl)imide
FTO	Fluorine doped tin oxide
FWHM	Full width half maximum
h	Plank's constant
HTL	Hole transport layer
HTM	Hole transport material

HOMO	Highest occupied molecular orbital
IE	Ionization energy
IMFP	Inelastic mean free path
J	Current density
J-V	Current density – voltage
J_{SC}	Short circuit current
LUMO	Lowest un-occupied molecular orbital
LiTFSI	Li-bis(trifluoromethanesulfonyl)-imide
MA	Methylammonium
MAI	Methylammonium iodide
MAPI	Methylammonium lead iodide
mp-TiO_2	Mesoporous-TiO_2
PCE	Power conversion efficiency
PES	Photoelectron spectroscopy
PSC	Perovskite solar cell
PTTA	Polytriarylamine
PV	Photovoltaic
PVSK	Perovskite
RH	Relative humidity
SCLC	Space charge limited current
SEM	Scanning electron microscopy
Spiro-MeOTAD	2,2′,7,7′-tetrakis(*N*,*N*-di-*p*-methoxyphenylamine)-9,9′-spirobifluorene
Spiro-TAD	2,2',7,7'-tetrakis-(diphenylamino)-9,9'-spirobifluorene
SPM	Scanning probe microscopy
ssDSSC	Solid state dye sensitized solar cell
STD	Standard deviation
STM	Scanning tunneling microscopy
Tg	Glass transition temperature

t-BP	4-*tert*-butylpyridine
TLD	Through the Lens Detector
TPD	N,N'-diphenyl-N,N'-bis-(3-methylphenyl)-1.1'-biphenyl-4,4'-diamine
UHV	Ultra-high vacuum
UPS	Ultra-violet photoelectron spectroscopy
v	Frequency
V_{OC}	Open circuit voltage
VBM	Valence band maximum
WF	Work function
w.r.t	With respect to
XPS	X-ray photoelectron spectroscopy
XRD	X-ray diffraction
Φ	Work function
σ	Conductivity
Ω	Ohm
ε	Permittivity
ε_o	Permittivity of free space
μ	Mobility

List of figures

Table of contents

Chapter 1: Instrumentation

1. 1. Ultra-High Vacuum:

In this dissertation, high vacuum and ultra-high vacuum (UHV) were utilized for different experiments. Medium to high vacuum was used for evaporation of different materials such as gold electrodes for hole-only devices, for perovskite solar cells, for interfacial modification of the perovskite, and for the environmentally controlled experiments (10^{-5}- 10^{-8} Torr.). UHV was used as the environment for the photoemission spectroscopy as well as scanning electron microscopy (10^{-7}- 10^{-9} Torr.).

In surface science studies, the need for the vacuum conditions relies on different factors. The main reason for utilizing high vacuum conditions is to maintain a clean surface of the samples under study. This can simply be depicted based on Hertz-Knudsen equation which explains the molecular flux of materials and its linear relation with pressure.[1] The surface cleanness is directly related to the analytical techniques used to study the sample. Some of these techniques are very sensitive to surface and its probing depth is in range of few nanometers as will be discussed later. Another reason for using vacuum is the setup requirements for some specific analytical techniques, in which the minimum scattering for a generated photoelectron by other gas molecules is required. Similarly, an ejected photoelectron from a specific element needs to travel without any interruption to the analyzer.

1. 2.   X-ray Photoelectron Spectroscopy (XPS):

XPS was implemented for investigation of the chemical changes in different layers of the perovskite solar cells. The core levels of specific elements related to the material under study were monitored. In case of spiro-MeOTAD HTM, the core levels of the spiro-MeOTAD elements as well as the used dopants were monitored before and after different environmental conditions. Similarly, in the perovskite/spiro-MeOTAD interface modification study, the perovskite absorber layer elements were monitored and compared before and after different modification steps.

XPS is mainly based on the photoelectric effect which was described theoretically by Albert Einstein when he discussed the production and conversion of light.[2] Einstein's work lead researchers to develop the instrumentation for XPS and a Nobel prize in physics was granted to Kai Siegbahn in 1981 for his contribution to develop a high-resolution electron spectroscopy "electron spectroscopy for chemical analysis (ESCA)".[3] ESCA or alternatively XPS is based on the employment of a soft x-ray beam with an energy of (hv) to excite an electron from the core levels of a specific element with specific binding energy (BE), Fig. 1.1. Then an electron spectrometer measures the kinetic energy (E_K) of the ejected photoelectrons and therefore, the BE of the ejected electrons will be given by equation (1.1):

$$BE = hv - E_K - \Phi_{sample} \tag{1.1}$$
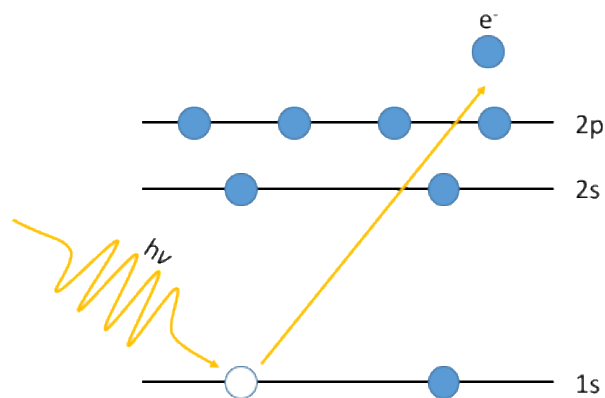
Figure 1.1 Representation of photoelectron generated in XPS from an element core level.

XPS allows us to qualitatively and quantitatively identify almost all of the periodic table elements that we have in the top surface of our samples. Therefore, it is one of the most powerful techniques for chemical analysis of solid surfaces.

1. 3. Ultraviolet Photoelectron Spectroscopy (UPS)

In this dissertation UPS was used for exploring the electronic structures for the spiro-MeOTAD HTM as well as the perovskite absorber. UPS was used to determine the valance band (VB) and the work function (WF) of the films under study.

Similar to XPS, UPS relies on the photoelectric effect in which a monochromatic beam is utilized to eject electrons of the material under study and therefore probe its VB and WF. Usually, the bandwidth of the materials is in range of few eV. Therefore, a low energy photon excitation source is used and often He I, which provides 21.21 eV photon source. The excited electrons undergo elastic and inelastic process before reaching the detector, which can translate their kinetic energies into a characteristic spectrum that provides us with the WF and VB values (Fig. 1.2).
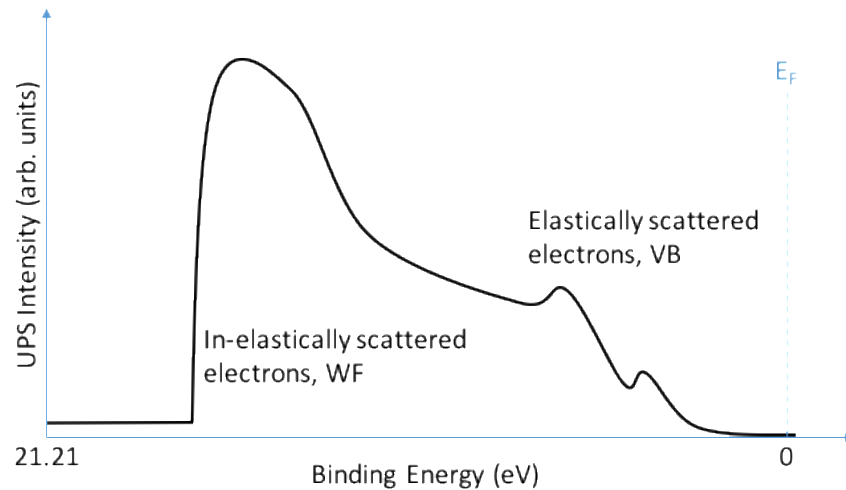
Figure 1.2 Photoexcitation of electrons in UPS.

1. 4.   Inelastic mean free path (IMFP)

The inelastic mean free path (IMFP) is one of the important aspects for electrons when working with photoemission spectroscopy. It explains the mean distance that an electron can travel before it loses some of its energy due to interaction with other particles. Therefore, it is important when employing photoelectrons as excitation source as well as for the afterwards ejected electrons. In 1979, Seah and Dench[4] provided a compilation for all measured IMFP for elements. Interestingly, the compiled data shows that IMFP for electrons with energy of 10 to 1000 eV goes from about 1.5 nm to a minimum of about 0.45 nm. Therefore, this is a very important concept when using photoemission spectroscopy, specially with the employment of different photoelectron energies to study surfaces of materials.

1. 5.   Scanning Electron Microscopy (SEM)

SEM utilizes a focused beam of electrons to provide high-resolution images by scanning of the sample surface. SEM provides images which are generated with depth effect and therefore it

has three-dimensional looking images. It consists mainly from an electron gun, electromagnetic lenses, beam deflection system for scanning, and detector.

Two kinds of electrons are generated or emitted from the sample while scanning with the electron beam: secondary electrons and backscattered electrons. The backscattered electrons are generated from elastic scattering of the beam electrons. The secondary electrons are generated from inelastic scattering of the electrons due to ejection of electrons from the sample atoms. While the back scattered electrons provide information about the elemental composition of the sample, the secondary electrons provide topographical information.

In SEM, the resolution of the created images depends highly on the electron probe area on sample surface. There are few important parameters that controls the probe diameter: the probe current, the convergence of the probe, and the brightness of the beam. The brightness of the beam is dependent on the electron gun type (field emission> LaB_6> tungsten) and proportional to the acceleration voltage used.

1. 6.   Atomic Force Microscopy (AFM)

AFM or generally the scanning probe microscopy (SPM) is relatively a new characterization technique compared to that using beam of electrons or visible light. In 1986, the AFM was introduced by Binnig and Quate[5] as a derived application from the concept of scanning tunneling microscopy (STM).[6] The AFM has an advantage over the STM in which the sample does not need to be conductive. Alternatively, AFM scans the interaction between the atoms of a very sharp tip mounted on a cantilever and the atoms on the surface of the material under study and this provides three-dimensional images. Scanning the interaction between the probe and sample atoms

eliminates the resolution limits associated with optical or electron microscopy and therefore provides us with very high-resolution images down to atomic level.

AFM system consists of few simple components: a probe, motion sensor, scanner, controller, computer, and vibration isolation system. The probe is often made out of SiO_2 or Si_3N_4 mounted onto a cantilever and etched to provide a sharp apex with a diameter that can be down to few nanometers. The most often used motion sensor is based on deflection of laser beam from the cantilever onto a quadrant photodiode which sends the deflection information to an electronic controller and computer. The electronic controller and computer are responsible for magnifying the signal and provide a feedback loop based on a set parameters which controls the tip-sample distance. The vibration isolation system is very important with such an atomic three-dimensional scanning system where any floor vibration or acoustic vibrations can severely affect the scan.

As aforementioned, AFM scanning is based on the interactions between a sharp tip and the sample at atomic level. At short range distance (in the order of atomic level) the tip apex undergoes a strong repulsive force. This repulsive force is sensitive to the topography of the sample and therefore it is usually utilized to provide topographic images of the samples in a mode called contact-mode. Alternatively, non-contact mode can be used to avoid direct contact between the tip and the sample. In non-contact mode, the AFM scan can be carried out at a farther distance from the sample surface, where the tip interacts with weak attractive force with the sample surface. In this mode, the cantilever is oscillated using piezo-actuator and changes in the amplitude or shift of the frequency are monitored to provide information about the surface of the sample.

Chapter 2: General Introduction[7]

2. 1.   Perovskite Solar Cells

The past decade has witnessed an emergence of an exceptional class of thin film solar cells, which are based on organic-inorganic light absorbers, namely, perovskite solar cells. Perovskites absorber can be solution-processable, compatible with large-area and flexible-substrates, and has promising cost estimates. PSCs possess power conversion efficiencies comparable to traditional silicon solar cell technologies. The emergence of PSCs[8-9] and subsequent advancements in their PCEs exceeding 22%[10-11] have captured the attention of photovoltaics research society and industry[12]. Perovskite semiconductors are currently being intensively investigated for applications such as light emitting diodes,[13-15] lasing,[16-17] energy storage,[18] water splitting,[19-20] photodetectors,[21] and memory devices.[22] Typical PSCs are composed of transparent top electrode, electron transport material, perovskite absorber, hole transport material, and bottom electrode.

The perovskite light absorber has a crystal structure similar to calcium titanate, which was discovered by Gustav Rose in 1839 and later named after Russian mineralogist Count Lev Alekseevich Perovski. The first report about lead halide perovskites goes back to 1893, when Wells reported for the first time about cesium lead halides.[23] In 1958, Moller reported the structure for the cesium halides.[24] Not much attention was received towards these materials even with its hybrid class reported by Weber in 1978[25] nor after it showed a potential with facile solution processing and promising electrical properties.[26-27] The first perovskite solar cell was reported in 2006 by Kojima et al.[28] at the 214th electrochemical society meeting using electrolyte in a device

architecture similar to that of dye sensitized solar cells and was published in 2009 with a moderate PCE of 3.8%.[29] However, a major leap in PSCs surged with the adoption of the architecture used for solid state dye sensitized solar cells. In typical DSSCs a liquid redox electrolyte consists of lithium iodide/triiodide is usually implemented.[30] Bach et al.[31] replaced this lithium iodide/triiodide electrolyte with an amorphous solid HTM, namely, spiro-MeOTAD. The replacement provided efficient charge carrier extraction. Similarly, Kojima et al.[29] report on organic-inorganic perovskite sensitizers by employing liquid electrolyte, Kim et al.[8] and in parallel Lee et al.[9] tried a similar approach and replaced the liquid electrolyte by the spiro-MeOTAD HTM in the perovskite solar cells.[8-9] The alteration to a solid HTM such as spiro-MeOTAD provided substantial increase in the PCE and stability of the devices, exceeding 10% of PCE.[9] In addition, stable operation of 500 h in air without any encapsulation was observed.[8] Since the replacement of lithium iodide/triiodide with the solid state spiro-MeOTAD HTM, intensive attention was drawn towards perovskite solar cells and within a few years PCEs increased substantially to reach certified PCEs exceeding 22.1%.[11]

2. 2. Spiro-MeOTAD

PCEs exceeding 20%[10] was achieved utilizing LiTFSI-doped spiro-MeOTAD HTM. Although PTAA HTM has been shown as another promising alternative HTM layer (Fig. 2.1), this survey shows that at the current stage LiTFSI-doped spiro-MeOTAD is still the dominant HTM employed in majority of the perovskite solar cells. The combination of multiple factors such as (i) the relatively simple recipe, (ii) solution-processable, (iii) high melting temperature, (iv) amorphous nature, (v) good conductivity, and (vi) proper energy levels that matches well with perovskites make doped spiro-MeOTAD one of the most widely employed HTM in PSCs. Spiro-MeOTAD is particularly well suited for MAPbI₃ perovskites. However, the mismatch between the HOMO

energy level of the spiro-MeOTAD HTM and VBM of the perovskite becomes excessive when considering perovskites with large band gaps,[32-33] such as $MAPb(I_xBr_{1-x})_3$, which are of interest for tandem solar cells. Pristine spiro-MeOTAD films suffers from low electrical conductivity. Additives such as LiTFSI, t-BP, and cobalt(III) complex FK209 are often used to enhance the electrical properties of the spiro-MeOTAD HTM films.[34] A survey of the reported recipes for the synthesis of the LiTFSI-doped spiro-MeOTAD HTM suggests that there is no common recipe.[35-38] For instance, the first point in Fig. 2.1, corresponding to a PCE of 9.7%, employs a mixture of spiro-MeOTAD: LiTFSI: t-BP in molar ratios of 1:0.38:1.16.[8] However, the next point reporting a higher PCE of 10.9% employed a much lower dopant concentrations of spiro-MeOTAD: LiTFSI: t-BP = 1:0.13:0.81.[9] The incorporation of FK209 into the spiro-MeOTAD HTM recipe resulted in a PCE of 21.1%[38] as can be seen in Fig. 2.1 (spiro-MeOTAD: LiTFSI: t-BP: FK209 = 1: 0.5: 3.3: 0.03). The PCEs reported in Fig. 2.1 reflect mainly the significant improvements in the quality of the perovskite absorber layer. In addition, these advances are benefited from a synergetic balance among the different functional layers (anode/ETM/perovskite/HTM/cathode).
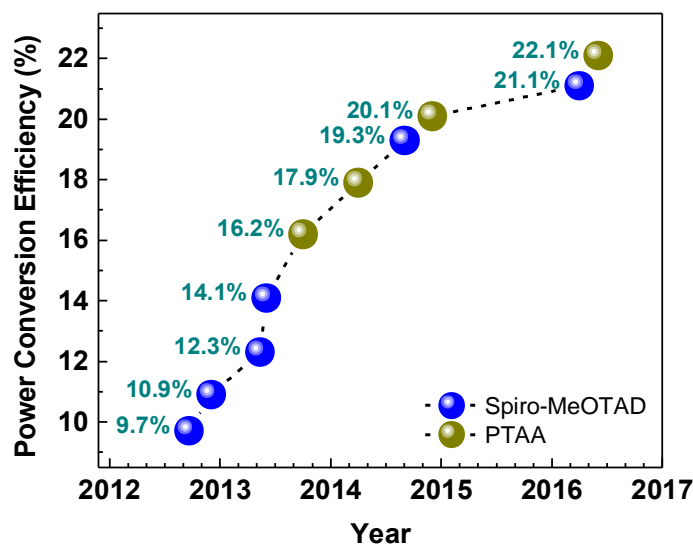
Figure 2.1 Trends in high-performing PSCs with focus on the HTM employed as a function of year. LiTFSI-doped spiro-MeOTAD is the dominant HTM widely used in high performing PSCs.

The motivation to synthesize HTMs with spiro-linked molecules was to achieve materials with high T_g, morphological stability, amorphous materials, and easy to process while keeping desirable electronic properties. The spiro molecular design was suggested to achieve such properties based on the concept of connecting two extended π systems with different or identical functions using common sp^3-hybridized atoms (Fig. 2.2a).[39] Molecular synthesis starts via a molecule with desirable electronic properties which can be further improved to achive better stability while maintaining the desired properties. Facci et al.[40] started with a well-known HTM widely employed in electroluminescent devices, namely, TPD[41] (Fig. 2.2b). However, TPD molecule suffered from low stability because of its low T_g of 60 °C. Based on the TPD structure and in parallel with the spiro-linked molecules concept, Salbeck et al.[42-43] synthesized spiro-TAD (Fig. 2.2c).[42-43] In addition, Facci et al.[40] showed that the addition of two *p*-methoxy groups (electron donating) to TPD increased its hole mobility by a factor of seven due to higher overlapping of electronic groups in this new molecule (MeO-TPD, Fig. 2.2d). These motivations

led Salbeck et al.[42-43] to synthesize spiro-TAD and used it in a blue light emitting device employing a two-layer stacked configuration where another spiro-linked molecule, spiro-PBD (Fig. 2.2e) was employed as ETL. Salbeck et al.[42-43] adopted the same strategy reported by Facci et al.,[40] but with the spiro-linked molecule resulting in synthesis of spiro-MeOTAD (Fig. 2.2f), where *p*-methoxy groups were added as well. The addition of *p*-methoxy groups provided 8 electron donating groups. These electron donating groups lowered the oxidation potential by 0.1 V compared to that of the spiro-TAD molecule and by 0.22 V compared to TPD molecule. The lowered oxidation potential resulted in a lower injection barrier with the ITO anode where the spiro-MeOTAD was meant to be employed. The newly developed molecule resulted in better stability with T_g of about 121 °C[31] and with the desired electronic properties of the TPD molecule.[39, 44]
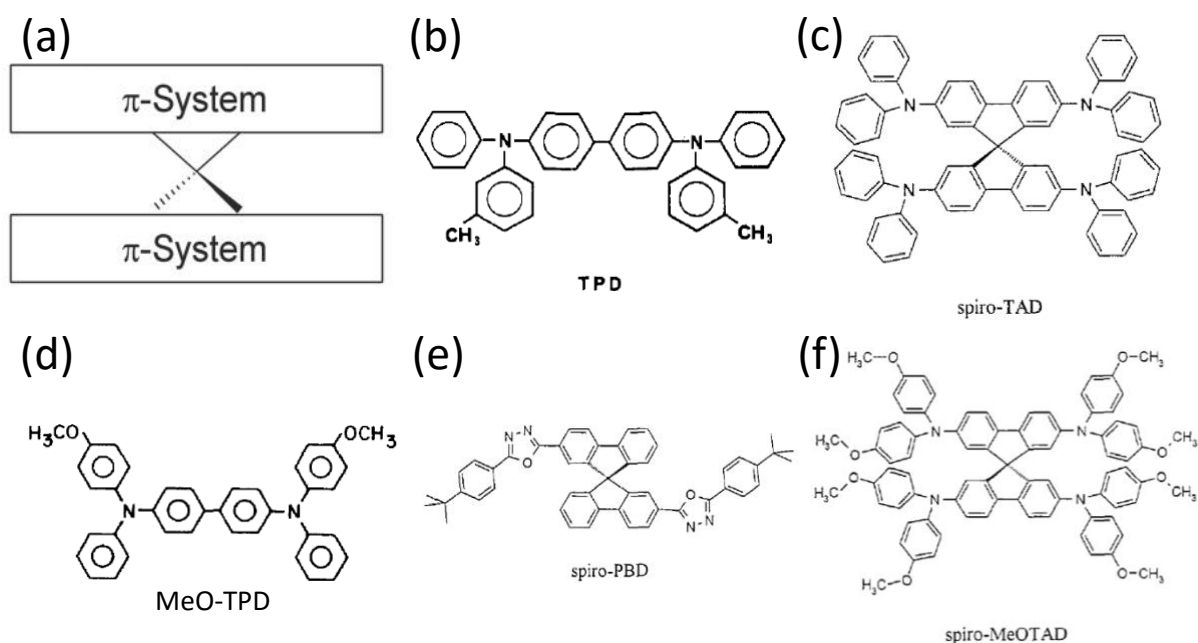
Figure 2.2 (a) spiro-linked systems, (b) TPD HTM, (c) spiro-TAD HTM, (d) MeO-TPD HTM, (e) spiro-PBD ETM, and (f) spiro-MeOTAD.

The stability of spiro-MeOTAD molecule that originates from its amorphous nature and its relatively high T_g brought attention to different potential applications in optoelectronics. Bach et al.[31] was the first to introduce spiro-MeOTAD HTM in DSSCs and used it as an efficient heterojunction layer formed with dye absorbers and provided a high yield of photon induced electric current. Following Bach et al.[31] recipe, many research groups widely adopted the use of spiro-MeOTAD as HTM in ssDSSCs.[45] Burschka et al.[46] achieved the highest PCE at that time in ssDSSCs using LiTFSI-doped spiro-MeOTAD HTL which provided a PCE of 7.2%. Similarly, spiro-MeOTAD was adopted in PSCs and lead breakthroughs in PCEs exceeding 22% as well as substantially improved stabilities.[47-50] Since 2012,[8-9] the first trials of employing spiro-MeOTAD in conjunction with organic-inorganic perovskite light sensitizers, an outstanding current density and V_{OC} were obtained when compared to ssDSSCs counterparts. This outstanding performance of perovskite-based solar cells was suggested to originate from proper choices of the functional layers (the absorber layer and the selective contacts) that work in harmony. For example, the perovskite absorber was shown to have a high absorption coefficient, ambipolar chare transport properties, long charge-carrier diffusion lengths, low exciton binding energy, and low charge trap densities or formation of only shallow-trap states within the perovskite absorber band gap.[51-57] The generated charge carriers are efficiently extracted and transported through the ETL and the HTL.[8-9] Spiro-MeOTAD molecule was also employed in photo-detector applications.[58-59] It was reported that spiro-MeOTAD film can form a very high quality p-n heterojunction with antimony trisulfide (Sb_2/S_3) that resulted in fast self-biased visible light photo-detector.[59] Similarly, spiro-MeOTAD in conjunction with nano-rods of zinc oxide showed enhanced sensing properties, such as, dimmed light intensities.[58] These applications aforementioned and more prove the practical functionality of spiro-MeOTAD molecule in the field of the optoelectronics and organic semiconductors.

2. 3.   LiTFSI Dopants

The first dopants employed for spiro-MeOTAD HTM were lithium- and antimony- based salts LiTFSI and N(PhBr)$_3$SbCl$_6$, respectively, employed in ssDSSCs. The additives were dissolved in chlorobenzene and acetonitrile at a ratio of spiro-MeOTAD: additive = 90:10.[31] The antimony salt was suggested to act as dopants by introducing free charge carriers in the HTM film via oxidation of the spiro-MeOTAD$^+$ molecules. The second dopant, the ionic lithium salt dopants provide the Li$^+$ ions to the system, which is known to be potential determining for the TiO$_2$ electrode.[31, 60] This means that the electrochemical properties of the TiO$_2$ surface can be controlled by the adsorption and intercalation processes of the Li$^+$ cations.[31, 60] Acetonitrile was used for the absorption of Ru-based dye sensitizer on screen printed mesoporous-TiO$_2$ and derivatization.[31] More importantly, addition of 12% of LiTFSI dopants was reported to increase the mobility of spiro-MeOTAD HTM by two orders of magnitude, which was confirmed by fabricating in-plane hole-only devices of Au electrodes/doped spiro-MeOTAD/dye/TiO$_2$ mesoporous/glass.[61] The improvement was explained by increased disorder and thus broadening of the tail of the density of states as well as screening of deep Coulomb traps by presence of Li$^+$ ions.[61] Although mobility is improved, interestingly, addition of LiTFSI dopants did not show the characteristic oxidation peaks of the spiro-MeOTAD$^+$ in the absorbance spectrum. The authors proposed that LiTFSI dopants alone does not p-dope spiro-MeOTAD molecules by oxidation.[61] On the basis of conductivity, SCLC model, and time-of-flight transient hole-current measurements, LiTFSI dopants results in improved charge carrier mobility.[61] A question naturally arises, *what is the microscopic mechanism that leads LiTFSI dopants to improve the mobility* (an order of magnitude higher compared to pristine spiro-MeOTAD) *as well as p-doping phenomena*. Snaith and Grätzel[61] provided a rationale for this question based on previous works,[62-64] which are based on the

influences of dopant anions on charge transport characteristics in disordered organic semiconductors. Briefly, charge transport between available sites occurs via a hopping mechanism. Then, the incorporation of p-dopants leads to positive charge transfer to the host molecules, which increases the overall hole density in the HTM film. These holes will fill the deepest trap states explaining the improvements in the hole mobility of the HTM film as well E_F shifts toward the HOMO energy level. A shift of 0.8 eV in the HOMO level by addition of LiTFSI dopants to spiro-MeOTAD towards E_F was confirmed using hard x-ray photo electron spectroscopy.[65] In addition, its results showed that there is a vertical gradient in the distribution of the LiTFSI dopants across the HTM layer.[65] The charge transport enhancements were only observed in the case of high concentrations of LiTFSI dopants, which was explained based on small doping concentrations, the p-dopant molecules also introduces immobile acceptor anions in the host film. That leads to generation of deep Coulomb traps and thus has detrimental effects on the mobility. As the doping concentration is increased, the Coulomb potential wells of anions start to overlap, resulting in a reduction of the barrier heights ("smoothing" the potential landscape) for charge hopping and thus increasing mobility. This is equivalent to the "broadening of the tail states" that was proposed to enable increased overlapping between deep traps sites moving HOMO level or the mobility edge closer to the quasi-E_F for holes.[61]

Chapter 3: Topography of LiTFSI Doped Spiro-MeOTAD[66]

3. 1. Introduction

As aforementioned one of the leading improvements of ssDSSC compared to DSSC was the replacement of the liquid electrolyte HTL with solid organic HTL.[31, 67] In typical DSSC a liquid redox electrolyte consists of lithium iodide/triiodide is usually implemented.[30] The replacement of the liquid electrolyte with spiro-MeOTAD HTL solved the problem of leakage and sealing issues for DSSC, as well as culminated as one of the most important HTLs for perovskite based solar cells.[8-9, 68] Spiro-MeOTAD is widely used HTL in currently high-performance solid-state solar cells, mostly due to its high stability (glass-transition temperature Tg = 121 °C), high solubility, and amorphous nature.[69-72] The HTL material infiltration into the mesosporous TiO_2 layers up to few micrometers has been reported.[71]

A thick enough layer of the spiro-MeOTAD HTL was proposed to be free of pinholes for ssDSSC[73] and similarly similar assumption was made for perovskite solar cells.[74] However, until publishing the results of the following chapter in 2015 [66] spiro-MeOTAD was not examined for defects in morphology, such as pinholes or voids.

Due to the importance of the morphology defects in the HTL, this chapter will be only discussing the morphology of the spiro-MeOTAD HTL studied by atomic force microscopy (AFM), cross-sectional scanning electron microscopy (CS-SEM), and optical microscopy.

3. 2.   Experimental Methods

Doped spiro-MeOTAD solution (Fig. 3.1) was prepared according to the standard literature procedure.[75] Spiro-MeOTAD (SHT-263, Merck KGaA) was dissolved in chlorobenzene and mixed with 4-tert-butylpyridine (*t*-BP, Sigma) and acetonitrile (52 mg/100 μL) dissolved Li-bis(trifluoromethanesulfonyl)-imide (LiTFSI, Sigma). The final solution had concentrations of 56.4 mM of spiro-MeOTAD, 187.9 mM of LiTFSI, and 30.46 mM of *t*-BP. Therefore, the corresponding molar ratios of spiro-MeOTAD : LiTFSI : *t*-BP were 1: 0.54 : 3.33 based on the nominal concentrations.
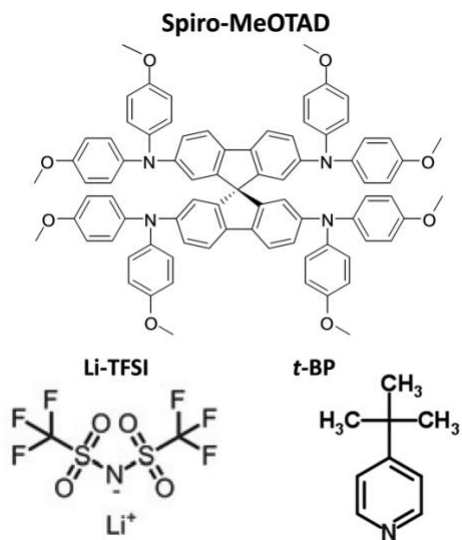
Figure 3.1 Molecular structures of LiTFSI, *t*-BP, and spiro-MeOTAD composing the doped spiro-MeOTAD hole transport material.

Thin films of doped spiro-MeOTAD were prepared by spin coating in nitrogen glove box for 60 s at a speed of 2000 rpm. Spin coating was performed on a thermally evaporated 120 nm film of Au (Denton Vacuum Evaporator, Model DV-502V) on heavily doped Si substrates with a thin native oxide layer of SiO_2 (SAMCO Inc., 0.013 Ω·cm). The final thickness of the films was approximately 240 nm as determined by a profilometer (Dektak stylus profiler, Bruker).

The morphological characterization of the films was performed *ex situ* using AFM in tapping-mode (MFP-3D series, Asylum Research). The quantitative analysis of the AFM was conducted using WSxM 5.0 software. The cross-sectional SEM images were obtained at 1.5 kV with through the lens detector (TLD) for detecting secondary electrons (FEI, Helios NanoLab 650). The samples for cross sectional SEM were prepared by manual cleaving of the doped spiro-MeOTAD HTL deposited on 120 nm of Au layer /SiO_2(native oxide)/Si substrate using a diamond

scriber from the backside of the substrate. Air exposure experiments were performed in dark stainless-steel container in the ambient air of the laboratory. The laboratory humidity and temperature were approximately 37 % and 24 °C, respectively.

3. 3.   AFM of As-prepared and Ambient Air Exposed Doped Spiro-MeOTAD

Fig. 3.2 shows AFM morphology images of an as-prepared doped spiro-MeOTAD HTL (a) and after 24 hours of air exposure (b). As can be seen from Fig. 3.2, a large density of pinholes of 3.72 holes/µm^2 was detected in the as-prepared films. The air exposed films showed similar morphology but the pinholes seemed to be being filled up.
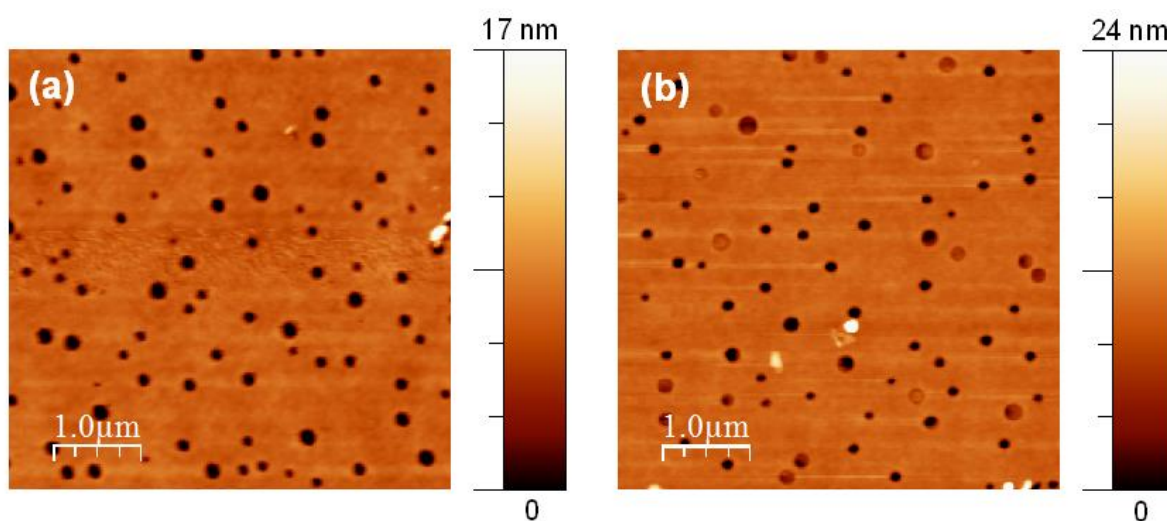
Figure 3.2 Tapping-mode AFM topography images of as prepared doped spiro-MeOTAD, and after 24 hours air exposure.

Based on the quantitative analysis of those morphology images, the integrated area of all pinholes corresponds to about 6% of the total surface area with an average diameter of 135 nm (Fig. 3.3). Similar pinholes were also observed when spiro-MeOTAD films were spin coated on

different substrates, such as the ones spin-coated on perovskite films, suggesting as a universal

phenomenon, the presence of these pin-holes in spiro-MeOTAD films prepared by spin coating.
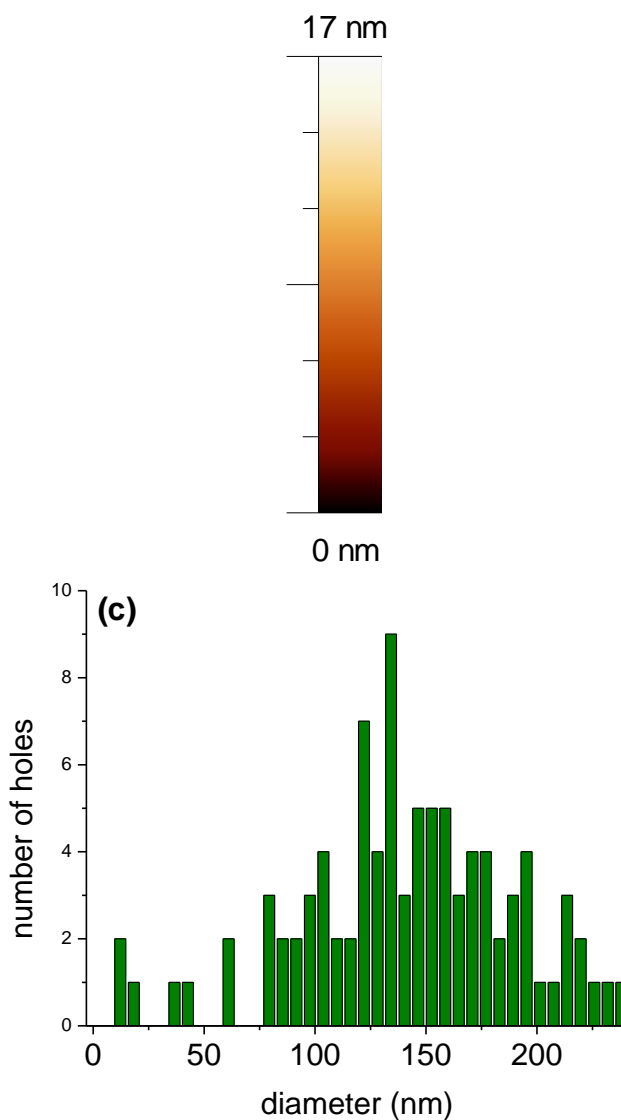
Figure 3.3 (a) Tapping-mode AFM topography images of the as-prepared doped spiro-MeOTAD, (b) Flooded image composed using WSXM software, and (c) frequency histogram for hole diameter data. Hole density of 3.72 holes/µm^2 were extracted, which corresponds to 5.86% of the total surface area with an average diameter of ~135nm.

3. 4. Optical Microscopy

Optical microscopy images of the doped spiro-MeOTAD on glass substrates showed large pinholes with diameters. The measured dimeters were in the range of 1-20 μm and with a density of ~289 holes/mm^2, which was extracted from 2×2 mm^2 area measurements (Fig. 3.4). The existence of pinholes in organic tin films is reported to lead to shorts between the different layers[76] and solutions have been sought to achieve pinholes-free devices.[76-78] These pinholes in spiro-MeOTAD HTL are also likely the cause for the very short lifetime commonly observed for perovskite solar cells that use spin coated spiro-MeOTAD as HTL. The existence of pinholes can possibly facilitate moisture migration through spiro-MeOTAD to reach perovskite layer and hence causing the degradation of the devices and similarly can facilitate elements from the perovskite layer (e.g. iodine) to migrate to top surface and degrade perovskite. On the basis of such observations and to increase the lifetime of the perovskite solar cells, it is necessary to optimize the preparation procedure of solution prepared doped spiro-MeOTAD HTL to avoid pinholes formation, such as by using different solvents, mixing with an additive, adding a capping layer, etc.
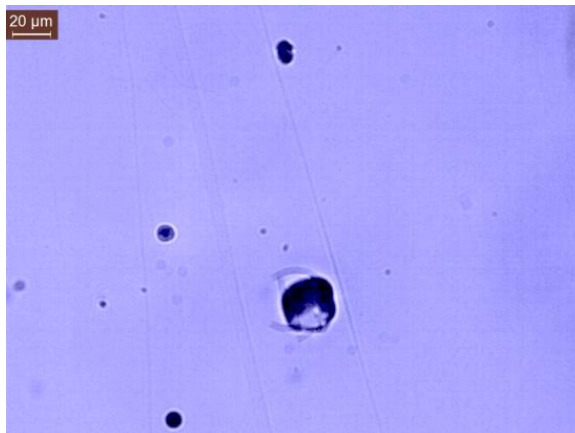
Figure 3.4 Optical microscope image of doped spiro-MeOTAD film.

3. 5.   Cross-Sectional Scanning Electron Microscopy

AFM provided us with three dimensional images of the top surface of the doped spiro-MeOTAD HTL. To further provide insights on the morphology of the pinholes of the doped spiro-MeOTAD HTL, cross sectional SEM was used on multiple samples of the doped spiro-MeOTAD films (Fig. 3.5). The high magnification SEM images presented in Fig. 3.5a revealed that the pinholes form channels across the HTL film (~240 nm depth) that wiggle through the whole film. The top surface SEM images of the spiro-MeOTAD films revealed that these channels are part of the high density of pinholes observed in the AFM images (Fig. 3.2). As described in the experimental methods, the samples were prepared by cleaving the doped spiro-MeOTAD film (240 nm), which was deposited on 120 nm of Au on SiO_2(native oxide)/Si substrate by using a diamond scriber from the backside of the substrate. The mechanical cleavage used was observed to tear apart the soft gold film together with the spiro-MeOTAD HTL film leaving portion of the underneath substrate exposed. The gold film appears delaminated from the underneath silicon

substrate and at the edges of the image in Fig. 3.5a and b, respectively, which is due to poor

adhesion of the evaporated gold on silicon dioxide.
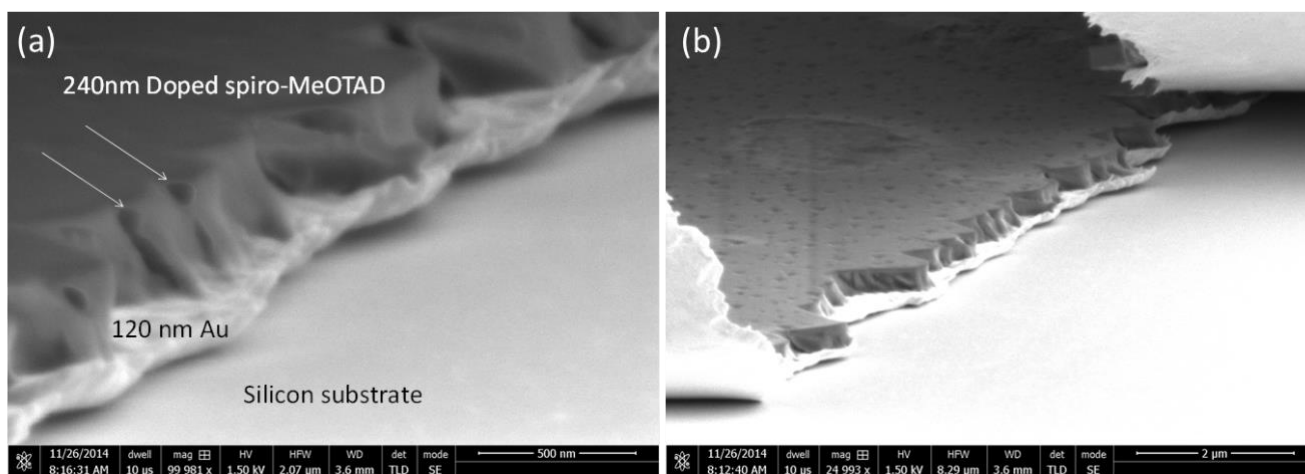
Figure 3.5 Cross sectional SEM of doped spiro-MeOTAD film on Au. (a) pinholes form channels across the doped spiro-MeOTAD film indicated with arrows in high magnification image, and (b) the pinholes observed from the top surface of the film and from the cross section.

3. 6.   Summary

In summary, AFM images revealed the presence of pinholes with an average diameter of ~135 nm and a density of ~3.72 holes/μm^2. In addition, cross-sectional SEM images reveal that these pinholes form channels that wiggle across the doped spiro-MeOTAD HTL film. Optical microscopy images revealed the presence of large area pinholes with diameters in the range of 1-20 μm and a density of ~289 holes/mm^2. The presence of these pinholes may play a major role in migration processes of LiTFSI dopants within the spiro-MeOTAD film. Similarly, it can detrimentally affect the life time of the solar cells by facilitating inward diffusion or intake of atmospheric gases such as H_2O or O_2 which would degrade the perovskite absorber layer. Interestingly, it was also found that the small-sized pinholes are partially filled up upon air exposure. The observation of the pinholes being filled up will be discussed in the next chapter

where chemical composition of the top surface was investigated using photoemission spectroscopy.

Adapted and reproduced with permission.[66] Copyright 2015, American Chemical Society.

Chapter 4: Ambient Air Effects on Chemical and Electronic Properties of Doped Spiro-MeOTAD[66]

4. 1. Introduction

As discussed in chapter 3, spiro-MeOTAD HTL suffer from high density of pinholes. These pinholes were observed to be filled up upon time in ambient environment. The materials and the mechanism that drives such an observation is not clear and would be expected to change the properties of the spiro-MeOTAD HTL and therefore would change the performance in the solar cells using it as HTL.

Spiro-MeOTAD in its pristine form is known to suffers from the low hole mobility and conductivity.[45, 79-80] Thus, inclusion of dopant, such as LiTFSI, helps to generate additional charge carriers, as well as tune the electronic properties of the HTL. This would help to achieve better energy-level alignment at the interfaces with the perovskite absorber and the bottom metallic electrode (often Au).[81-83]

The doping of spiro-MeOTAD HTL is generally associated with an oxidation reaction and efforts were made to find suitable dopants that effectively dope spiro-MeOTAD.[81-86] In the presence of LiTFSI dopants, spiro-MeOTAD is not readily oxidized in the presence of light or in

dark and the oxidation reaction is only promoted upon air exposure.[79, 87-88] In organic solar cells, air exposure leads to degradation of devices, however, air exposure is necessary during device fabrication in order to obtain a working perovskite cells when utilizing LiTFSI doped spiro-MeOTAD as HTL.[87, 89] In addition, as we discussed in chapter 3, air exposure induces morphological changes of the LiTFSI-doped spiro-MeOTAD HTL. Therefore, fundamental understanding remains elusive regarding the doping mechanism that takes place when the LiTFSI doped spiro-MeOTAD films are exposed to ambient air.

In this chapter, the electronic properties and the chemical composition of the LiTFSI-doped spiro-MeOTAD HTL and its interactions with air exposure is investigated. Comparisons are made to un-doped spiro-MeOTAD and spiro-MeOTAD films with only *t*-BP. As discussed in chapter 3, microscopy techniques revealed the presence of pinholes in those films. The observed pinholes were found to be filled up upon time with ambient air exposure. The existence of these pinholes is a possible factor to facilitate the diffusion of the dopant upon air exposure as well as on the degradation processes of the active materials (e.g., perovskite). The presence of these pinholes may also play a major role in the properties of the HTL when exposed to air. In this chapter photoemission spectroscopy techniques were utilized to monitor the top most surface of the spiro-MeOTAD HTL under controlled environments of ambient air, vacuum, and nitrogen.

4. 2. Experimental Methods

LiTFSI-doped spiro-MeOTAD solution and spin-coated films were prepared in the same way as previously discussed in section 3.2.

The electronic changes of different spiro-MeOTAD HTL films were characterized by ultraviolet photoelectron spectroscopy (UPS, Kratos AXIS ULTRA HAS, He-Iα = 21.22 eV) and the data analysis were performed in Origin Pro 9. The analysis of the UPS was complemented by X-ray photoemission spectroscopy (XPS, Kratos AXIS ULTRA HAS, monochromated Al Kα = 1486.6 eV). XPS measurements were performed to monitor the chemical states of the as-prepared spiro-MeOTAD films, air and nitrogen exposed films, and control films of spiro-MeOTAD HTL. The binding energy (BE) for UPS and XPS were calibrated by measuring Fermi edge (E_F = 0 eV) and Au-4$f_{7/2}$ (84.0 eV) on a clean Au surface. The estimated energy resolutions of UPS and XPS were 0.14 eV and 0.7 eV, respectively. Analysis of the XPS data was performed in CasaXPS 2.3.16 software. UV and X-ray induced damage were monitored by taking consecutive five spectra and comparing those spectra. The time acquisition for each scan was varied from 60 to 100 s depending on the core level regions under investigation. If no changes were observed among the five scans, the spectra were averaged to a single spectrum. Individual films of spiro-MeOTAD, LiTFSI, and *t*-BP were examined under UV and X-ray radiation. Special care was taken into account to minimize UV or X-ray exposure time when acquiring UPS/XPS on spiro-MeOTAD films. No X-ray or UV induced damages were observed on spiro-MeOTAD films. Fitting parameters of the XPS core levels were conducted following Hock *et al*.[81] A Shirley-type background was fitted due to inelastic scattering processes.[90] No X-ray and UV induced damage was observed on spiro-MeOTAD molecules.

The XPS detection of spin-coated or drop-casted *t*-BP compound on Au films were below the sensitivity of the XPS system when the samples were loaded into the XPS system. It was not possible to obtain reference UPS and XPS spectra for spin-coated *t*-BP on Au because of the high vapor pressure of *t*-BP. For the investigation of the influence of the *t*-BP molecule on spiro-

MeOTAD HTL, ten times higher concentration of *t*-BP solution was mixed with spiro-MeOTAD and films were prepared by spin coating.

Ambient air exposure experiments were performed on LiTFSI-doped spiro-MeOTAD films by exposure to the laboratory air in dark (samples stored in a stainless-steel container). The measured laboratory humidity and temperature were approximately 40 % and 24 °C, respectively. Controlled N_2 exposure experiments were conducted in the load-lock of the XPS/UPS system (N_2 gas pressure = 1 atm). Chemical states were also monitored by storing the samples in vacuum (2×10^{-9} Torr) for the same period of times used for the different gas exposures (as control) to rule out any measurement-induced uncertainties or artifacts (such as UV and X-ray radiation). No indication of radiation induced changes (e.g., dopant segregation, spiro-MeOTAD oxidation, or fragmentation of different chemical compounds) were observed by UPS and XPS on the LiTFSI-doped spiro-MeOTAD films with constant halogen light illumination (strong intensity in the visible range).

4. 3.   Electronic Changes (UPS)

Changes in the electronic properties of the LiTFSI-doped spiro-MeOTAD films after ambient air exposure were probed by UPS with He-Iα source (Fig. 4.1). The leading edge of the HOMO energy level with respect to the Fermi level w.r.t. E_F for the as-prepared LiTFSI-doped spiro-MeOTAD films was at − 0.54 eV (Fig. 4.1a(i)). After short exposure of three hours, the HOMO level of the LiTFSI-doped spiro-MeOTAD HTL showed a slight shift towards high BEs settling at −0.56 eV (Fig. 4.1a(ii)). Additional 3 hours of exposure (Fig. 4.1a(iii)) induced a large shift of the HOMO level leading edge, bringing it to −0.76 eV followed by an overall decrease in the intensity of the HOMO spectrum features. With a total of 18 or 39 hours of ambient air

exposure (Fig. 4.1a(iv), (v)), the HOMO leading edge further shifted to be at −1.00 eV and −1.04

eV, respectively. Complete disappearance of the HOMO features was observed after the 18 hours

air exposure. Nevertheless, the high sensitivity of the UPS system used for this experiment made

it still possible to extract the leading edge position of the HOMO level that was distinguishable

above the background signal. A substantial HOMO level shift occurred during the first 6 hours of

exposure and saturation was reached after 18 hours (Fig. 4.1a).
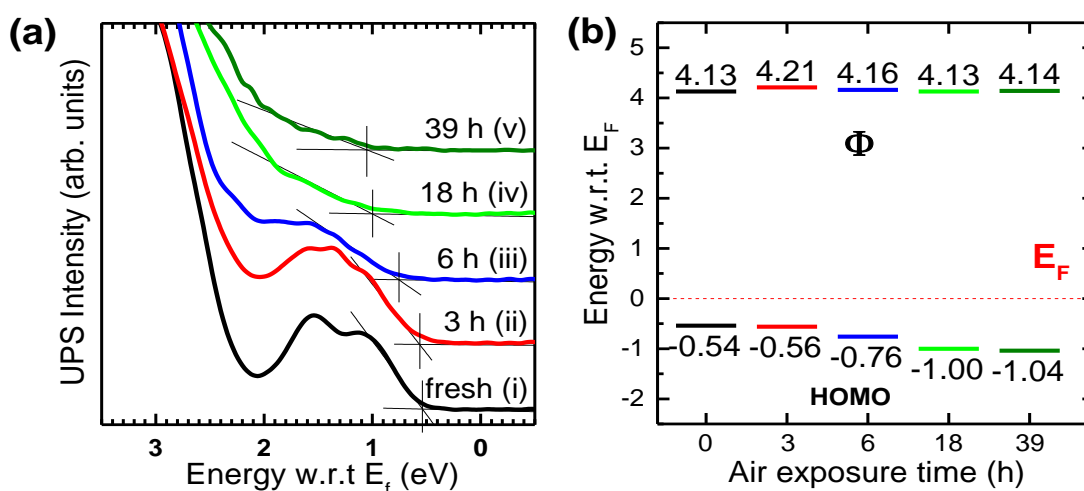
Figure 4.1 (a) UPS spectra (He−Iα = 21.22 eV) corresponding to the HOMO region
of the as-prepared doped spiro-MeOTAD film (i) and the same sample when exposed
to air for 3 hours (ii), 6 hours (iii), 18 hours (iv), and 39 hours (v). (b) Corresponding
schematic energy diagram of doped spiro-MeOTAD film.

Fig. 4.1b shows the schematic energy diagram with time evolution of the work function (Φ)

and HOMO level leading edge values w.r.t. E_F on the LiTFSI-doped spiro-MeOTAD films with

ambient air exposure. The Φ values were determined from the cutoff edge observed in the high

BE side of the UPS spectra (Fig. 4.2a). The extracted Φ values showed no change over the entire

ambient air exposure time in this experiment ($\overline{\Phi} = 4.15 \pm 0.03$ eV). The ionization energy (IE) was

calculated to be 4.67 eV for the as-prepared LiTFSI-doped spiro-MeOTAD film, which is about

0.3 eV lower than IE measured on pristine spiro-MeOTAD films prepared by vacuum-evaporation[80] and about 0.1 eV lower than the un-doped spiro-MeOTAD HTL films prepared by solution processing (Fig. 4.2b). The observed differences in the energy levels values are possibly due to different preparation methods used in these studies. Interestingly, the IE was observed to increase as a function of ambient air exposure period, from initial value of 4.67 eV for the as-prepared film to a saturation value of about 5.1 eV after 18 hours of air exposure. At the same time, as will be discussed in the XPS section, as-prepared LiTFSI-doped spiro-MeOTAD HTL film shows a small amount of LiTFSI at the top surface of the film. This indicates that a strong electronic interaction between spiro-MeOTAD molecules and the LiTFSI dopants prevails within the film upon ambient air exposure. The observed IE changes could be due to chemical changes of the spiro-MeOTAD induced by dopants, ambient air exposure contamination (induced by atmospheric aerosols),[91] or the diffusion of dopants populating at the top surface.
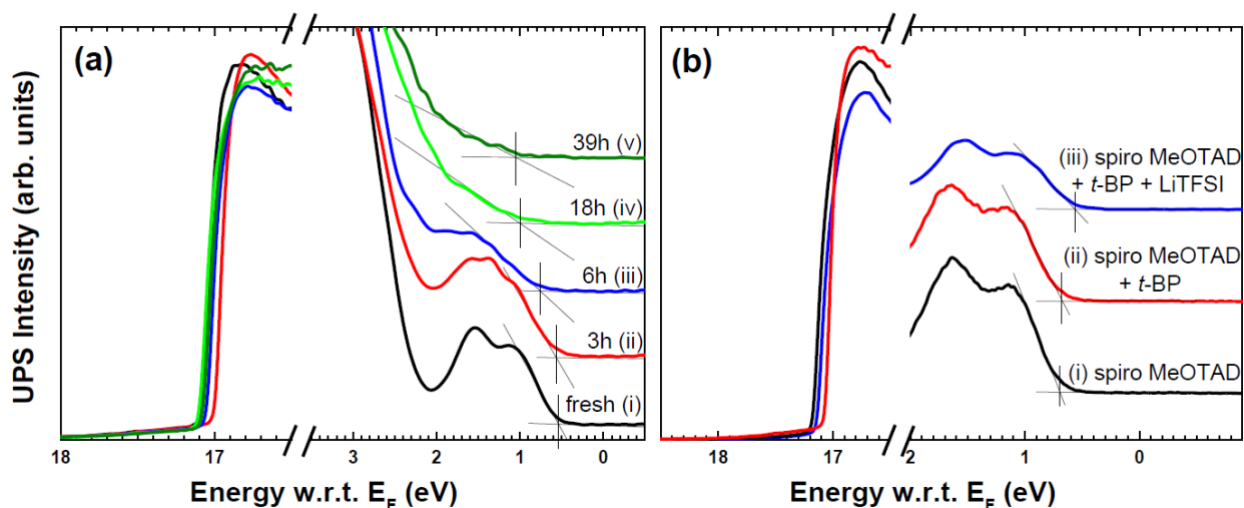
Figure 4.2 (a) UPS spectra (He−Iα = 21.22 eV) corresponding to the cut off region and the HOMO region of the as-prepared doped spiro-MeOTAD film (i), and subsequent air exposure for 3 hours (ii), 6 hours (iii), 18 hours (iv), and 39 hours (v). (b) UPS spectra (He−Iα = 21.22 eV) corresponding to the cut off region and the HOMO region of the as-prepared spiro-MeOTAD film (i), as-prepared t-BP doped spiro-MeOTAD film (ii), and as-prepared t-BP +LiTFSI doped spiro-MeOTAD film (iii).

4. 4. Chemical Changes (XPS)

The XPS measurements were performed after the UPS for each sample. The chemical states of the top surface for the films under study were monitored using XPS. Fig. 4.3 shows the XPS C-1s (a), Li-1s (b), and F-1s (c) core levels of LiTFSI- doped spiro-MeOTAD HTL films for the as-prepared sample (i) and same sample after different air exposure periods (after 3 hours (ii), 6 hours (iii), 18 hours (iv), and 39 hours (v)). The core levels of O-1s, S-2p, and N-1s were also monitored and are displayed in Fig. 4.4.
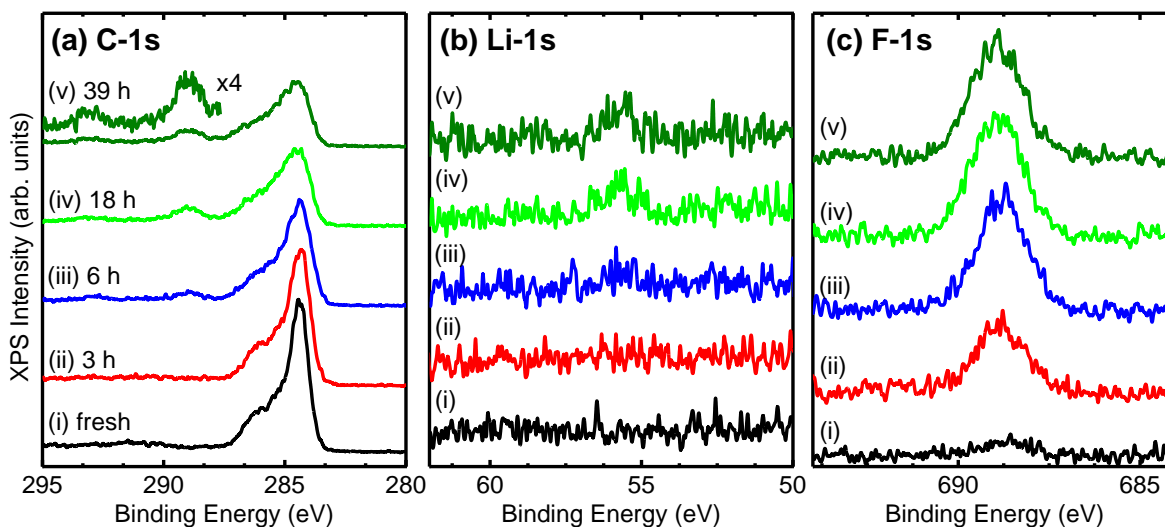
Figure 4.3 XPS spectra (Al−Kα = 1486.6 eV) corresponding to (a) C-1s, (b) Li-1s, and (f) F-1s core levels of the as-prepared doped spiro-MeOTAD films (i) and subsequent after 3 hours (ii), 6 hours (iii), 18 hours (iv), and 39 hours air exposure (v).
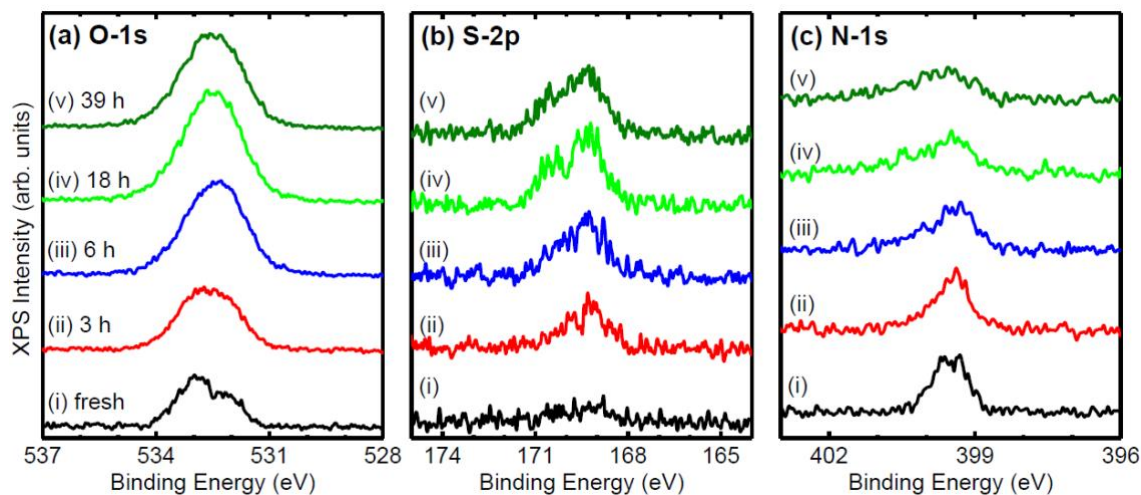
Figure 4.4 XPS spectra (Al−Kα = 1486.6 eV) corresponding to (a) O-1s, (b) S-2p, and (c) N-1s core levels of the as-prepared doped spiro-MeOTAD films (i) and subsequent air exposure for 3 hours (ii), 6 hours (iii), 18 hours (iv), and 39 hours (v).

As-prepared LiTFSI-doped spiro-MeOTAD HTL film shows an overall C-1s spectrum features similar to the pristine spiro-MeOTAD films.[65, 80-81, 92] A small signal of F-1s core level (~2.2%) corresponding to LiTFSI (Figs. 4.3b, c, and 4.4) was detected, meaning that a small amount of LiTFSI dopants is present at the top surface on the as-prepared doped film. Since the doped spiro-MeOTAD HTL films are composed of three chemical compounds (spiro-MeOTAD, LiTFSI, t-BP), the overlapping of C−H, C−C, and C−N signals from the spiro-MeOTAD molecule and t-BP molecule are unavoidable. Therefore, analysis of the curve fitting in C-1s core level region is challenging. In addition, for comparison, XPS measurements were performed on a film of spiro-MeOTAD mixed with t-BP only and was compared to pristine spiro-MeOTAD film, however, no difference was observed (Fig. 4.5).
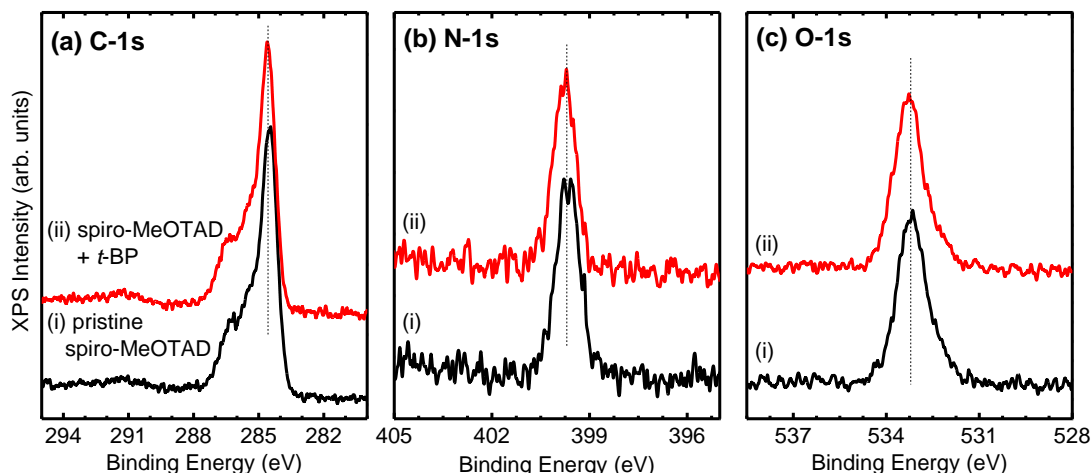
Figure 4.5 XPS spectra (Al−Kα = 1486.6 eV) corresponding to (a) C-1s, (b) N-1s, and (c) O-1s core levels of pristine spiro-MeOTAD film in comparison with spiro-MeOTAD with *t*-BP film

The LiTFSI dopants have characteristic signatures in the XPS[93] spectrum, such as Li and high oxidative-shifted carbon (−CF$_3$) (Figs. 4.3b,c), which enables unambiguous detection. The peak maximum of C-1s for the as-prepared LiTFSI-doped spiro-MeOTAD HTL was located at a BE of about 284.5 eV. For comparison, typical BE value of C-1s core level reported for the un-doped spiro-MeOTAD HTL is ~285.1−285.4 eV.[65, 80-81, 92] Thus, XPS results also confirmed that the LiTFSI dopants induced a E$_F$ shift towards the HOMO level by about 0.6−0.9 eV, consistent with p-type doping previously discussed for the UPS analysis (Fig. 4.1).

After 3 hours of ambient air exposure a new peak maximum appeared at ~688.6 eV that was attributed to F-1s of the −CF$_3$ groups in the LiTFSI dopants.[93] Such an observation suggests a re-distribution of the LiTFSI dopants within the LiTFSI-doped spiro-MeOTAD film to reach the top surface of the film, which is driven by the air exposure. Thus, as-prepared films seem to have phase segregated concentrations of LiTFSI and spiro-MeOTAD within the doped film. It would be expected that a high concentration of LiTFSI was initially located at the bottom region of the

film (i.e. the region that is close to the Au substrate). Upon air-exposure, LiTFSI starts to diffuse and segregate to the top surface of the film.

F-1s core level has a high atomic sensitivity factor (ASF=4.43) compared to the Li-1s with ASF of 0.06 and C-1s ASF of 1.[94] Therefore, the observed changes in the C-1s and Li-1s regions are very small (Figs. 4.3a,b(ii)). Clear signatures of the LiTFSI dopants were only observed after long period of exposure (18 hours, Fig. 4.3) with the Li-1s peak centered at ~56 eV, C-1s at 293 eV, and S-2p at ~170 eV (Fig. 4.4b).[65, 93, 95] The O-1s and N-1s core levels (Fig. 4.4) in agreement are with the picture of the segregation of LiTFSI dopants to the top-surface. In the S-2p core level region; the appearance of doublet peaks ($2p_{3/2}$ = 169.3 eV and $2p_{1/2}$ = 170.5 eV) due to spin-orbit splitting was observed with the initial 3 hours of ambient air exposure.[95] The S-2p core level photoemission was assigned to $-SO_2-$ group of the LiTFSI dopants.[95] In O-1s core level region, the as-prepared film showed two components, one centered at about 532 eV and the other at about 533 eV. The O-1s peak at 532 eV, belongs to the LiTFSI dopants and was detected in the as-prepared films due to the high ASF value of O-1s of 2.93. After 3 hours of air exposure, the lower BE shoulder at ~532 eV was observed to increase in intensity, which can be assigned to LiTFSI dopants.[95] The other high BE component was assigned to C_a–O–C group (where C_a corresponds to aromatic C) in spiro-MeOTAD molecule.[80] In the N-1s region (Fig. 4.3c) a gradual broadening of the peak with increasing of the air exposure period was observed. Two components were de-convoluted with one at 399.5 eV and the other at 400 eV, which can be assigned to C–N group in spiro-MeOTAD molecule and imide group in LiTFSI, respectively.[80, 95]

XPS for Li-1s and F-1s spectra measured on an as-prepared pure LiTFSI film (Fig. 4.6) show a peak position and overall shape similar to the doped spiro-MeOTAD HTL film. Thus, it is

expected that the majority of the LiTFSI dopants were found in its intact form (i.e, dissociation of Li from TFSI[96] was negligible, if any) in this experiments. A small peak corresponding to LiF compound was observed at higher BE in F-1s core level region (~685 eV) as well as TFSI at lower BE of ~402 eV in the N-1s core level region, both of which were a result of the decomposition of the LiTFSI dopants (Fig. 4.6) upon UV and X-ray exposures.[93]
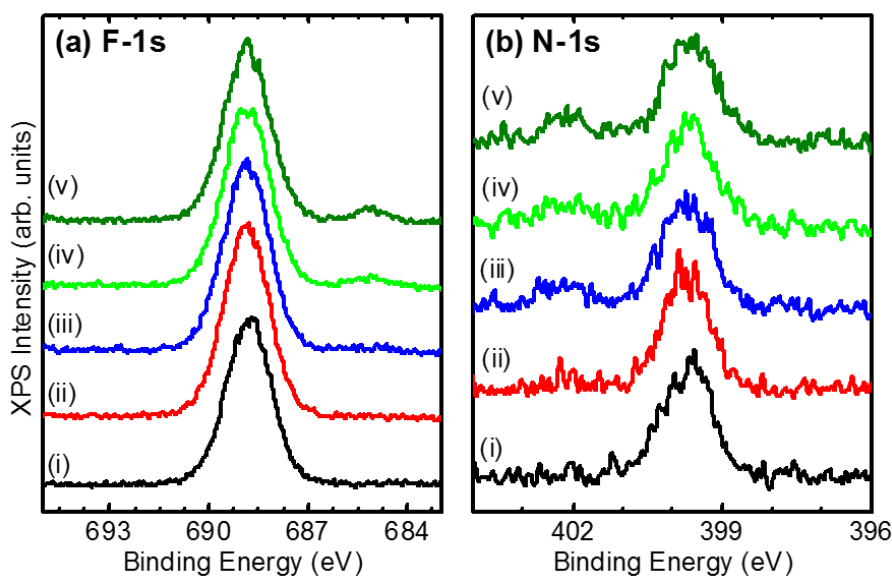
Figure 4.6 XPS spectra (Al−Kα = 1486.6 eV) corresponding to (a) F-1s, and (b) N-1s core levels of LiTFSI first scan (i), second scan (ii), third scan (iii), fourth scan (iv), and fifth scan (v)

Additional secondary processes were observed from the XPS analysis induced by ambient air exposure. For example, an additional peak in C-1s region centered at ~289 eV was observed after 6 hours of air exposure (Fig. 4.3a(iii)), which could be associated with air exposure related contamination, such as aerosols.[91] At the moment, it is difficult to assign the observed peak. A similar peak was reported[65, 97-99] and assigned as the oxidized form of the spiro-MeOTAD. In

addition, the C-1s peak maximum at 284.4 eV corresponding to C−H carbon in spiro-MeOTAD[80-81] decreases substantially in intensity while in the BE range between ~285−287 eV (corresponding to carbon from C−C, C−N, and C−O in spiro-MeOTAD molecule) is less affected by the ambient air exposure. As described in the experimental section, caution was taken into account to minimize any possible X-ray or UV long time exposure when acquiring XPS and UPS on the films under study. Thus, the aforementioned secondary processes observed in the LiTFSI-doped spiro-MeOTAD (appearance of ~289 eV peak and significant decrease of the 284.4 eV peak in C-1s) are expected to be induced mainly from the ambient air exposure.

The effect of ambient air exposure over period of time on the LiTFSI-doped spiro-MeOTAD film surface induced by the presence of gas molecules were monitored by the quantitative analysis of the XPS data (Fig. 4.7). XPS relative atomic ratios of O-1s, N-1s, C-1s, F-1s, S-2p and Li-1s were calculated by summing the integrated peak area values of all species in each region followed by normalization on the basis of the respective ASF values. Each spiro-MeOTAD molecule is composed of 4 N atoms, 8 O atoms, and 81 C atoms (Fig. 3.1). The *t*-BP molecules, as discussed previously in the XPS results, facilitates the solubility of the LiTFSI dopants, and mostly expected to desorb from the surface when transferred into vacuum.[87] In the case of LiTFSI dopants, each molecule is composed of 6 F atoms, 4 O atoms, 2 C atoms, 1 Li atom, 1 N atom, and 2 S atoms (Fig. 3.1). A clear increase in F-1s, O-1s, S-2p, and Li-1s atomic ratios was observed as ambient air exposure period increases, meaning that a dynamic process of re-distribution of the LiTFSI to the top-surface takes place. On the other hand, the atomic ratios of C-1s and N-1s decrease substantially. If LiTFSI molecules segregate to the top surface in their intact form, then the atomic ratios of C-1s and N-1s from the dopant would be expected to increase, but if one LiTFSI molecule displaces a spiro-MeOTAD molecule then the overall atomic ratios of C-1s should decrease. On

the other hand, it is difficult to expect the overall ratio of N-1s without knowing each component concentration on the surface. Therefore, the secondary processes cannot be neglected. As described previously, the photoemission spectroscopy analysis upon ambient air exposure was complex due to the different gas molecules present in ambient air (N_2, O_2, H_2O, CO_2, etc.). Moreover, special care in XPS analysis has to be taken into account, considering the effects of adventitious carbon compounds typically assigned as contamination in the literature.[97-99] To pin-point the gas element(s) responsible for the segregation of the LiTFSI and unravel the observed secondary processes, further systematic studies to expose the LiTFSI-doped spiro-MeOTAD HTL films under controlled environments of O_2, H_2O + N_2, and synthetic air are currently under further investigation.
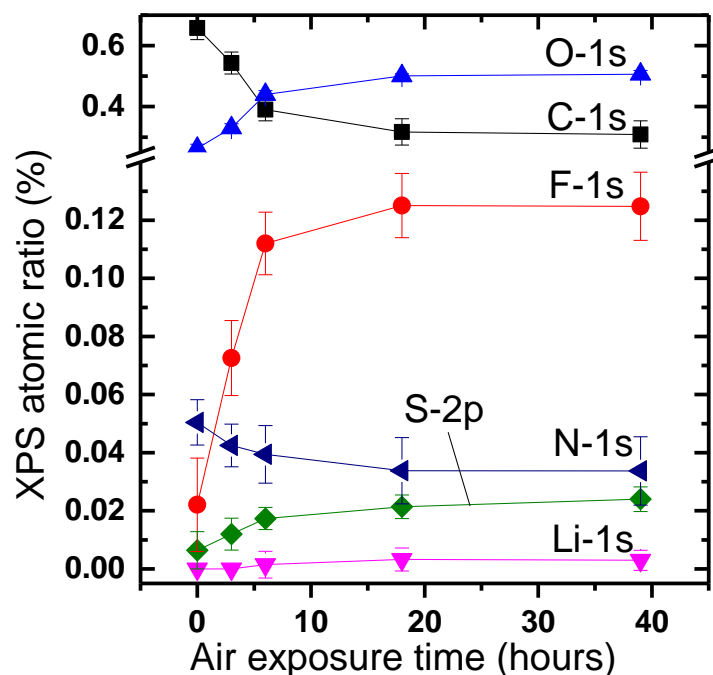
Figure 4.7 XPS atomic ratio variations for C-1s, O-1s, S-2p, N-1s, Li-1s and F-1s when doped spiro-MeOTAD is exposed to air.

4. 5.   Chemical and Electronic Changes under Controlled Environments of O_2 and N_2

As control environments and to make sure that the previously discussed results are induced by ambient air exposure, two other sets of experiments were carried out in presumably inert environments of nitrogen and vacuum. XPS core levels or HOMO leading edges of the doped spiro-MeOTAD films when samples were kept in vacuum or in dry N_2 environment did not show any chemical or electronic changes (Fig. 4.8, 4.9, 4.10, and 4.11).
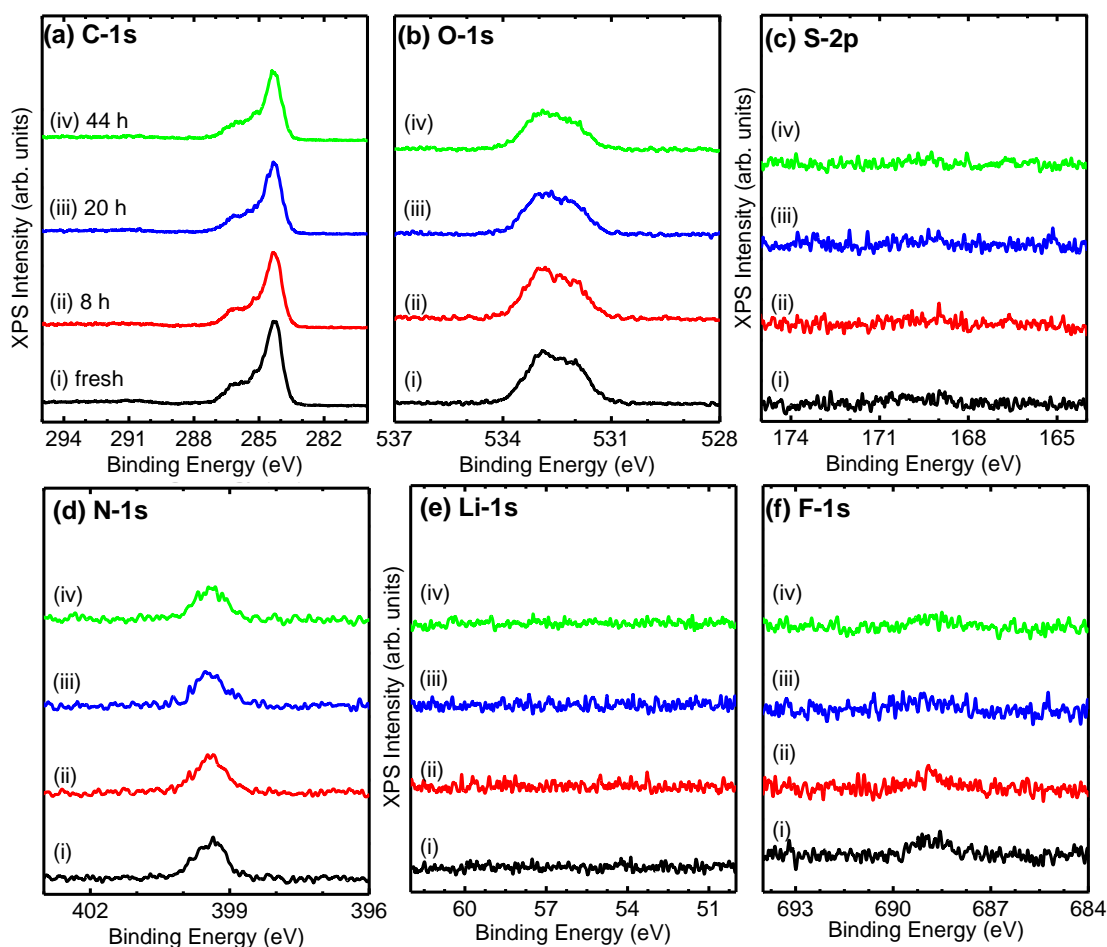
Figure 4.8 XPS spectra (Al−Kα = 1486.6 eV) corresponding to (a) C-1s, (b) O-1s, (c)S-2p, (d) N-1s, (e) Li-1s and (f) F-1s core levels of the doped spiro-MeOTAD films as prepared(i), after 8 hours vacuum (ii), after 20 hours vacuum (iii), and after 44 hours vacuum (iv)
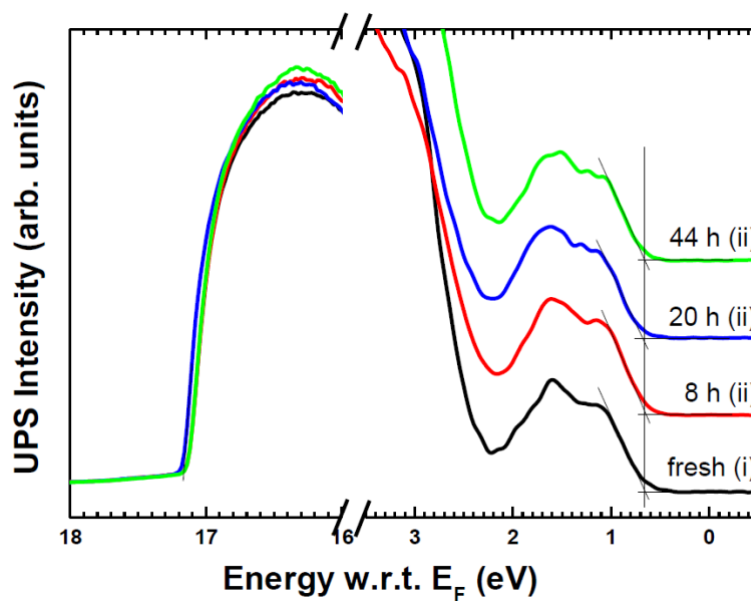
Figure 4.9 UPS spectra (He−Iα = 21.22 eV) corresponding to the cut off region and the HOMO region of doped spiro-MeOTAD films as prepared(i), after 8 hours vacuum (ii), after 20 hours vacuum (iii), and after 44 hours vacuum (iv)
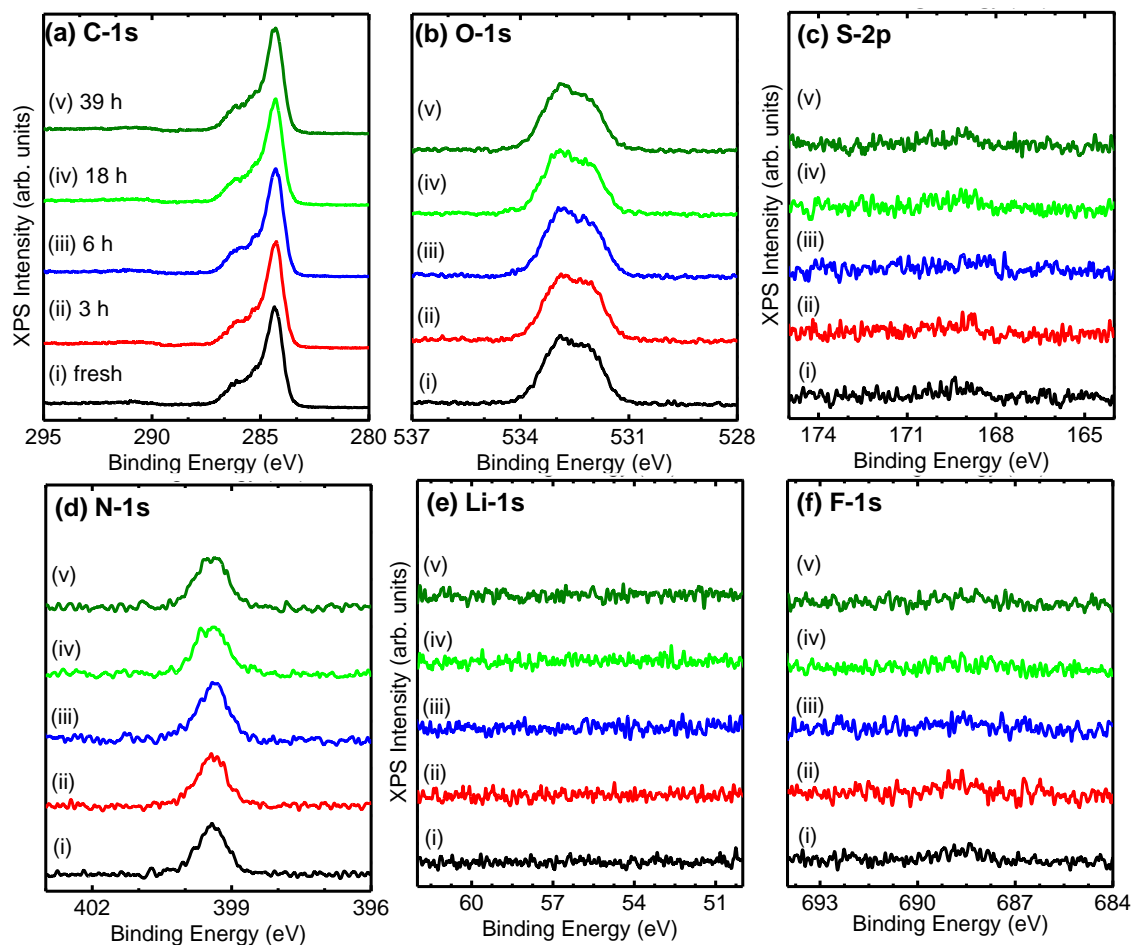
Figure 4.10 XPS spectra (Al−Kα = 1486.6 eV) corresponding to (a) C-1s, (b) O-1s, (c)S-2p, (d) N-1s, (e) Li-1s and (f) F-1s core levels of the doped spiro-MeOTAD films as prepared(i), after 3 hours N_2 exposure (ii), after 6 hours N_2 exposure (iii), after 18 hours N_2 exposure (iv), and after 39 hours N_2 exposure (v)
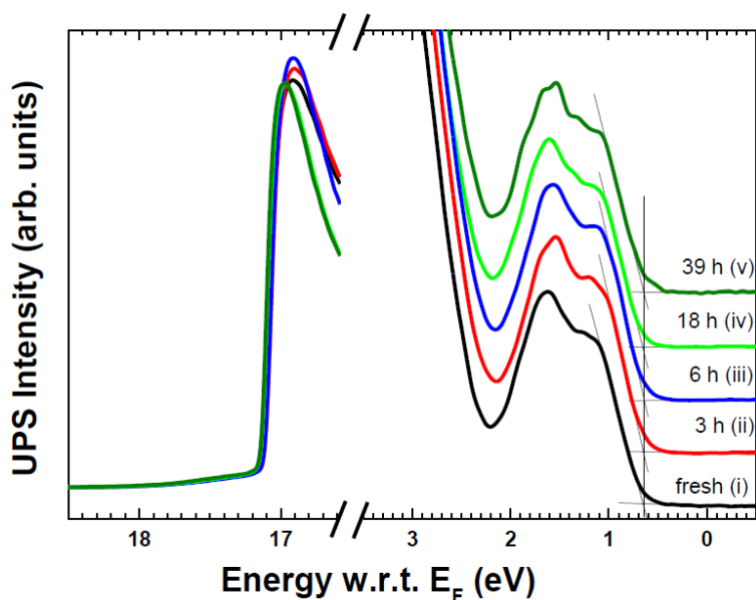
Figure 4.11 UPS spectra (He−Iα = 21.22 eV) corresponding to the cut off region and the HOMO region of doped spiro-MeOTAD films as prepared(i), after 3 hours N_2 exposure (ii), after 6 hours N_2 exposure (iii), after 18 hours N_2 exposure (iv), and after 39 hours N_2 exposure (v)

4. 6. Summary

In summary, the XPS results reveal that freshly prepared LiTFSI-doped spiro-MeOTAD HTL shows a very low concentration of LiTFSI dopants at the top surface of the HTL film. In addition, ambient air exposure causes some characteristic elements (e.g. F, S, and Li) belonging to LiTFSI dopants to migrate to the top surface of the HTL film. This migration across the bulk film seems to be facilitated by the two types of pinholes with different sizes that were discussed in chapter 3 and were confirmed by AFM, SEM, and optical microscopy. UPS results revealed the evolution of the energy levels of the LiTFSI-doped spiro-MeOTAD upon ambient air exposure, which are highly dependent on the spatial redistribution of the LiTFSI dopants within the HTL film. Further XPS results corroborates this interpretation. The results of this study raised more questions about what is the constituent component in ambient air that induces the movement of the LiTFSI dopants. Similarly, does the ambient air exposure result in a complete segregation of the dopants to the top surface of the HTL or does it result in a redistribution of the dopants which would result in an enhancement of the bulk properties. These questions will be answered in the next chapter.

Chapter 5: H$_2$O and O$_2$ Effects on Chemical and Electronic Properties of Doped Spiro-MeOTAD[100]

5. 1.   Introduction

As discussed previously, the replacement of the liquid electrolyte HTL with LiTFSI-doped spiro-MeOTAD HTL[8-9, 31, 67-68] substantially improved the PCEs of the perovskite solar cells. The addition of the LiTFSI dopants substantially enhanced conductivity of the HTL.[87-88, 101-103] LiTFSI is a commonly employed dopant for many other HTLs such as PTAA,[104-105] P3HT,[106-107] PIF8-TAA,[108] and PTB7[109] in perovskite solar cells. The top electrode and the underneath LiTFSI-doped spiro-MeOTAD HTL are usually the most affected by external environmental conditions (O$_2$, H$_2$O, N$_2$, temperature, and light).[66, 110-113] DSSCs with doped spiro-MeOTAD as HTL need to be fabricated in air in order to work.[87, 114-115] Similarly, for perovskite solar cells it is common practice to expose the device to air for many hours after fabrication in order to obtain high PCEs.[114-115] Ambient air exposure results in electrical conductivity improvement of LiTFSI-doped spiro-MeOTAD and was reported to be associated with oxidation reaction induced by light exposure.[87-88, 116]

Additional chemical synthesis steps were also carried out employing AgTFSI to prepare readily oxidized spiro-MeOTAD.[85] Replacement of the doped spiro-MeOTAD HTL was

demonstrated using inverted solar cell structure with inorganic HTL, but additional processing steps and high temperature treatment were needed.[117]

As discussed in chapter 3, the standard preparation method for the spin-coated LiTFSI-doped spiro-MeOTAD HTL films generate a high density of pinholes with an average diameter of ~135 nm. These pinholes form channels across the entire LiTFSI-doped spiro-MeOTAD HTL films. These pinholes are believed to accelerate diffusion of gas molecules from ambient air into the perovskite layer in perovskite-based solar cells as well as facilitate the outward diffusion of chemical elements/compounds such as LiTFSI, which is hygroscopic. Based on the AFM results these pinholes were observed to be partially filled up upon time of ambient air exposure.

In chapter 4, it was revealed using photoemission spectroscopy techniques that these pinholes were partially filled up with the LiTFSI dopants upon ambient air exposure. The movement of the LiTFSI dopants to top surface of the LiTFSI-doped spiro-MeOTAD film was found to substantially enhance the energy level alignment in the perovskite solar cells. However, the constituent component from ambient air that induced this movement of the LiTFSI dopants was not clear. In addition, the oxidation reactions that happen and were proposed previously for LiTFSI-dope spiro-MeOTAD[87-88, 116] needs more investigations after the direct observation of the dopants movement that was discussed in the previous chapter. Efforts have been made to better understand environmental effects on LiTFSI-doped spiro-MeOTAD films.[66, 81-86] However, a clear understanding of the LiTFSI dopant re-distribution process and resulted effects is still lacking. It is crucial to study LiTFSI-doped spiro-MeOTAD charge dynamics under controlled environmental conditions to understand the overall current-voltage behavior of perovskite solar cells.[118-119]

5. 2.   Experimental Methods

LiTFSI-doped spiro-MeOTAD precursor solution and spin-coated films were prepared in the same way as previously discussed in chapter 3, section 2. The final thickness of doped spiro-MeOTAD films were approximately 250 nm, determined by a profilometer.

For the effect of environmental H_2O vapor, the relative humidity was 90% that is generated by letting a stream of dry nitrogen gas flow through a H_2O bubbler. As for the effect of O_2, high purity dry oxygen gas (>99.5%) was used. The exposure was performed in stainless-steel containers at a pressure of 1 atm.

Electronic properties of doped spiro-MeOTAD films were characterized with an UPS (He−Iα = 21.22 eV). Chemical states of doped spiro-MeOTAD films were characterized by XPS (monochromated Al Kα = 1486.6 eV). Details of XPS/UPS measurements and analysis were discussed in chapter 4, section 2.

5. 3.   Chemical Changes (XPS)

In order to find out the main component in air that drives the redistribution of LiTFSI across spiro-MeOTAD films upon air exposure, LiTFSI-doped spiro-MeOTAD HTL films were exposed to controlled environments of H_2O vapor with RH of 90% (with nitrogen as carrier gas), and dry O_2 gas (Fig. 5.1). Afterward, the chemical states of the exposed doped spiro-MeOTAD films were studied using XPS. In F-1s and S-2p core levels regions (Fig 5.1a, b, d, e), as-prepared samples showed small peaks at ~688.7 eV and ~169.4 eV in the BE scale, respectively, and were assigned to LiTFSI dopants (chapter 3, Fig. 3.1).[93] Gradual increases of the peaks in both of F-1s and S-2p were observed when samples were exposed to H_2O vapor. In contrast, no changes in the XPS peak

intensities for F-1s and S-2p core levels when samples were exposed to oxygen. This observation clearly shows that the re-distribution of LiTFSI dopants within the doped spiro-MeOTAD film to reach the top surface is mainly because of the H_2O vapor exposure.

Unlike ambient air exposure,[66] H_2O vapor or oxygen exposure showed no changes in the spectra of the five components corresponding to the core level of C-1s (C−H, C−C, C−N, aromatic C_a−O, and C−O) (Fig. 5.1c, f) of spiro-MeOTAD molecule. In comparison with C-1s core level of LiTFSI-doped spiro-MeOTAD films when exposed to ambient air,[66] H_2O vapor- and O_2-exposure did not show decreased C-1s core level intensity.
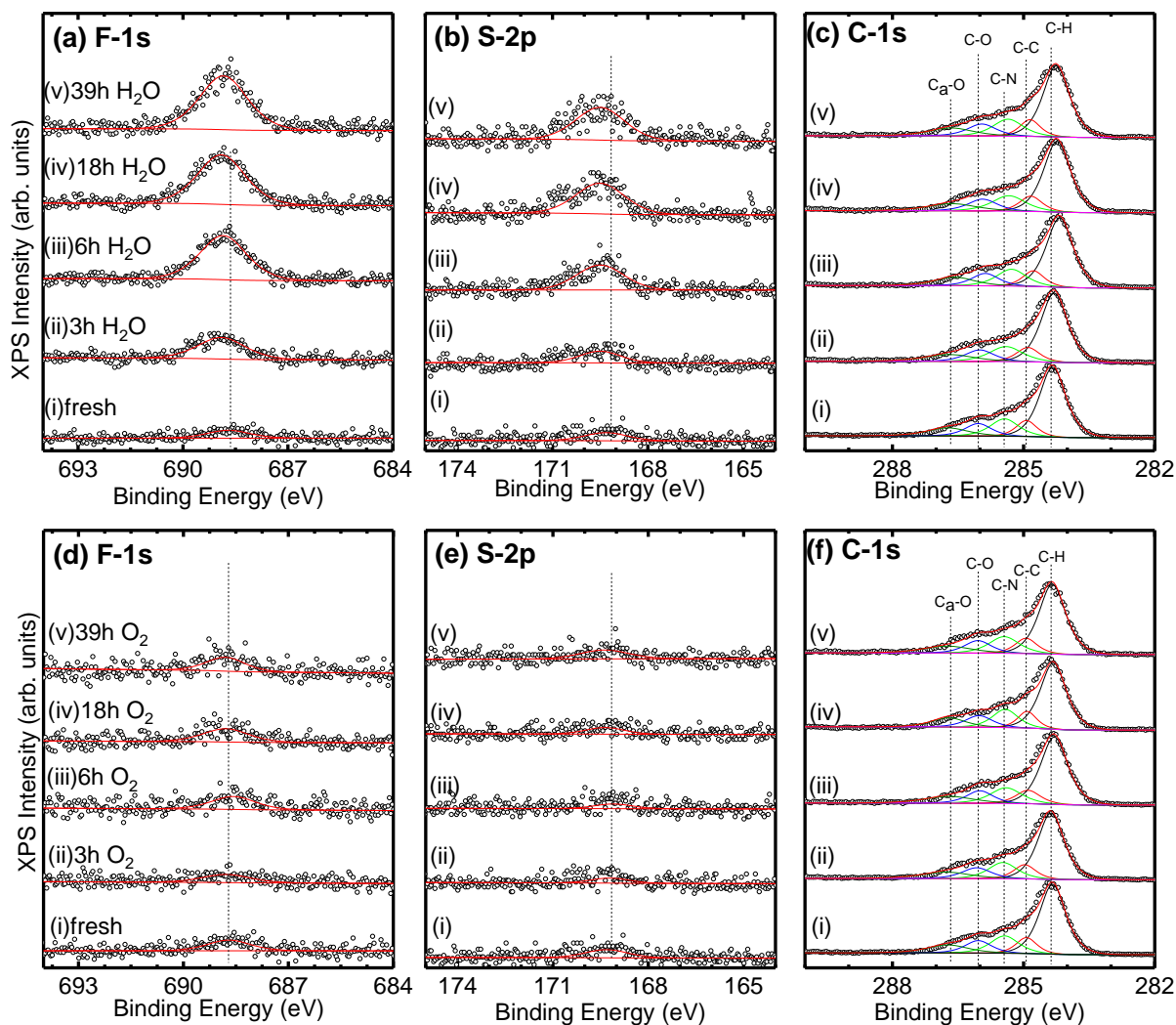
Figure 5.1 LiTFSI re-distribution across the spiro-MeOTAD HTL upon H_2O vapor exposure. XPS spectra (Al−Kα = 1486.6 eV) corresponding to (a,d) F-1s, (b,e) S-2p, and (c,f) C-1s core levels of H_2O vapor-exposed films (a-c) and O_2-exposed films (d-f). (i) As-prepared doped spiro-MeOTAD films, before and after (ii) 3 h, (iii) 6 h, (iv) 18 h, and (v) 39 h H_2O vapor or O_2 exposures.

Similarly, the core levels of O-1s and N-1s under the controlled environments of H_2O and O_2 were monitored (Fig. 5.2). The lower BE peak in the core level region of O-1s was increased in both of the exposures.
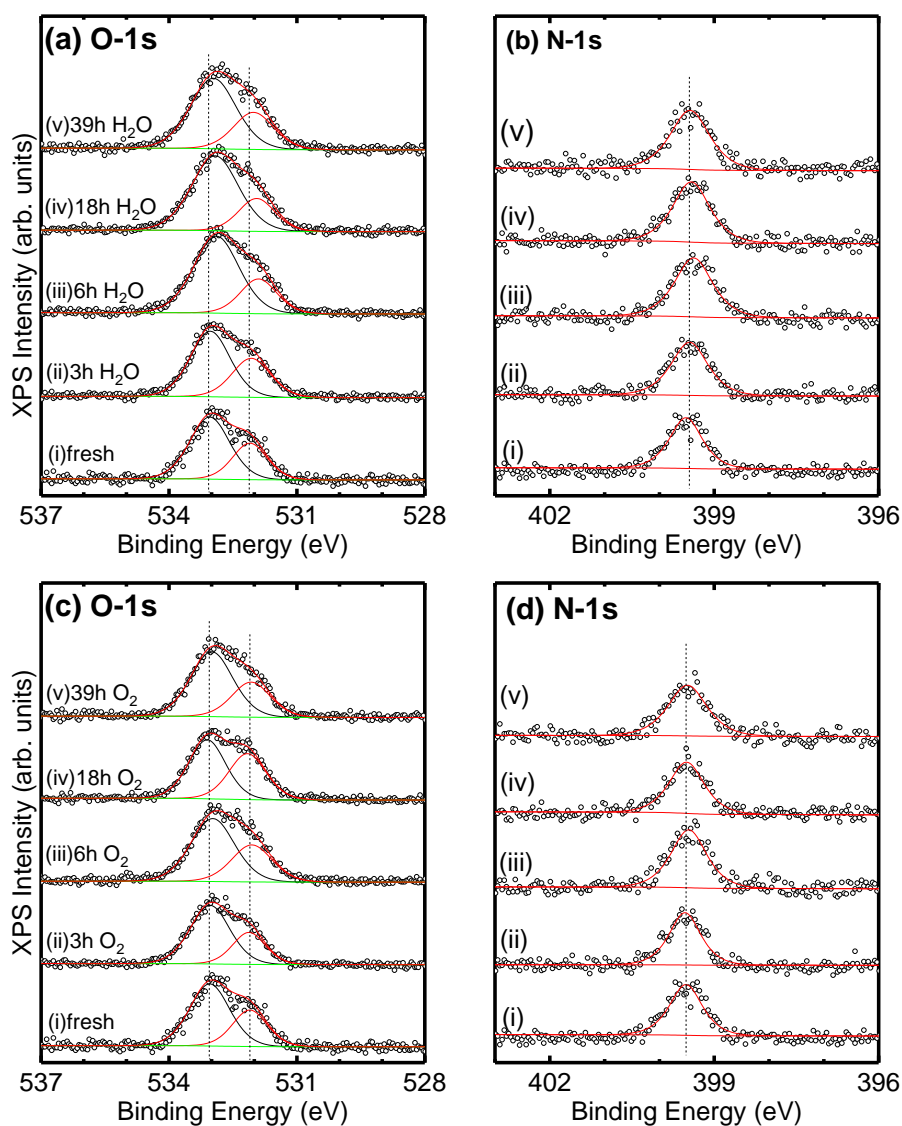
Figure 5.2 XPS spectra (Al−Kα = 1486.6 eV) corresponding to (a,c) O-1s, and (b,d) N-1s core levels of H_2O vapor- (a,b) and O_2-exposed (c,d) films. (i) as-prepared doped spiro-MeOTAD films and after exposures of (ii) 3 h, (iii) 6 h, (iv) 18 h, and (v) 39 h to H_2O vapor or O_2.

5. 4.   **Electronic Changes (UPS)**

Electronic changes of the as-prepared, LiTFSI-doped spiro-MeOTAD films before and after oxygen and H_2O vapor (RH 90%) exposures, were investigated using UPS (He−Iα source, Fig. 5.3). For H_2O vapor exposure, the leading edge of the HOMO level for the LiTFSI-doped spiro-MeOTAD film, with respect to E_F, showed a gradual shift of ~0.1 eV to lower BE (Fig 5.3a, b). The observed shift of HOMO leading edge suggests p-doping of spiro-MeOTAD in the presence of the LiTFSI dopants and H_2O vapor. On the other hand, only subtle change of <0.1 eV was observed in the case of oxygen exposure (Fig. 5.3c, d). At first glance, the foregoing results of oxygen exposure indicated that p-doping by oxygen is difficult. However, spiro-MeOTAD molecules were p-doped in the case of H_2O vapor exposure. As will be discussed in detail in the next chapter, I-V measurements conducted on oxygen-exposed LiTFSI-doped spiro-MeOTAD films showed higher initial conductivities than the samples that was exposed to H_2O vapor. This great difference is explained by taking into account the pressure gap between the two analytical techniques: I-V measurements were conducted in nitrogen environment (1 atm) while photoemission spectroscopy measurements were conducted under ultrahigh vacuum with base pressure of ~10^{-10} Torr. It is expected that the majority of physisorbed O_2 molecules into spiro-MeOTAD film desorb under UHV environment.[120] Thus, care should be taken when discussing energy levels of oxygen exposed LiTFSI-doped spiro-MeOTAD films.
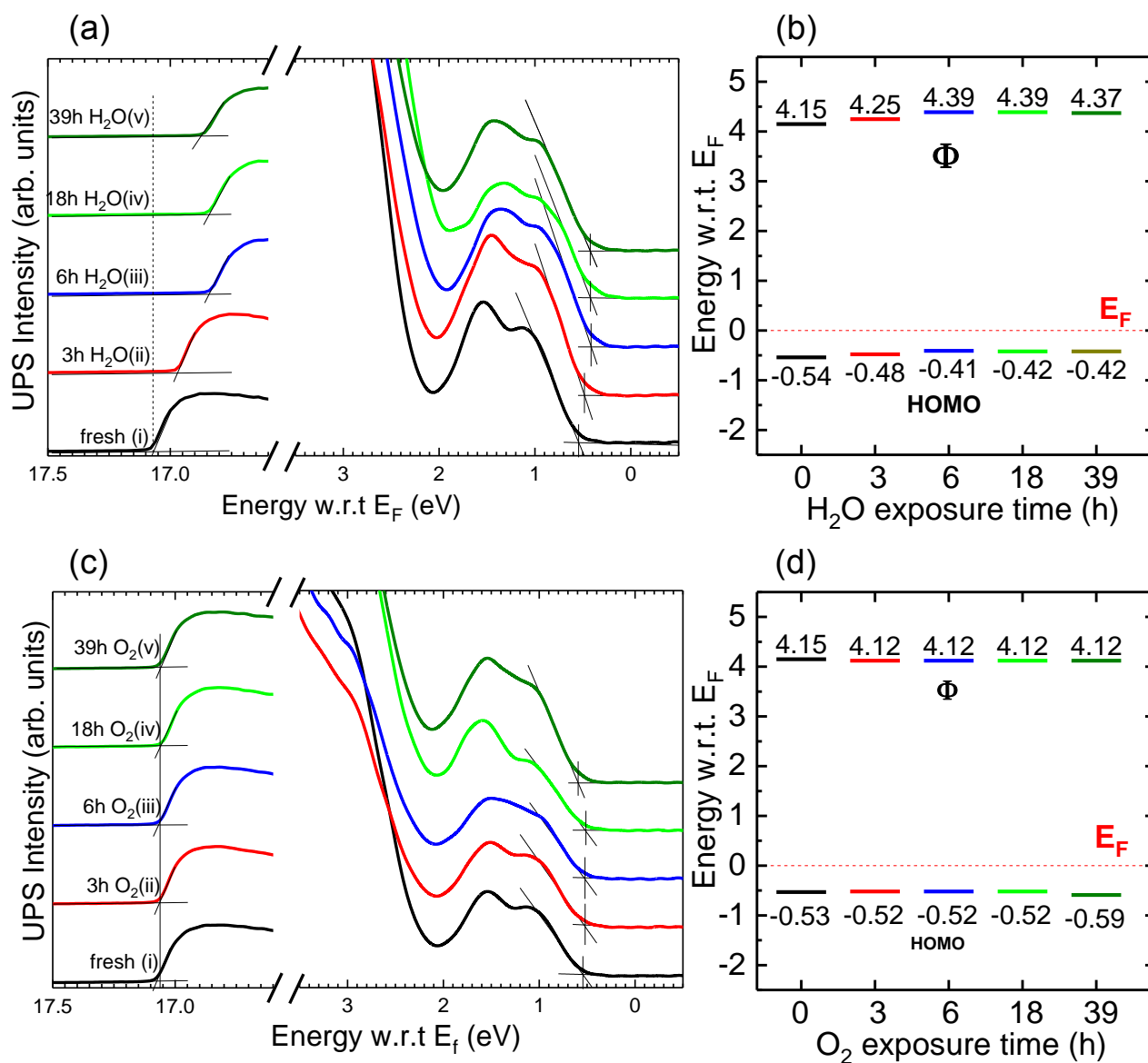
Figure 5.3 (a, c) UPS spectra (He−Iα = 21.22 eV) corresponding to the cut-off region, and HOMO region of the as-prepared doped spiro-MeOTAD film (i) and the same sample when exposed for 3 h (ii), 6 h (iii), 18 h (iv), and 39 h (v) to H₂O vapor and O₂, respectively. (b, d) Corresponding schematic energy diagram of doped spiro-MeOTAD film.

A clear leading edge of the HOMO level was observed in both of the H_2O vapor and O_2 exposure even after long period of 39 h of exposure. A distinctively different observation from that of ambient air-exposed doped spiro-MeOTAD, which showed a complete disappearance of the HOMO leading edge after 18 h of exposure.[66] The work function values were calculated from the cutoff edges at the high BE side of the UPS spectra (Fig. 5.3). Oxygen exposed films showed no changes, but a high shift of ~0.2 eV to lower BE were observed in the case of H_2O vapor exposed films, suggesting p-doping. The ionization energy was calculated to be 4.68 eV for the as-prepared LiTFSI-doped spiro-MeOTAD films (Fig. 5.3b, d) and was observed to increase as a function of H_2O vapor exposure time, reaching a saturation value of 4.8 eV after 6 h of H_2O vapor exposure. The ionization energy value for the films exposed to oxygen were constant throughout the entire oxygen exposure times (IE = 4.64 − 4.71 eV), corroborating the XPS measurements where the detection of the LiTFSI dopants was very low (Figure 5.1d, e).

5.5. Summary

In summary, H_2O was revealed as the constituent component that drives the movement of the LiTFSI dopants across the LiTFSI-doped spiro-MeOTAD HTL films, which eventually leads to enhanced PCEs in perovskite solar cells. XPS measurements revealed that H_2O vapor exposure (RH 90%, N_2 as carrier gas) is the main component in ambient air that leads to the movement of the LiTFSI dopants across the whole spiro-MeOTAD HTL. However, the UPS measurements showed that the H_2O vapor exposure and the oxygen exposure are different from that of ambient air exposure which caused a complete disappearance of the HOMO features as discussed in the previous chapter. XPS measurements also revealed that dry O_2 exposure does not affect the LiTFSI in the HTL film and does not oxidize the film. However, when the sample were exposed to dry O_2, specially with long exposure periods, a physiosorption effect was observed. Finally, it is still not

clear whether LiTFSI dopants completely segregates to top surface of the spiro-MeOTAD HTL or it re-distributes across the entire HTL film upon ambient air exposure or H$_2$O vapor exposure, which will be addressed and discussed in the next chapter.

Chapter 6: Electrical Property Changes of Doped Spiro-MeOTAD under Different Environmental Conditions[100]

6. 1. Introduction

As discussed previously, power conversion efficiencies in perovskite solar cells enhanced substantially after incorporating spiro-MeOTAD, also the enhanced PCEs resulted from the addition of LiTFSI dopants to the spiro-MeOTAD, which is known to substantially enhance the conductivity of the HTL.[87-88, 101-103] In perovskite solar cells it is common practice to expose the device to ambient air for several hours after fabrication to obtain high PCEs.[114-115] Ambient air exposure results in electrical conductivity enhancement of LiTFSI doped spiro-MeOTAD and is associated with oxidation reaction induced by light exposure. [87-88, 116]

The standard preparation method for LiTFSI-doped spiro-MeOTAD films generate a high density of pinholes. These pinholes form channels that wiggle within the spiro-MeOTAD film, and are thought to accelerate diffusion of gas molecules from ambient air such as H_2O and O_2 into the perovskite layer.[66] as well as the outward diffusion of chemical elements/compounds such as LiTFSI.

H_2O vapor is the constituent component in ambient air that drives the movement of the LiTFSI dopants. However, a clear understanding of the LiTFSI dopant re-distribution process and whether it is a re-distribution across the entire HTL or segregation to top surface is still lacking. Similarly, the effect of the redistribution of the dopants or segregation to top surface on the electrical bulk properties is crucial to be understood. Therefore, it is important to study LiTFSI-doped spiro-MeOTAD charge dynamics under controlled environmental conditions to understand the overall current-voltage behavior of perovskite solar cells.[118-119]

In this chapter, the effects of environmental effect H_2O vapor with a relative humidity of 90% that is generated by letting a stream of dry N_2 gas flow through a H_2O bubbler, high purity dry O_2 gas (>99.5%), and ambient air (RH 50%) on the electrical properties of hole-only devices of LiTFSI-doped spiro-MeOTAD films, using mercury drop I-V measurements is investigated.

6. 2.   Experimental Methods

Doped spiro-MeOTAD solution was prepared as discussed in previous chapters. The corresponding molar ratios of spiro-MeOTAD: LiTFSI: t-BP were 1: 0.54: 3.33 based on nominal concentrations. For I-V measurements, thin films of doped spiro-MeOTAD were prepared by spin-coating in the nitrogen glove-box for 60 s at 2000 rpm. Spin-coating was performed on thermally evaporated 100 nm of Au on heavily doped Si substrates with a thin native oxide layer. The final thickness of the LiTFSI-doped spiro-MeOTAD HTL was ~250 nm, determined by a profilometer.

The I-V measurement system consists of a modified 663 VA Stand (Metrohm), which is often used for voltammetry measurements and a 4200-SCS Keithley semiconductor characterization system. Reproducible and size-controlled mercury drops were formed at the end

of a silanized glass micro-capillary ($\phi = 50$ μm) using 663 VA Stand. The two I-V electrodes were connected to Hg-reservoir and to the sample substrate (Au electrode) with the aid of a micrometer-controlled x-y-z stage, and were connected to a low-noise Keithley I-V measurement system. All I-V measurements were performed in a nitrogen glove-box at room temperature. The final device configuration was Hg-drop electrode/LiTFSI-doped spiro-MeOTADHTL/Au electrode. The top Hg-drop electrode was about 540 μm in diameter. The top Hg-drop and the bottom Au electrodes had similar work functions of about 4.5 eV, which confirms a hole-only device configuration.[121-124] A home-made nitrogen-filled containers of stainless-steel were used to transport the samples from the nitrogen-glove box (for conductivity measurements) to the deionized H_2O+N_2 (RH 90%) and dry-O_2 gases exposure systems and vice-versa. Conductivity was extracted using **equation (1)**.

$$\sigma = \frac{d}{RA} \tag{1}$$

Where d is the thickness of the film in centimeters, R is the electrical resistance in Ohm, and A is the cross-sectional area in square centimeters. The mobility was extracted using SCLC model, **equation (2).**

$$J = \frac{9}{8} \varepsilon \varepsilon_o \mu_e \frac{V^2}{d^3} \tag{2}$$

Where ε for organic semiconductors is 3,[125] ε_o is the permittivity of free space, μ_e is the mobility, V is the voltage, and d is the thickness of the film.

6. 3.   Conductivity Changes under Different Environmental Conditions

Controlled environmental gas exposures to dry oxygen, H_2O vapor (RH 90%), and ambient air (RH 50%) were carried out on hole-only devices to investigate conductivity changes of the LiTFSI-doped spiro-MeOTAD HTL films. The hole-only devices were fabricated by using high work function materials as electrodes (e.g. Au, Hg), which presumably resulted in a close energetic alignment between the HOMO level of LiTFSI-doped spiro-MeOTAD layer and the E_F of the electrodes. In the hole-only devices, electrical current flowing through the devices are expected to be primarily caused by holes conduction.[121, 123-124]

The device consisted of an Au electrode/LiTFSI-doped spiro-MeOTAD/hanging mercury drop electrode. The Au electrode was connected to a positive bias and the Hg-drop electrode was connected to ground. This configuration leads to holes injection from the Au electrode to the spiro-MeOTAD film (Fig. 6.1a, inset). The hanging Hg-drop system allowed conductivity measurements directly on the HTL films without the need to deposit a top electrode metal or new samples for every measurement.[126] J was recorded under an applied electric field, from which the conductivities (σ) were calculated and plotted for the as-prepared, air (RH 50%), H_2O vapor (RH 90%), and dry oxygen-exposed, LiTFSI-doped spiro-MeOTAD films (Fig. 6.1a-c). As shown in chapter 5, XPS showed that LiTFSI-doped films need about 6 h of H_2O vapor exposure for LiTFSI to be detected on the top of HTL film. Based on the XPS results, LiTFSI-doped films were exposed to the above mentioned controlled environments for 6 h at the beginning, and followed by additional 18 h of exposure (24 h total). As-prepared LiTFSI-doped spiro-MeOTAD films showed conductivity values of about 10^{-9} ($\Omega \cdot cm)^{-1}$ at an electric field of $<10^4$ V/cm (Fig. 6.1a-c).
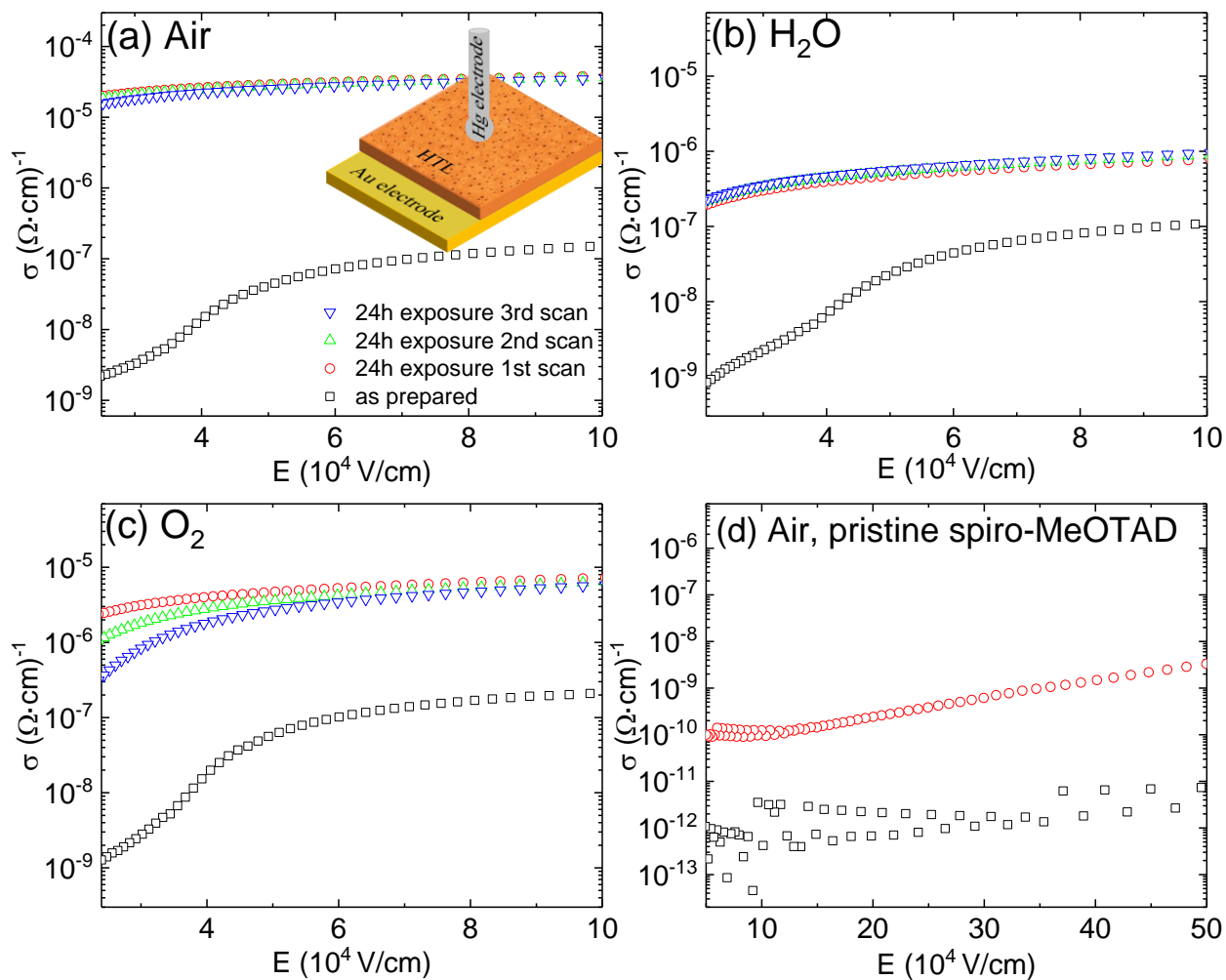
Figure 6.1 Enhanced conductivities upon H_2O vapor and O_2 exposures. Semi-log plots of conductivity versus electric field of as-prepared doped spiro-MeOTAD films before and after 24 h exposure to (a) ambient air, (b) H_2O vapor, and (c) O_2, and (d) as-prepared undoped spiro-MeOTAD after 1day of air exposure. The inset shows the hole-only device. In each figure, red, green, and blue curves represent the first, second, and third scans, respectively.

Interestingly, I-V results showed that 6 h of exposure to ambient air, H_2O vapor, or oxygen, substantially increased the electrical conductivity of the HTL films, especially at low electric field. The additional 18 h of ambient air, H_2O vapor, or oxygen exposure also caused another substantial increase in the electrical conductivity (Fig. 6.2). The samples that were exposed to ambient air showed a conductivity increase of more than three orders of magnitude, while individually, oxygen and H_2O vapor exposed films showed an increase of two orders of magnitude. Dry-oxygen exposed samples showed higher σ values compared to those from H_2O exposed samples. Abate et al.[79] proposed an equilibrium between spiro-MeOTAD and O_2 and oxidized spiro-MeOTAD$^+$ (spiro-MeOTAD + O_2 $\leftrightarrow$ spiro-MeOTAD$^+$·O_2^-) and they proposed that the equilibrium can be moved forward in the presence of LiTFSI dopants where the superoxide O_2^- reacts with Li^+ ions to form Li_2O and Li_2O_2 and then generating a stable spiro-MeOTAD$^+$·TFSI$^-$ (spiro-MeOTAD$^+$·O_2^- + LiTFSI $\leftrightarrow$ spiro-MeOTAD$^+$·TFSI$^-$ + Li_xO_y). The presence of spiro-MeOTAD$^+$·O_2^- and spiro-MeOTAD$^+$·TFSI$^-$ are associated with high σ. [66, 79, 87-88, 116] In the presence of oxygen or H_2O vapor, there are O_2 molecules, H^+, and OH^- ions, which are available for oxidation or reduction reactions. The redox reaction is expected to play a major role in determining the conductivity of the LiTFSI-doped spiro-MeOTAD HTL films. De Leeuw et al. reported that H_2O can easily attack charged p-type organic semiconductors in a reaction which reduces H_2O and leading into neutral organic semiconductors.[127-128] The analysis of σ of the LiTFSI-doped spiro-MeOTAD HTL films when it is exposed to ambient air and compared to individual exposures of dry oxygen and H_2O vapor is complex. Non-linear relationship is obtained as σ of the ambient air exposed films is much higher (one order of magnitude) than the summation of the individual H_2O vapor and oxygen exposed spiro-MeOTAD HTL films. It is noteworthy to mention that additional experiments are needed and crucial to understand the fundamental aspects of simultaneous effect of H_2O and O_2 molecules

interactions with LiTFSI-doped spiro-MeOTAD films. However, σ behaved differently in subsequent I-V measurements on the doped spiro-MeOTAD film. Oxygen exposed films showed a gradual decrease in σ with the subsequent I-V scans. After the third I-V scan, a decay of two orders in magnitude was obtained when compared to the first I-V scan (Fig. 6.1c). A small decrease (less than one order of magnitude) in σ was observed in the case of films exposed to ambient air (Fig. 6.1a). On the contrary, there was almost no decrease in σ in case of the H_2O vapor exposed films (Fig. 6.1b), indicating a stable, LiTFSI-doped spiro-MeOTAD molecules and/or complexes were formed; this is corroborated by the photoemission spectroscopy results discussed in chapter 5. In addition, un-doped spiro-MeOTAD films showed an increase in σ of 2 orders of magnitude after 24 h of ambient air exposure (Fig. 6.1d).
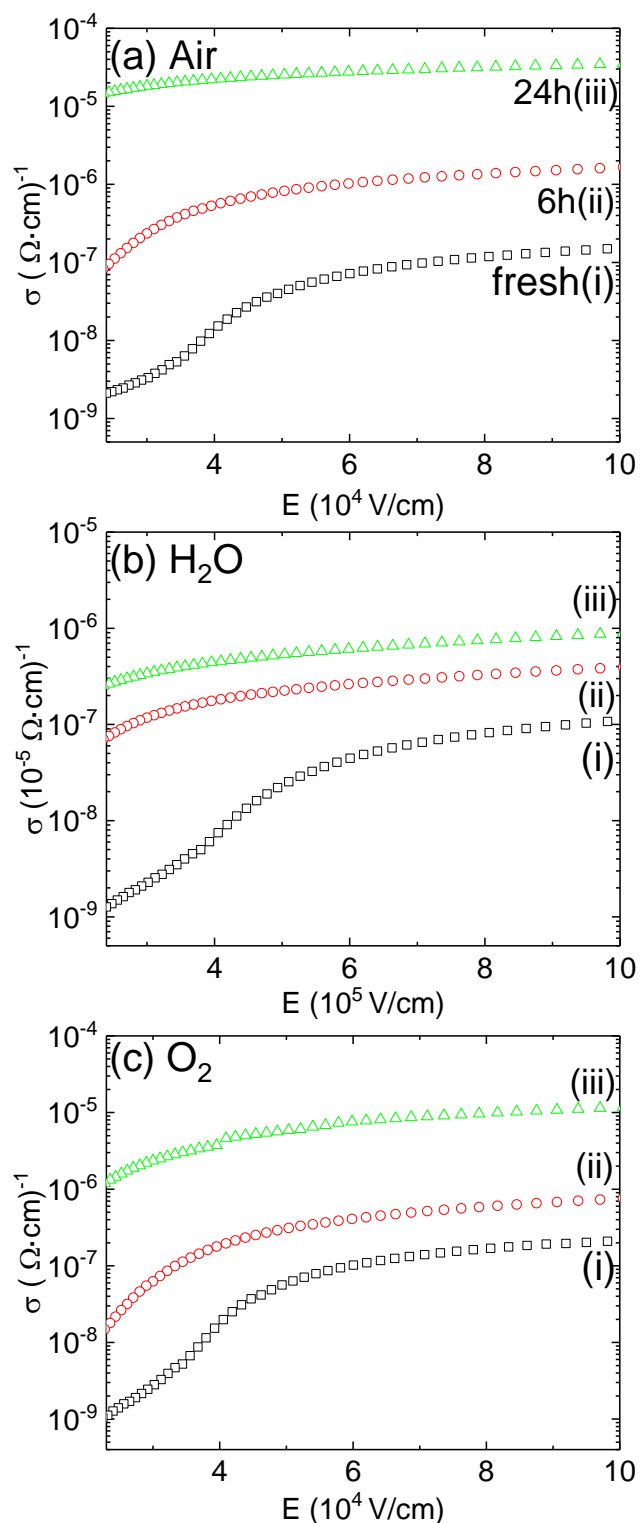
Figure 6.2 Semi-log plots of conductivity versus electric field of as-prepared doped spiro-MeOTAD (i), and after exposures of 6h (ii), and 24 h (iii) to ambient air (a), H_2O vapor (b), and O_2 (c).

6. 4.   Mobility Changes under Different Environmental Conditions

The changes in the mobility values of LiTFSI-doped spiro-MeOTAD HTL films using space charge limited current (SCLC) model[129] were also investigated (Fig. 6.3). In previous work by Ono et al.[80] the interactions of oxygen and H_2O gas molecules with pristine spiro-MeOTAD films were studied and showed deterioration in the hole mobility using organic field effect transistor devices. The new I-V data presented here from LiTFSI-doped spiro-MeOTAD were fitted to the SCLC model and then mobility values for these films were extracted. The mobility of the LiTFSI-doped spiro-MeOTAD HTL increased by two orders of magnitude (4.7×10^{-5} cm^2/V·s $\rightarrow$ 1.5×10^{-2} cm^2/V·s) after 24 h of ambient air exposure with RH of 50% (Table 6.1). The extracted mobility values of the ambient air-exposure are consistent with literature.[61] Interestingly, after 24 h of oxygen exposure, the increase in the mobility value was about an order of magnitude, but an approximately five-fold increase in the case of H_2O vapor exposed films with RH of 90% (Table 6.1). On the other hand, when the LiTFSI-doped films were exposed to oxygen, the current density decreased dramatically with the second and third I-V scans (Fig. 6.3b). In comparison, only a small decrease in the current density was observed in case of ambient air exposure (Fig. 6.3a) and no decrease was observed in the case of H_2O vapor exposure (Fig. 6.3c). These observations suggest that both H_2O vapor and oxygen have important roles in the enhancement of the electrical properties of LiTFSI-doped spiro-MeOTAD HTL, but the improvement induced by exposing the films to H_2O vapor is mainly caused by a re-distribution of the LiTFSI dopants (confirmed by XPS, chapter 5).[66] However, in the case of the oxygen exposure it seems that O_2 molecules serves as electron traps, resulting in p-doping of the spiro-MeOTAD films, which can be reversibly influenced by the applied bias.[130-131] On the other hand, it was difficult to extract mobility values

from the un-doped spiro-MeOTAD films, because of low current level and higher electric field was needed to reach the SCLC region.

Based on the previously discussed results, the enhancement of the mobility in case of ambient air exposure is a combination of different factors (i) LiTFSI additives redistribution across the HTL film, (ii) oxygen physisorbtion, and (iii) a distinctive effect from ambient air. The distinctive effect from ambient air can be associated with the coexistence of H_2O and O_2 that would promote oxidation of the spiro-MeOTAD. As previously presented in the XPS data in chapter 4, ambient air exposure resulted in a clear decrease of C-1s spectra (Fig 4.3a), which indicates an oxidation of the spiro-MeOTAD.[7] On the other hand, spiro-MeOTAD single crystals were observed to have higher mobility values.[7] At the same time spiro-MeOTAD thin films were observed to crystalize in ambient conditions, which would suggest increased mobility due to crystallization.[7] However, the influence of H2O+O2 as well as the influence of ambient air on the mobility needs more investigations.

	Mobility [cm^2/V·s]
As-prepared doped spiro-MeOTAD	4.7×10^{-5}
H_2O vapor exposed doped spiro-MeOTAD	6.1×10^{-4}
Dry O_2 exposed doped spiro-MeOTAD	5.0×10^{-3}
Ambient air exposed doped spiro-MeOTAD	1.5×10^{-2}

Table 6.1 Extracted hole mobility values of as-prepared spiro-MeOTAD films and those exposed to H_2O vapor, dry O_2, and ambient air.
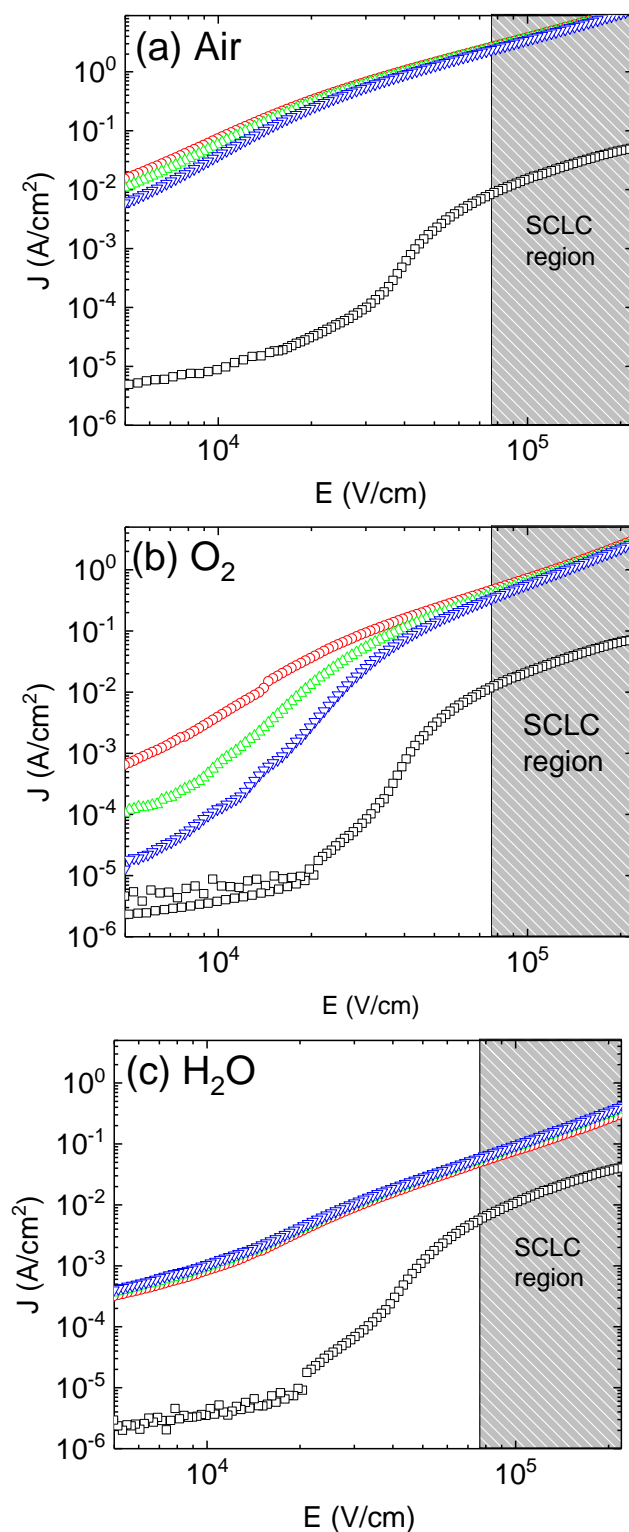
Figure 6.3 Mobility extraction from SCLC region. Log-log plots of current density (J) versus electric field (E) and voltage-square (V^2) of as-prepared doped spiro-MeOTAD films before and after 24 h exposure to (a) ambient air, (b) O_2, and (c) H_2O vapor.

6. 5. Summary

In summary, the mechanisms that drive the conductivity improvement of the LiTFSI-doped spiro-MeOTAD HTLs, that eventually leads to enhanced power conversion efficiencies in perovskite solar cells were revealed. The I-V measurements on the hole-only devices revealed the influences of the H_2O vapor (RH 90%), dry O_2, and ambient air (RH 50%) exposure on the electrical properties of LiTFSI-doped spiro-MeOTAD HTLs. H_2O vapor exposure resulted in an irreversible enhancement of LiTFSI-doped HTL conductivity, which was independent of the applied bias. On the other hand, the films exposed to oxygen resulted in a reversible enhancement of the conductivity under applied bias in the devices, which is probably due to oxygen doping and was observed after long O_2 exposure times (39 h). I-V measurements on the air-exposed samples showed about 4 orders of magnitude increase in the conductivity compared to about 2 orders of magnitude in each of the H_2O vapor and O_2 gas exposures. The observed combined effect seems to be the major cause of the increased cell performance when perovskite solar cells are exposed to ambient air for a several hours before testing.

Chapter 7: Interfacial Engineering of the Spiro-MeOTAD/Perovskite Interface[132]

7. 1. Introduction

The work presented in chapters 3-6 was focusing on the basic science behind the outstanding performance of the LiTFSI-doped spiro-MeOTAD HTL in perovskite solar cells and its interaction with the surrounding environmental conditions. In this chapter, a step further will be presented, in which a successful attempt to engineer the interface between the perovskite absorber and the LiTFSI doped spiro-MeOTAD HTL.

To achieve better PCEs in thin film solar cells, it is crucial to minimize the recombination and maximize the carrier extraction efficiency at the interfaces between different layers. One of the necessary steps to achieve this goal is by optimization of the energy-level alignment at the interfaces in devices.[133] Favourable energy-level alignment depends on fine adjustment of the energy levels of the hole and electron selective contacts to match the energy levels of the absorber material and vice versa.

Methyl ammonium lead iodide perovskite is a widely employed semiconductor material for optoelectronic devices and specially for solar cells based on $MAPbI_3$ exhibit high PCEs. $MAPbI_3$

films are often reported with an n-type natures when deposited on n-type or insulating substrates.[134-135] In standard perovskite solar cells structure, (with FTO/TiO_2 as electron selective layer), the CB of the ETL has a favourable alignment with the CB of perovskite absorber.[92, 135-136] On the other hand, an interfacial increase in the leading edge of the perovskite layer VB would provide better hole extraction efficiency and minimized carrier recombination at the interface between the perovskite layer and the LiTFSI-doped spiro-MeOTAD HTL. Thus, a fine control of the $MAPbI_3$ perovskite interface with the HTL is necessary to achieve an optimal energy-level alignment and therefore maximize the charge extraction and power conversion efficiencies.

The CB of $MAPbI_3$ is often reported to be pinned to the E_F in standard-structure PSCs.[92, 135-137] It was shown by ultraviolet photoelectron spectroscopy that the $MAPbI_3$ semiconductor layer is complex and several factors such as the surface stoichiometry, the type of defects present, influence from the underneath substrate, and others may lead to such an observation.[137] Deficient amounts of methylammonium iodide in the precursor solution of the $MAPbI_3$ or short annealing time were reported to lead to an n-type behavior of the $MAPbI_3$ film.[138] UPS and XPS measurements show that energy levels of $MAPbI_3$ layer can be tuned up to 1 eV, depending on the preparation conditions.[139] The doping density of the perovskite film in the inverted structure PSCs with 2-step perovskite film preparation method was reported to be highly dependent on the length of the MAI loading period of time. Short length of methylammonium iodide loading time resulted in low efficiencies, which substantially increased with longer length up to 1 minute. Longer periods of loading resulted in an opposite effect with a dramatic decrease in the PCEs and was attributed to excess of uncoordinated ions.[140] High PCE and reproducibility were achieved using one-step method with a small amount of excess methylammonium iodide in the precursor solution. The higher PCE and reproducibility were attributed to formation of an MAI layer at the grain

boundaries of the perovskite film. The passivation of the grain boundaries with MAI is believed to enhance charge carrier extraction and suppress the non-radiative recombination.[141]

On the other hand, it was proposed that excess MAI might remain on the surface of the perovskite layer and thus reduce the surface conductivity.[142] Interestingly, excess PbI_2 incorporation in the perovskite precursor solution was also reported to improve the PCEs of the perovskite solar cells and was suggested to enhance the crystallinity of the perovskite film.[143] Excess PbI_2 in the perovskite precursor solution was also discussed as a "double-edge sword" leading to higher efficiencies for PbI_2-rich solar cells and higher open circuit voltage for MAI rich solar cells.[144] However, the exact influence of excess MAI or where it should be located in PSCs has remained speculative.

In this work, an ultrathin MAI layer by vacuum evaporation was introduced to simulate and study the effects of various amounts of excess MAI at the interface between the $MAPbI_3$ layer and the LiTFSI-doped spiro-MeOTAD HTL. The photoemission spectroscopy measurements suggest that the additional ultrathin MAI layer deposition leads to better interfacial energy level tuning of the $MAPbI_3$ perovskite films. By examining the energy level evolution systematically at the interface between the perovskite and the HTL as a function of MAI layer thickness, an excess MAI thickness of 8 nm was found to be the optimal interfacial energy level alignment with the doped spiro-MeOTAD HTL. Moreover, we examined the validity of such an optimized condition with solar cells testing. Samples were prepared using standard perovskite solar cells structure consisting of FTO/TiO_2 compact layer/TiO_2 mesoporous layer/$MAPbI_3$. The $MAPbI_3$ layer was prepared using one-step solution processing with an anti-solvent of diethyl ether.[145-146] One sample served as reference, was prepared without any modification of the $MAPbI_3$ layer, while the remaining

samples were prepared with additional ultrathin layers of MAI on the top of the MAPbI$_3$ layer by thermal evaporation under vacuum. Nominal thicknesses of the evaporated MAI were 1 nm, 2 nm, 4 nm, 8 nm, 16 nm, and 32 nm. The nominal thicknesses were measured with a calibrated quartz crystal microbalance inside MAI evaporation chamber. The fabricated solar cells with optimal interfacial modification exhibited an average stabilized PCE of 17.2%, which is 19% higher than that of reference solar cells which had a PCE of 14.5%. The devices stabilized PCE shows smaller spreading with a PCE standard deviation of 0.4% as compared with 1.9% for reference cells, suggesting significantly improved device reproducibility.

7. 2.   Experimental Methods

The electronic properties of interfacially doped MAPbI$_3$ films were characterized by UPS (Kratos AXIS ULTRA HAS, He−Iα = 21.22 eV). The leading edge of the VB was extracted from logarithmic scale of the intensity. The analysis of UPS measurements was complemented by XPS (Kratos AXIS ULTRA HAS, monochromated Al−Kα = 1486.6 eV). XPS was performed to monitor the chemical states of the perovskite films, and the MAI treated films. The BE for UPS and XPS was calibrated by measuring E_F = 0 eV and Au- 4f$_{7/2}$ (84.0 eV) on a clean Au surface. The estimated energy resolutions of UPS and XPS were 0.14 and 0.7 eV, respectively. Pristine perovskite samples were used as reference for fitting the first peaks. For the afterwards MAI treated samples, FWHM of each spectrum was constrained to a change of ±0.1 eV. The peak positions were constrained to a change of ±0.1 eV. When spectral changes were observed, new peaks were added to complete the curve fit. The new fitted peaks were used as reference for the afterwards samples. The peak fittings and STD calculations were performed using CasaXPS 2.3.16 software. The stoichiometry analyses in the C-1s core level region show the largest STD of ~50%. The large STD is due to the fitting of multiple components (4 peaks) that was employed to reproduce the

XPS raw data. The analyses of the atomic ratio for the other elements were estimated to have lower relative errors with respect to the stoichiometry values (30%). UV- and X-ray-induced sample damage was monitored by comparing five consecutive spectra. Time acquisition for each XPS scan varied from 20 to 70 s depending on the element regions. If no changes were observed, the five scans were averaged to a single spectrum. Special care was taken to minimize the UV and X-ray exposure time while acquiring the photoemission on the perovskite films. No X-ray- or UV-induced damage was observed on the perovskite samples.

Perovskite solar cells were prepared by cleaning the FTO conductive substrates (FTO22-7, OPVTech) using brushing with sodium dodecyl sulfate, rinsing with milliQ water and finally sonicating the samples in a 2-propanol bath for 15 min. A ~70 nm layer of compact TiO_2 layer was deposited by spraying a solution of Ti (IV) diisopropoxyde bis(acetylacetonate) (75%) in isopropanol (Aldrich) on a heated FTO substrates at 480°C in four rounds of 3 s each spray. After cooling the substrates to room temperature, a TiO_2 mesoporous layer of about 150 nm was deposited by spin-coating a diluted paste (90-T, Dyesol) in 1-butanol 1:5 wt. at 4500 rpm for 30 s. The spin-coated layer was dried at hotplate (100°C) and the edge removed using cotton swabs. Finally, the samples were annealed at 480°C for 30 min with a slow heating ramp.

The $MAPbI_3$ precursor was made by mixing 0.461 g of PbI_2 (99.99%, TCI) and 0.159 g of methylammonium iodide (Dyesol) in 73 μL anhydrous dimethylsulfoxide (DMSO, Aldrich) and 570 μL of anhydrous *N, N* - dimethylformamide (DMF, Aldrich). The precursor solution was spin-coated on the substrates after UV-O_3-treatment of the TiO_2 mesoporous layer at 1200 rpm for 1 s followed by 2800 rpm 25 s. A 300 μL of DEE was dripped at 14 s during the second spinning to

form a transparent adduct. The substrates were transferred into a nitrogen-filled glove box with low RH (< 5%) and annealed at 60°C for 10 min and then 100°C for 20 min.

The modification of the perovskite films was achieved using thermal evaporation of the MAI powder (Dyesol) in a vacuum chamber (1×10^{-2} Pa). It is noteworthy to mention that a precise calibration of evaporated MAI film is difficult to be obtained due to Volmer-Weber (island) growth characteristics onto flat substrates such as glass or silicon.[147-148] The QCM was calibrated by evaporating different thickness of MAI powder onto Si substrates and then measuring the final thicknesses by profilometer.[148] Reported thicknesses of MAI evaporation in this work are based on these nominal values as measured by the QCM.

The LiTFSI-doped spiro-MeOTAD precursor was prepared by mixing 70 mM of spiro-MeOTAD (Merck), 231 mM t-BP, 35 mM of bis(trifluoromethane) sulfonimide lithium salt (pre-dissolved in acetonitrile) and 2.1 mM of tris(2-(1H-pyrazol-1-yl)-4-tert-butylpyridine)cobalt(III) tri[bis(trifluoromethane)sulfonimide] in chlorobenzene (all from Aldrich). The LiTFSI-doped spiro-MeOTAD HTL solution was deposited on the $MAPbI_3$ layer by dripping 30 µL of the solution during spinning at 3000 rpm. Finally, 70 nm of gold was deposited as the top electrode by thermal evaporation.

7. 3.   Electronic Changes (UPS)

Analysis of UPS data for the pristine perovskite film provide a VB leading edge position of 1.45 eV w.r.t. E_F (Fig. 7.1, 7.2), which corresponds to IE of 5.36 eV (Fig. 7.3). The addition of small amounts of MAI on top of the $MAPbI_3$ layer resulted in a gradual up-shift of the perovskite VB from -1.45 eV to -1.15 eV, which resembles p-doping behaviour.[138] The distance between E_F

and VB was decreased by 0.3 eV (pristine vs. 16 nm). On the other hand, no drastic changes in the WFs were observed as a function of MAI layer thickness, (Fig. 7.2b). As shown in Fig. 7.3, gradual and systematic decrease in the IE is noticed as the additional MAI layer is thickness increased.[139, 149] The change in the IE is related to the chemical composition changes on the $MAPbI_3$ surfaces, which is discussed later when discussing the XPS results. For example, the IE of the $MAPbI_3$ layer with an additional 16 nm MAI layer was 4.93 eV, as compared to 5.36 eV in case of pristine the films (Fig. 7.3). Thus, the energy shift in the VB and IE (Fig. 7.2a, 7.3) is different (0.3 eV vs. 0.43 eV), which suggests that this is not a doping effect in a strict sense. A doping effect would be expected to induce a rigid shift of the whole UPS spectrum toward E_F (Fig. 7.2a). The observed energy shift suggests a non-stoichiometric nature of the deposited MAI on top of the $MAPbI_3$ layer. The predicted non-stoichiometric nature here suggests that the MAI molecules break, more details will be discussed based on the XPS results in the next section. An opposite effect was observed with additional evaporation of MAI with nominal values greater than 16 nm. For instance, the evaporation of 32 nm of MAI resulted in about 0.4 eV shift away from E_F to -1.61 eV with a corresponding IE of 5.34 eV. The schematic energy level diagrams with respect to E_V extracted from the UPS results can be seen in Fig. 7.3.
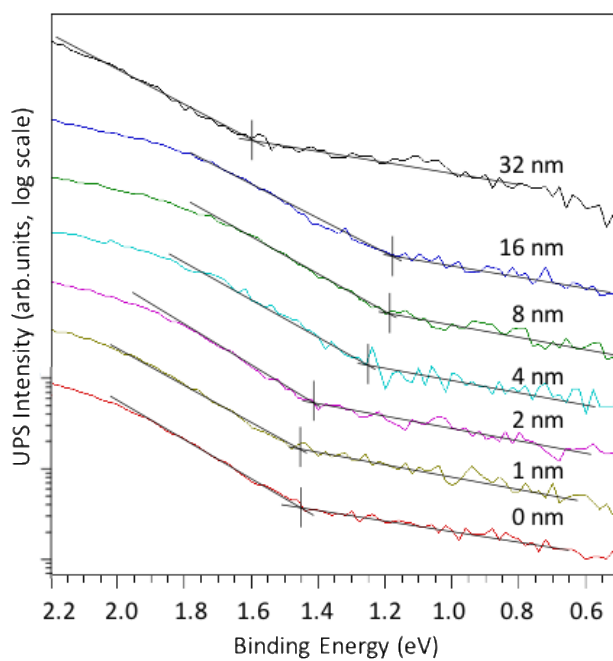
Figure 7.1 UPS spectra (He-Iα = 21.22 eV) shown in Figure 1 plotted in semi-log scale. The valence band of the pristine perovskite (0 nm) and the samples with additional layer of excess MAI of various thicknesses (1 to 32 nm) are shown.
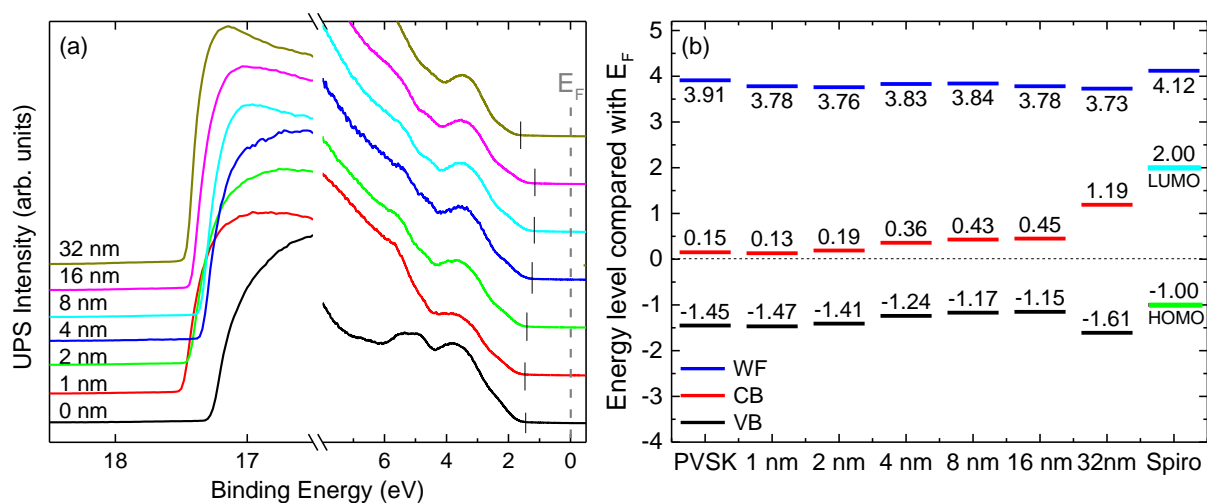
Figure 7.2 (a) UPS spectra (He−Iα = 21.22 eV) corresponding to valance band (VB) and cut-off regions of the pristine perovskite (PVSK) sample and the samples with an additional layer of excess MAI of various thicknesses. (b) A schematic energy diagram of VB, conduction band (CB), and work function (WF) with respect to Fermi energy (E_F) corresponding to the pristine perovskite sample, afterwards modification by MAI evaporation, and spiro-MeOTAD (spiro). CB values are derived based on the optical band gap of MAPI perovskite and VB, and in the case of a 32-nm MAI layer, the MAI band gap is used.
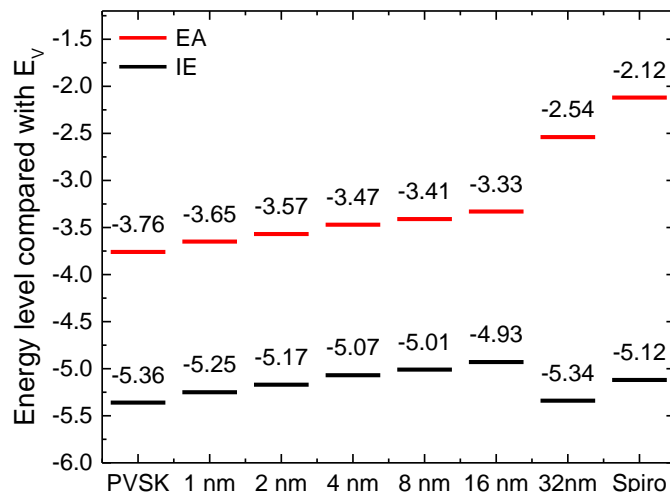
Figure 7.3 UPS schematic energy diagram with respect to vacuum level (E_V) corresponding to the pristine perovskite sample, modified by MAI deposition, and spiro-MeOTAD (spiro). Electron affinity (EA) values provided are based on adding the band gap of $MAPbI_3$ perovskite to its ionization energy. At 32-nm the MAI band gap is added.

7. 4.   Chemical Changes (XPS)

XPS (Al−Kα = 1486.6 eV) was carried out on the perovskite samples to monitor the chemical states evolution. As can be seen in Fig. 7.4 XPS core levels of Pb-4f (a), I-3d (b), and C-1s (c) of the $MAPbI_3$ perovskite films with different MAI thicknesses were monitored. Interestingly, no detectable shifts in the binding energies in the region of Pb-4f (Fig. 7.4a) was observed. The peak maximum of Pb-$4f_{7/2}$ for the pristine $MAPbI_3$ film was found to be at a BE of 138.58 eV and showed no shift in BE, even after evaporation of a 32nm nominal thickness of MAI (~0.01 eV). The Pb-4f core level signal is still detected with a 32nm of MAI, which indicates an interfacial modification rather than formation of a thick conformal layer of MAI on top of the $MAPbI_3$ film. Moreover, a sample with 120 nm of MAI evaporation on the perovskite film was prepared to examine the possibility of conformal layer formation with excessive amount of MAI (Fig. 7.4). However, Pb-4f signal was still detected. Thus, the interaction between the evaporated MAI and

the MAPbI$_3$ layer needs be considered instead of a considering a simple physical deposition of an inert MAI layer on the MAPbI$_3$ layer. Possible scenarios include penetration of MAI and/or dissociated species of MAI into the perovskite film or the dissociated species from MAI are volatile species and may leave the perovskite surface leading to a detectable level of Pb-4f core level signal by XPS. Here the focus is on the Pb-4f core level because Pb is the only element that can be correlated directly with the underlying layer of the MAPbI$_3$ perovskite layer (all other elements are also present in the MAI molecule). XPS has a deeper probing depth compared to UPS because of a longer mean escape depth for the photoelectrons with higher kinetic energies.[150] In addition, almost no shift in the BEs of Pb-4f were observed. Thus, it is clear that the observed shift in the leading edge of the VB is taking place at the interface with no more than 2nm depth, which is the expected mean escape depth for UPS.
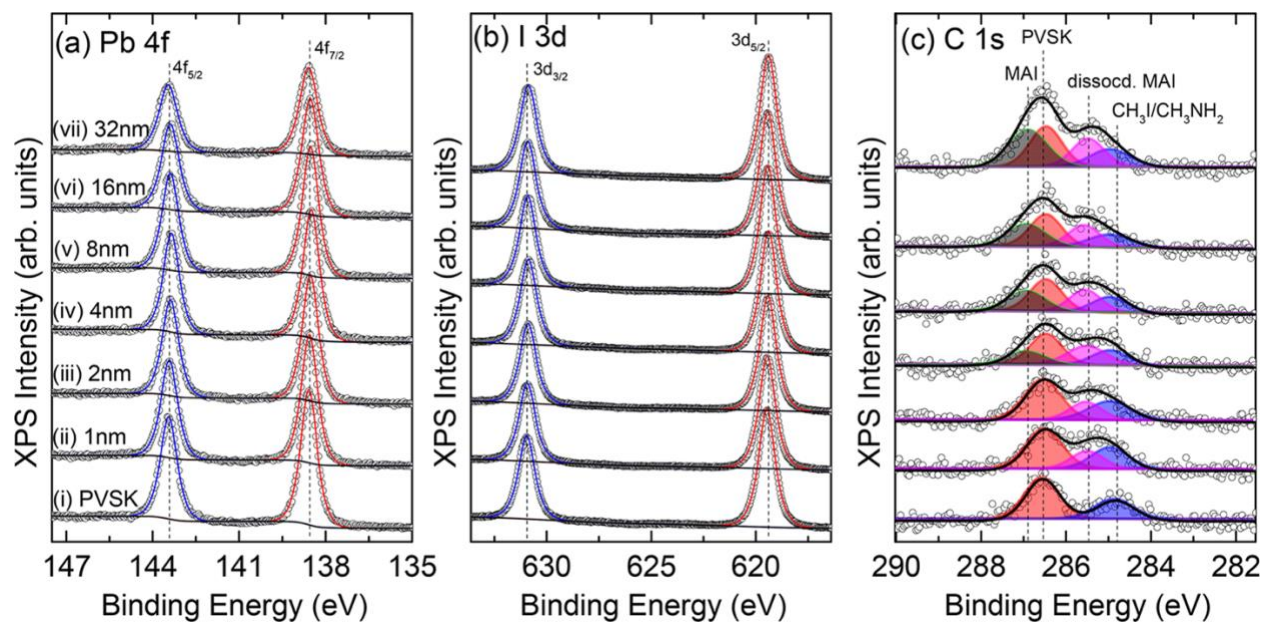
Figure 7.4 XPS spectra (Al−Kα = 1486.6 eV) corresponding to (a) Pb-4f, (b) I-3d, and (c) C-1s core levels of the pristine perovskite (PVSK) film (i) and the samples after depositing an additional excess MAI layer of 1 nm (ii), 2 nm (iii), 4 nm (iv), 8 nm (v), 16 nm (vi), and 32 nm (vii).

Similarly, no shifts were observed in the BEs of the core levels of I-3d (Fig. 7.4b). The I-3d$_{5/2}$ peak maximum for the pristine perovskite sample was found to be at a BE of 619.47 eV and the maximum observed change was 0.07 eV, which is within the measurements uncertainty. Similarly, the core level of N-1s spectra did not show any shift in the BEs of the peak maximum (Fig. 7.5a). O-1s core level was also monitored for all samples and the detected amount was less than 1% (Fig. 7.5b).
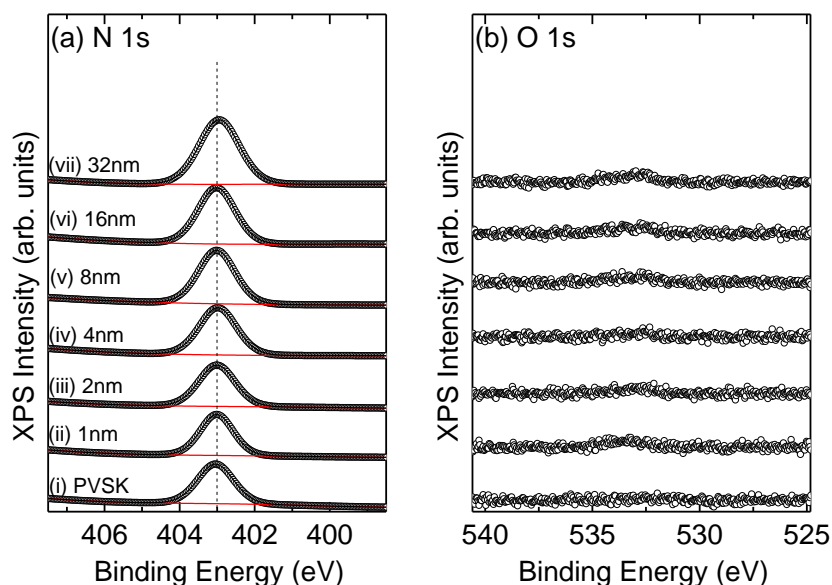
Figure 7.5 XPS spectra (Al−Kα = 1486.6 eV) corresponding to (a) N-1s, and (b) O-1s core levels of pristine perovskite film (i) and subsequent MAI deposition of 1 nm (ii), 2 nm (iii), 4 nm (iv), 8 nm (v), 16 nm (vi), and 32 nm (vii).

In C-1s core level spectrum (Fig. 7.4c), non-modified MAPbI$_3$ films showed two main peaks, one with maxima located at BEs of 286.54 eV and the other was located at 284.83 eV. The C-1s peak at a higher BE of 286.54 eV was reported to be associated with carbon in crystalline

perovskite films. Currently, the origin of the C-1s peak at a lower BE of 284.83 eV remains controversial, and it has been suggested that this peak could originate from carbon in CH_3I,[151] CH_3NH_2,[152] and/or remaining solvents.[135, 149, 153-154] After deposition of 1-nm of MAI layer on the perovskite layer, a new peak between the aforementioned two peaks at a BE of 285.46 eV was observed. At the current stage, this peak is tentatively assigned to dissociated MAI species (dissocd. MAI). As more MAI is deposited on the perovskite layer, another new peak appeared in the C-1s core level region with a peak maximum at 286.86 eV, the intensity of which gradually increased as MAI thickness increased. Simultaneously, a behavior of MAI electronic properties was noticed with UPS, that could be because of progressive formation of a pure MAI layer on top of the $MAPbI_3$ film. An alternative explanation will be discussed based on the changes in the atomic ratios below.

In addition, XPS measurements were performed on the 120 nm of MAI evaporated on $MAPbI_3$ layer, pristine $MAPbI_3$, SiO_2 (native oxide)/Si(100), and chlorobenzene spin-coated on $MAI/MAPbI_3$ films for comparison purposes (Fig. 7.6). As can be seen in Fig. 7.6a, the Pb-4f signal in the 120-nm is still observed, however it was significantly attenuated when compared to $MAI/MAPbI_3$ sample, which confirms the observation with the 32-nm that no conformal layer is formed. These results indicate that the interaction chemistry between MAI and the perovskite needs be considered, and it is NOT a simple physical deposition of an inert MAI layer on perovskite film. For instance, MAI and/or dissociated species may penetrate into the perovskite film or the dissociated species from MAI are volatile species and may leave the perovskite surface leading to a detectable level of Pb-4f core level signal by XPS. This effect will be more enhanced when the sample is under UHV conditions for photoemission spectroscopy measurements. In addition, a shift of about 0.3 eV was noticed in the peak maximum of all the elements related to

the perovskite film when a thick layer of 120 nm of MAI was deposited on the perovskite film.

This shift indicates an additional shift of the leading edge of the VB features away from E_F.
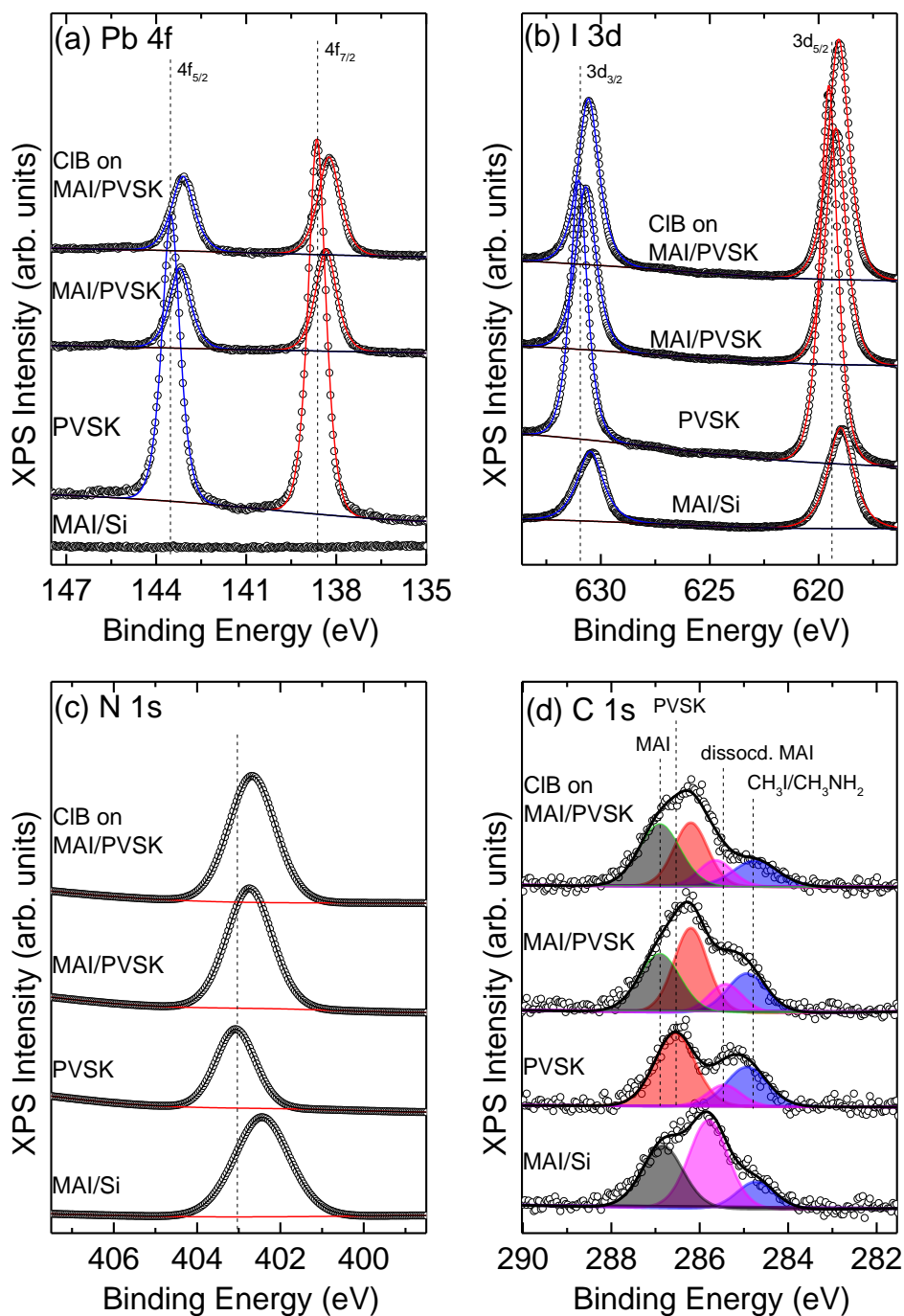
Figure 7.6 XPS spectra (Al-Kα = 1486.8 eV) corresponding to (a) Pb-4f, (b) I-3d, (c) N-1s, and (d) C-1s of MAI on SiO₂(native oxide)/Si(100); MAI on MAPbI₃ perovskite (PVSK); chlorobenzene spin coated on MAI/MAPbI₃; pristine MAPbI₃ as reference.

As shown in Fig 7.6, a mixture similar to hole transport material solvent composition (chlorobenzene+ acetonitrile) was spin-coated on top of the as-deposited MAI layer on MAPbI$_3$ to examine the effect of the HTL solution deposition on top of the modified layer. However, no remarkable decrease in thickness or composition change was observed. It was also observed that after spin-coating of this mixture (chlorobenzene+ acetonitrile), the C-1s at low BE and the perovskite signals decrease slightly, which could be due to a "cleaning" of oxidized or hydrated MAI species on the top surface. Some of the low BE in C 1s region can be also originated from contamination.

7. 5. XPS Atomic Concentration Variations

The atomic concentration variations of all the measured elements (Fig. 7.7a, b) showed that pristine MAPbI$_3$ films have Pb: I: C(MAPbI$_3$): N ratio of 1.0: 2.9: 1.1: 1.1. This ratio is in good agreement with MAPbI$_3$ perovskite, which shows ideal ratios of 1: 3: 1: 1. However, the best performing solar cells (with 4 nm excess MAI) showed non-stoichiometric ratios of 1.0: 3.0: 1.6: 1.1 (Pb: I: C(MAPbI$_3$): N), which indicates that the MAI modification is *not* an extra conversion step of the non-converted PbI$_2$ on the surface to perovskite. Thus, the excessive carbon observed here is from dissociated MAI species from the evaporated MAI. The N-1s core level signal did not increase, possibly due to possible release of ammonia gas[155] or other nitrogen containing released gas species. Atomic ratio variations of I-3d, C-1s, N-1s, and all different types of carbon species in C-1s region for all samples can be seen in Fig. 7.7. After deposition of 32nm of MAI, the atomic ratio concentration of nitrogen and iodine increased substantially while the concentration of the carbon from MAPbI$_3$ in the total C-1s concentration decreased (Fig. 7.7).
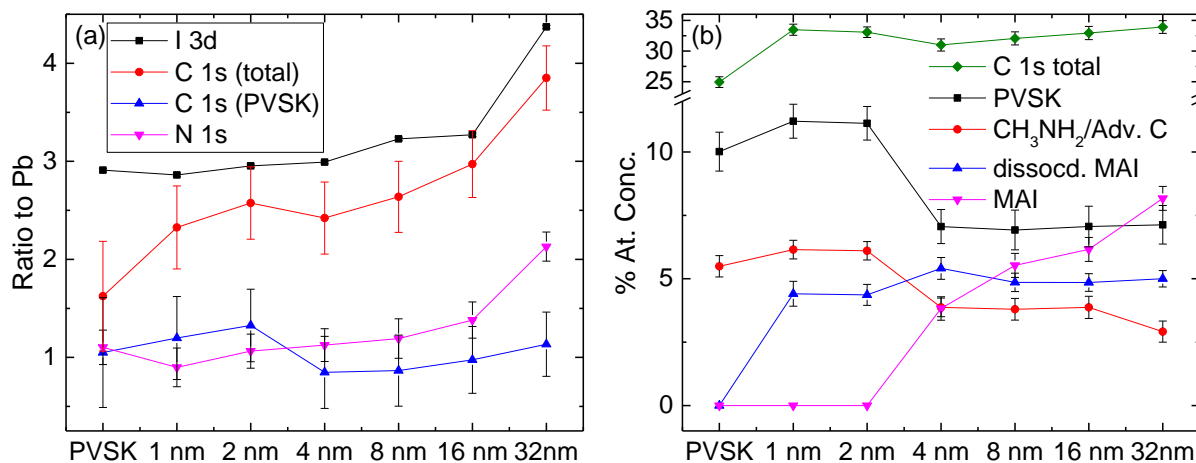
Figure 7.7 XPS surface atomic concentration (a) ratio for I-3d, C-1s from perovskite (PVSK), and N-1s with respect to Pb-4f signal, and (b) C-1s different species versus nominal MAI evaporation thicknesses.

7. 6.   perovskite solar cells

The photoemission spectroscopy measurements provided an explicit evidence that the addition of ultrathin MAI layer efficiently tunes energy level of the $MAPbI_3$ layer at the interface with the HTL. As can be seen from Fig.7.2b, a favorable energy level alignment between $MAPbI_3$ and the spiro-MeOTAD HTL would be achieved if an ultrathin layer of MAI is implemented at the interface. This ultrathin MAI layer would clearly enhance hole extraction efficiency due to staircase energy level alignment, which is achieved with the interfacial modification of the $MAPbI_3$ layer.[156-157] Also, a reduction in the recombination at this interface is expected due to decreased number of electrons as a result of slight band bending at the top of $MAPbI_3$/MAI layer.

In addition, as discussed in the XPS results (Fig. 7.4c) the MAPbI$_3$ that was modified with 4 nm of MAI showed formation of small amount of intact MAI. The presence of intact MAI would also enhance the PCE by passivating the grain boundaries as discussed by Son et al.[141] Although the excess of MAI in the precursor solution in the work by Son et al.[141] is not completely equivalent to the case of evaporating a thin interface layer of MAI between perovskite and HTL as in this study, a consistent trend is once again drawn.

Thus, following the findings presented here, solar cells with MAI modification were fabricated. The fabricated perovskite solar cells used the same structure as was used for photoemission spectroscopy experiments. The only difference was that for devices, a doped spiro-MeOTAD layer was deposited by spin-coating and Au electrode by vacuum evaporation on top of pristine or MAI-modified perovskites. After Au evaporation, devices were left overnight in relatively low humidity environment to achieve better electrical properties and a HOMO level of 1 eV below E_F for spiro-MeOTAD HTL (Fig. 7.2b), which provides better energy level alignment with the modified perovskite layer.[66, 100]

Impressive enhancement in the stabilized PCE was obtained for the solar cells with additional 2 nm and 4 nm deposition of MAI, which is in good agreement with the enhanced energy level alignment at the interface between MAI-modified MAPbI$_3$ and the doped spiro-MeOTAD HTL. Reference solar cells showed an average steady-state PCE of 14.5%. In comparison, the solar cells with an additional 4 nm MAI layer showed a significantly enhanced stabilized PCE up to 17.2% (Fig. 7.8a). In addition, solar cells with an additional 4 nm MAI deposition showed much lower STD in PCE, which indicates better batch-to-batch reproducibility (Fig. 7.8b). Solar Cells with an additional 4 nm MAI deposition showed STD of 0.4% compared to the reference cells with STD of 1.9%. The enhancement in the perovskite solar cell device PCE and reproducibility

highlights the importance of interfacial modification in PSCs performance. The low value of STD suggests better reproducibility, which is consistent with previous reports that showed enhanced reproducibility with excess amounts of MAI in the perovskite precursor solution.[141] The improved reproducibility is possibly a benefit of the better-defined perovskite/HTL interface for the solar cells with excess interfacial MAI, as compared with the reference solar cells, in which interface properties may sensitively depend on the conditions of the perovskite film preparation.
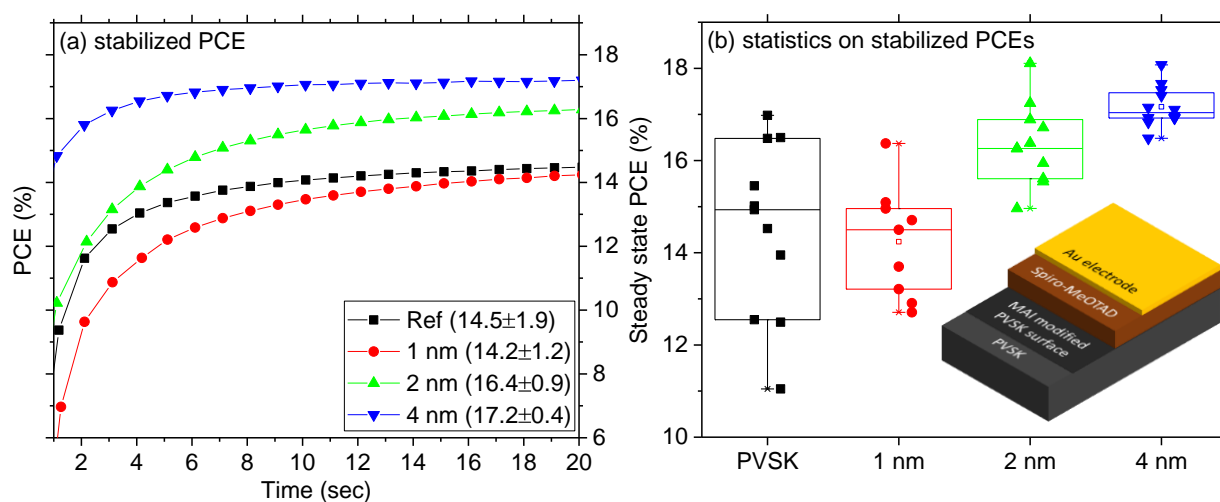
Figure 7.8 (a) average steady-state PCE from all measured devices, and (b) statistics on steady-state PCE for perovskite (PVSK) solar cells as a function of excess MAI layer thickness. The inset shows a schematic of the interface modification.

In the J-V scans (Fig. 7.9), improved PCEs were observed after the addition of MAI layer. The maximum PCE obtained was 18.3%, which was obtained with 2 nm of MAI excess on top of the perovskite layer. The maximum PCE for 1 nm of MAI obtained was 18.0%, and 17.6% was the limit for both the reference and 4 nm MAI excess samples (Fig. 7.9a). However, average J-V scans for all samples and corresponding STD (Fig. 7.9b) showed that the 2-nm MAI cells have the

highest average efficiencies of 17.4% with STD of 0.4%. Photovoltaic parameters extracted from the transient J-V scans (Fig. 7.10) showed that the main improvement in the PCE (Fig. 7.10a) was due to a better fill factor (Fig. 7.10c) for all MAI-treated cells. It is noteworthy that the STD values extracted from J-V scans did not exhibit a similar trend of lower STD values for samples modified with MAI excess, but all values were comparable.

J-V curves were measured the next day of the solar cells fabrication to allow enough time for doping and re-distribution of LiTFSI dopants across the spiro-MeOTAD HTL film (Fig. 7.9, 7.10). J-V and steady-state measurements were performed under 1 sun illumination (AM 1.5 G, 100 mW·cm^{-2}, calibrated using a Newport reference Si-cell) using a solar simulator (Newport Oriel Sol 1A) and a Keithley 2400 source meter in ambient air conditions at a relative humidity of ~40–50% and using a 0.1 cm^2 shadow mask. The measurements were performed from -0.1V to 1.2V in 40-point steps with a delay time of 10 ms.
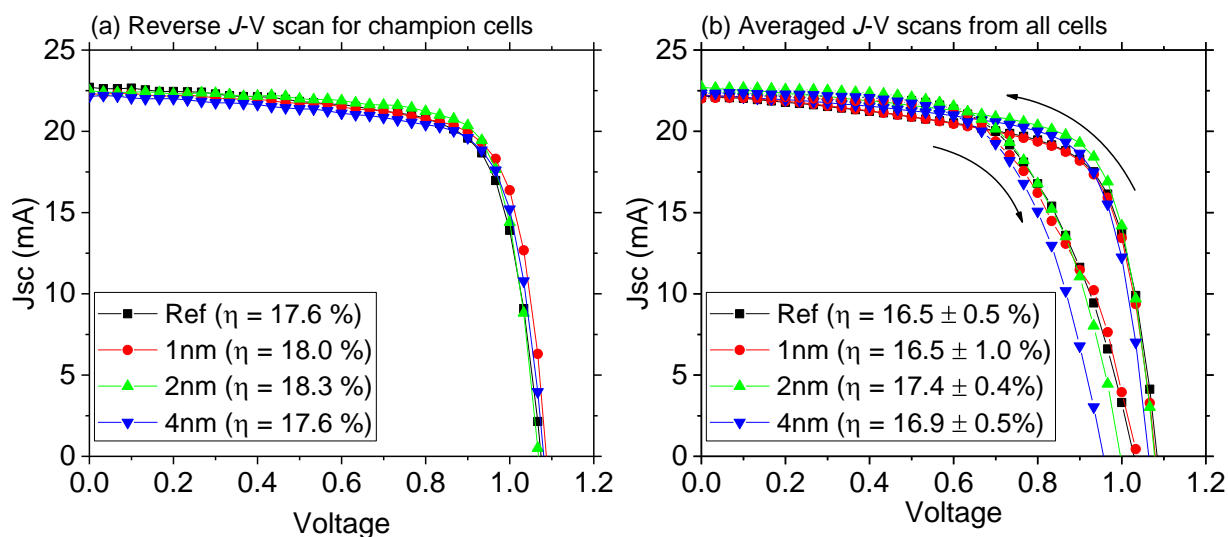
Figure 7.9 (a) Reverse transient J-V scans for champion cells, and (b) averaged J-V scans for all devices with different added MAI thicknesses.
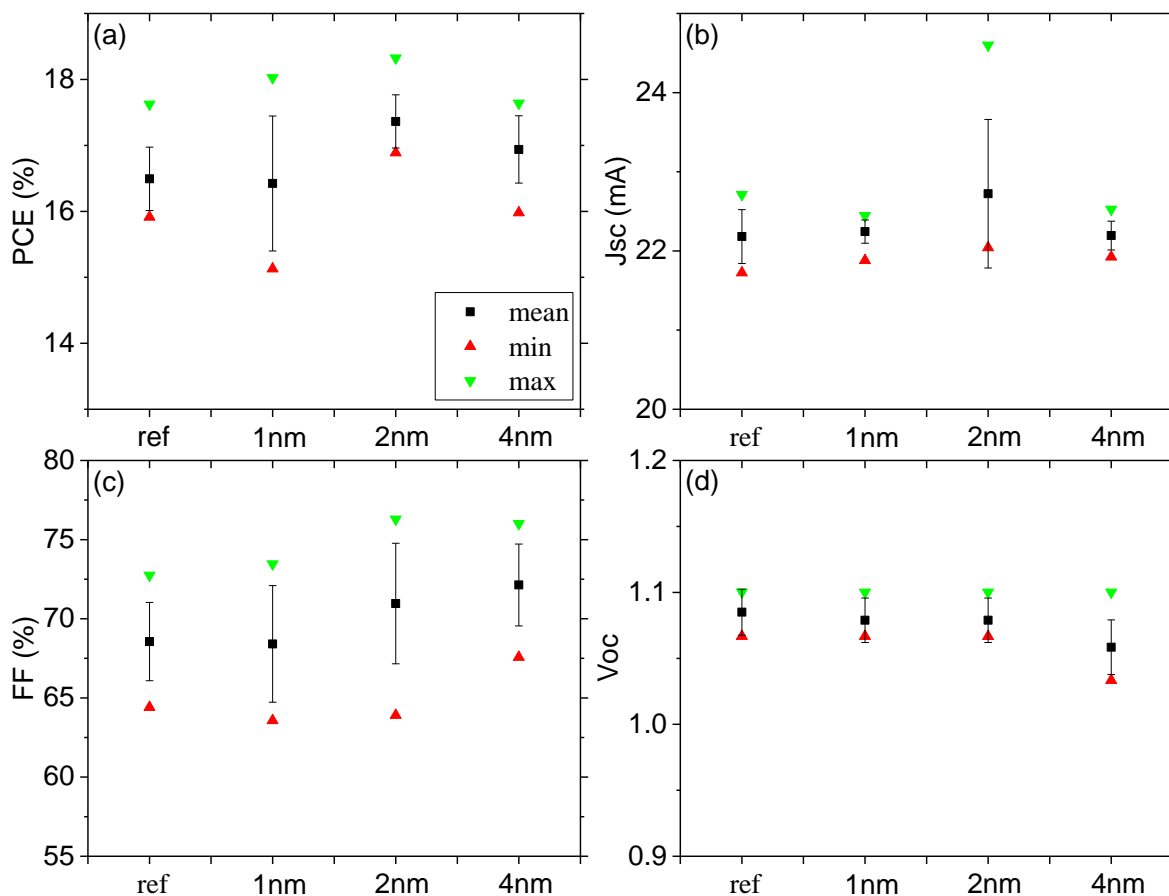
Figure 7.10 Statistics for photovoltaic parameters from transient *J*-V scans with interfacial excess MAI treatment (a) PCE, (b) Jsc, (c) FF, and Voc.

7. 7.   Summary

In summary, the effect of excess MAI at the interface between MAPbI₃ perovskite and LiTFSI-doped spiro-MeOTAD HTL in standard structure perovskite cells was examined. The situation is simulated by vacuum depositing a layer of excess MAI on top of MAPbI₃ perovskite layer. Photoemission spectroscopy results revealed an efficient interfacial energy-level tuning of the perovskite layer, as a function of excess MAI layer thickness. By examining the energy level at the interface systematically as the MAI layer thickness increased, the optimal interfacial

energetic and the corresponding interfacial MAI layer thickness was identified. The XPS results revealed that the initial thin layer of MAI dissociates when it is in contact with the $MAPbI_3$ layer. It is not the MAI layer, but the MAI dissociated species that leads to the interfacial energy-level tuning. The validity of such an optimal condition was verified with perovskite solar cell devices testing. The perovskite solar cells showed an impressive improvement in reproducibility and stabilized PCEs of 17.2±0.4% (4nm nominal thickness of MAI) as compared to 14.5±1.9% in the case of reference non-modified cells. The findings presented here, not only provide vital insight into the role of excess MAI in perovskite solar cells, but it also indicates the importance of interfacial modification on both the performance and the reproducibility of the perovskite solar cells.

Conclusion

This dissertation discusses surface science aspects of perovskite solar cells including surface chemistry, electronic properties, and morphological defects. These aspects were investigated using x-ray photoelectron spectroscopy, ultraviolet photoelectron spectroscopy, atomic force microscopy, and scanning electron microscopy. The findings from the surface science investigations were further examined for bulk electrical properties using hole-only devices as well as to achieve enhanced power conversion efficiency using solar cell devices.

As discussed in chapter 3, it was revealed using AFM that LiTFSI-doped spiro-MeOTAD HTL has high density of pinholes of ~3.7 holes/μm^2 with an average diameter of ~135 nm. In addition, large size pinholes with diameters in the range of 1-20 μm and a density of ~289 holes/mm^2 were also revealed using optical microscopy. Using cross sectional SEM, these pinholes were found to wiggle through the entire HTL film. The small-sized pinholes were partially filled up upon ambient air exposure.

As described in chapter 4, XPS measurements revealed that freshly prepared LiTFSI-doped spiro-MeOTAD HTL has very low concentration of LiTFSI dopants on the top surface of the HTL film and upon ambient air exposure, LiTFSI concentration increases substantially. This migration of LiTFSI dopants across the bulk film is believed to be facilitated by the two types of pinholes that was discovered. The presence of these pinholes may strongly affect the stability of the

perovskite based solar cells using spin coated spiro-MeOTAD as HTL. Therefore, it is necessary to optimize the preparation method for spin coated doped spiro-MeOTAD. It was also found using UPS that ambient air exposure results in better energy level alignment in the perovskite solar cells which is due to p-doping behavior of the doped spiro-MeOTAD HTM.

Next, in chapter 5, the constituent component in ambient air that drives the migration of the LiTFSI dopants was investigated using controlled environments of H_2O vapor with a relative humidity of 90% that is generated by letting a stream of dry N_2 gas flow through a H_2O bubbler, high purity dry O_2 gas (>99.5%), and control environments of N_2 gas and vacuum. It was found using XPS that H_2O vapor is the main component that drives the migration of LiTFSI dopants.

Afterwards, as was revealed in chapter 6, the same environmental conditions of ambient air, H_2O vapor, high purity O_2, and N_2 exposures were implemented to investigate the electrical properties of hole-only devices of LiTFSI-doped spiro-MeOTAD films, using mercury drop I-V measurements. It was found that H_2O vapor exposure results in an irreversible enhancement of LiTFSI-doped HTL conductivity, which indicates that LiTFSI dopants are re-distributed across the spiro-MeOTAD HTL film rather than segregated to the top surface of the film. On the other hand, it was found that O_2 exposure results in a reversible enhancement of the electrical properties under applied bias in the tested devices. This enhancement is expected to be due to O_2 doping and was observed after long O_2 exposure times (39 h). I-V measurements on ambient air-exposed samples showed more than 4 orders of magnitude increase in the conductivity of the devices compared to about an increase of 2 orders of magnitude in case of the H_2O vapor or O_2 exposure. Such an effect is expected to be the major cause of the increased cell performance when perovskite solar cells are exposed to ambient air for a period of time (typically several hours) before testing.

Finally, in chapter 7, interfacial modification of the interface between the doped spiro-MeOTAD and the perovskite absorber was investigated and implemented to achieve better efficiency and reproducibility. This approach was based on intentionally deposition of an ultrathin layer of excess methyl ammonium iodide (MAI) using thermal evaporation on top of a methyl ammonium lead iodide MAPbI$_3$ perovskite film. Using photoemission spectroscopy, it was found that the deposited ultrathin MAI layer resulted in interfacial and favorable, energy-level tuning of the perovskite absorber layer. XPS results revealed that MAI dissociates at low nominal thicknesses (< 16 nm) of evaporation on top the perovskite layer. The dissociated species leads to the interfacial energy-level tuning. The achieved favorable energy level tuning was tested in perovskite solar cells and resulted in substantially enhanced efficiency with an increase of 19% in the average stabilized power conversion efficiency PCE and enhanced reproducibility represented with less standered deviation (from $15 \pm 2\%$ to $17.2 \pm 0.4\%$).

References

1. O'Connor, J.; Sexton, B.; Smart, R. S. C., *Surface Analysis Methods in Materials Science*. Springer Berlin Heidelberg: 2013.

2. Einstein, A., Concerning an Heuristic Point of View Toward the Emission and Transformation of Light. *Am. J. Phys.* **1965,** *33* (5), 367.

3. Siegbahn, K., Electron Spectroscopy for Chemical Analysis (Esca). *Philosophical Transactions of the Royal Society of London Series a-Mathematical and Physical Sciences* **1970,** *268* (1184), 33-&.

4. Seah, M. P.; Dench, W. A., Quantitative electron spectroscopy of surfaces: A standard data base for electron inelastic mean free paths in solids. *Surf. Interface Anal.* **1979,** *1* (1), 2-11.

5. Binnig, G.; Quate, C. F.; Gerber, C., Atomic force microscope. *Phys. Rev. Lett.* **1986,** *56* (9), 930-933.

6. Binnig, G.; Rohrer, H., Scanning Tunneling Microscopy. *Surf. Sci.* **1983,** *126* (1-3), 236-244.

7. Hawash, Z.; Ono, L. K.; Qi, Y. B., Recent Advances in Spiro-MeOTAD Hole Transport Material and its Applications in Organic-Inorganic Halide Perovskite Solar Cells. *Adv. Mater. Interfaces* **2017**, 1700623.

8. Kim, H. S.; Lee, C. R.; Im, J. H.; Lee, K. B.; Moehl, T.; Marchioro, A.; Moon, S. J.; Humphry-Baker, R.; Yum, J. H.; Moser, J. E.; Gratzel, M.; Park, N. G., Lead iodide

perovskite sensitized all-solid-state submicron thin film mesoscopic solar cell with efficiency exceeding 9%. *Sci. rep.* **2012,** *2*, 591.

9.   Lee, M. M.; Teuscher, J.; Miyasaka, T.; Murakami, T. N.; Snaith, H. J., Efficient hybrid solar cells based on meso-superstructured organometal halide perovskites. *Science* **2012,** *338* (6107), 643-7.

10.   National Renewable Energy Laboratory (NREL). Research Cell Efficiency Record. http://www.nrel.gov/ncpv/images/efficiency_chart.jpg. (accessed May 9th, 2017).

11.   Green, M. A.; Emery, K.; Hishikawa, Y.; Warta, W.; Dunlop, E. D., Solar cell efficiency tables (version 48). *Prog. Photovolt: Res. Appl.* **2016,** *24* (7), 905-913.

12.   He, X.; Zervos, H. Perovskite Photovoltaics 2016-2026: Technologies, Markets, Players. http://www.idtechex.com/research/reports/perovskite-photovoltaics-2016-2026-technologies-markets-players-000493.asp (accessed January, 2017).

13.   Hoye, R. L. Z.; Brandt, R. E.; Osherov, A.; Stevanovic, V.; Stranks, S. D.; Wilson, M. W. B.; Kim, H.; Akey, A. J.; Perkins, J. D.; Kurchin, R. C.; Poindexter, J. R.; Wang, E. N.; Bawendi, M. G.; Bulovic, V.; Buonassisi, T., Methylammonium Bismuth Iodide as a Lead-Free, Stable Hybrid Organic-Inorganic Solar Absorber. *Chem. Eur. J.* **2016,** *22* (8), 2605-2610.

14.   Yuan, M.; Li Na, Q.; Comin, R.; Walters, G.; Sabatini, R.; Voznyy, O.; Hoogland, S.; Zhao, Y.; Beauregard, E. M.; Kanjanaboos, P.; Lu, Z.; Kim, D. H.; Sargent, E. H., Perovskite energy funnels for efficient light-emitting diodes. *Nat. Nanotechnol.* **2016,** *11* (10), 872.

15.   Lee, J. W.; Choi, Y. J.; Yang, J. M.; Ham, S.; Jeon, S. K.; Lee, J. Y.; Song, Y. H.; Ji, E. K.; Yoon, D. H.; Seo, S.; Shin, H.; Han, G. S.; Jung, H. S.; Kim, D.; Park, N. G., In-Situ

Formed Type I Nanocrystalline Perovskite Film for Highly Efficient Light-Emitting Diode. *ACS Nano* **2017,** *11* (3), 3311-3319.

16.   Chen, S.; Roh, K.; Lee, J.; Chong, W. K.; Lu, Y.; Mathews, N.; Sum, T. C.; Nurmikko, A., A Photonic Crystal Laser from Solution Based Organo-Lead Iodide Perovskite Thin Films. *ACS Nano* **2016,** *10* (4), 3959-3967.

17.   Zhu, H.; Fu, Y.; Meng, F.; Wu, X.; Gong, Z.; Ding, Q.; Gustafsson, M. V.; Trinh, M. T.; Jin, S.; Zhu, X., Lead halide perovskite nanowire lasers with low lasing thresholds and high quality factors. *Nat. Mater.* **2015,** *14* (6), 636-642.

18.   Xu, J.; Chen, Y.; Dai, L., Efficiently photo-charging lithium-ion battery by perovskite solar cell. *Nat. Commun.* **2015,** *6*, 8103.

19.   Luo, J.; Im, J.-H.; Mayer, M. T.; Schreier, M.; Nazeeruddin, M. K.; Park, N.-G.; Tilley, S. D.; Fan, H. J.; Graetzel, M., Water photolysis at 12.3% efficiency via perovskite photovoltaics and Earth-abundant catalysts. *Science* **2014,** *345* (6204), 1593-1596.

20.   Zhang, K.; Ma, M.; Li, P.; Wang, D. H.; Park, J. H., Water Splitting Progress in Tandem Devices: Moving Photolysis beyond Electrolysis. *Adv. Energy Mater.* **2016,** *6* (15), 1600602.

21.   Dou, L.; Yang, Y.; You, J.; Hong, Z.; Chang, W.-H.; Li, G.; Yang, Y., Solution-processed hybrid perovskite photodetectors with high detectivity. *Nat. Commun.* **2014,** *5*, 5404.

22.   Xiao, Z.; Yuan, Y.; Shao, Y.; Wang, Q.; Dong, Q.; Bi, C.; Sharma, P.; Gruverman, A.; Huang, J., Giant switchable photovoltaic effect in organometal trihalide perovskite devices. *Nat. Mater.* **2015,** *14* (2), 193-198.

23.   Wells, H. L., Über die Cäsium- und Kalium-Bleihalogenide. *Z. anorg. allg. Chem.* **1893,** *3* (1), 195-210.

24. Moller, C. K., Crystal Structure and Photoconductivity of Caesium Plumbohalides. *Nature* **1958,** *182* (4647), 1436-1436.

25. Weber, D., CH3NH3PbX3, ein Pb (II)-system mit Kubischer Perowskitstruktur/CH3NH3PbX3, a Pb (II)-system with Cubic Perovskite Structure. *Z. Naturforsch. B* **1978,** *33* (12), 1443-1445.

26. Mitzi, D. B.; Wang, S.; Feild, C. A.; Chess, C. A.; Guloy, A. M., Conducting Layered Organic-inorganic Halides Containing <110>-Oriented Perovskite Sheets. *Science* **1995,** *267* (5203), 1473-6.

27. Papavassiliou, G. C.; Mousdis, G. A.; Koutselas, I. B., Some new organic-inorganic hybrid semiconductors based on metal halide units: Structural, optical and related properties. *Adv. Mater. Opt. Electron.* **1999,** *9* (6), 265-271.

28. Kojima, A.; T., k.; Miyasaka, T.; Shirai, Y., Novel Photoelectrochemical Cell with Mesoscopic Electrodes Sensitized by Lead-Halide Compounds (2). *ECS Meeting, The Elctrochemical Society* **2006,** *214*, Abstract #27.

29. Kojima, A.; Teshima, K.; Shirai, Y.; Miyasaka, T., Organometal halide perovskites as visible-light sensitizers for photovoltaic cells. *J. Am. Chem. Soc.* **2009,** *131* (17), 6050-1.

30. Nazeeruddin, M. K.; Kay, A.; Rodicio, I.; Humphry-Baker, R.; Mueller, E.; Liska, P.; Vlachopoulos, N.; Graetzel, M., Conversion of light to electricity by cis-X2bis(2,2'-bipyridyl-4,4'-dicarboxylate)ruthenium(II) charge-transfer sensitizers (X = Cl-, Br-, I-, CN-, and SCN-) on nanocrystalline titanium dioxide electrodes. *J. Am. Chem. Soc.* **1993,** *115* (14), 6382-6390.

31.   Bach, U.; Lupo, D.; Comte, P.; Moser, J. E.; Weissortel, F.; Salbeck, J.; Spreitzer, H.; Gratzel, M., Solid-state dye-sensitized mesoporous TiO2 solar cells with high photon-to-electron conversion efficiencies. *Nature* **1998,** *395* (6702), 583-585.

32.   Li, C.; Wei, J.; Sato, M.; Koike, H.; Xie, Z.-Z.; Li, Y.-Q.; Kanai, K.; Kera, S.; Ueno, N.; Tang, J.-X., Halide-Substituted Electronic Properties of Organometal Halide Perovskite Films: Direct and Inverse Photoemission Studies. *ACS Appl. Mater. Interfaces* **2016,** *8* (18), 11526-11531.

33.   Park, B. W.; Philippe, B.; Jain, S. M.; Zhang, X. L.; Edvinsson, T.; Rensmo, H.; Zietz, B.; Boschloo, G., Chemical engineering of methylammonium lead iodide/bromide perovskites: tuning of opto-electronic properties and photovoltaic performance. *J. Mater. Chem. A* **2015,** *3* (43), 21760-21771.

34.   Ameen, S.; Rub, M. A.; Kosa, S. A.; Alamry, K. A.; Akhtar, M. S.; Shin, H.-S.; Seo, H.-K.; Asiri, A. M.; Nazeeruddin, M. K., Perovskite Solar Cells: Influence of Hole Transporting Materials on Power Conversion Efficiency. *ChemSusChem* **2016,** *9* (1), 10-27.

35.   Burschka, J.; Pellet, N.; Moon, S. J.; Humphry-Baker, R.; Gao, P.; Nazeeruddin, M. K.; Gratzel, M., Sequential deposition as a route to high-performance perovskite-sensitized solar cells. *Nature* **2013,** *499* (7458), 316-9.

36.   Jeon, N. J.; Noh, J. H.; Kim, Y. C.; Yang, W. S.; Ryu, S.; Il Seol, S., Solvent engineering for high-performance inorganic-organic hybrid perovskite solar cells. *Nat. Mater.* **2014,** *13* (9), 897-903.

37.   Jeon, N. J.; Noh, J. H.; Yang, W. S.; Kim, Y. C.; Ryu, S.; Seo, J.; Seok, S. I., Compositional engineering of perovskite materials for high-performance solar cells. *Nature* **2015,** *517* (7535), 476-480.

38.   Saliba, M.; Matsui, T.; Seo, J.-Y.; Domanski, K.; Correa-Baena, J.-P.; Nazeeruddin, M. K.; Zakeeruddin, S. M.; Tress, W.; Abate, A.; Hagfeldt, A.; Gratzel, M., Cesium-containing triple cation perovskite solar cells: improved stability, reproducibility and high efficiency. *Energy Environ. Sci.* **2016,** *9* (6), 1989-1997.

39.   Saragi, T. P.; Spehr, T.; Siebert, A.; Fuhrmann-Lieker, T.; Salbeck, J., Spiro compounds for organic optoelectronics. *Chem. Rev.* **2007,** *107* (4), 1011-1065.

40.   Facci, J. S.; Stolka, M., Redox Migration Mechanism of Charge Transport in Molecularly Doped Polymers. *Philosophical Magazine B-Physics of Condensed Matter Statistical Mechanics Electronic Optical and Magnetic Properties* **1986,** *54* (1), 1-18.

41.   Stolka, M.; Yanus, J. F.; Pai, D. M., Hole Transport in Solid-Solutions of a Diamine in Polycarbonate. *J. Phys. Chem.* **1984,** *88* (20), 4707-4714.

42.   Salbeck, J.; Weissortel, F.; Bauer, J., Spiro linked compounds for use as active materials in organic light emitting diodes. *Macromolecular Symposia* **1998,** *125* (1), 121-132.

43.   Salbeck, J.; Yu, N.; Bauer, J.; Weissortel, F.; Bestgen, H., Low molecular organic glasses for blue electroluminescence. *Synth. Met.* **1997,** *91* (1-3), 209-215.

44.   Calio, L.; Kazim, S.; Gratzel, M.; Ahmad, S., Hole-Transport Materials for Perovskite Solar Cells. *Angew. Chem. Int. Ed.* **2016,** *55* (47), 14522-14545.

45.   Docampo, P.; Guldin, S.; Leijtens, T.; Noel, N. K.; Steiner, U.; Snaith, H. J., Lessons learned: from dye-sensitized solar cells to all-solid-state hybrid devices. *Adv. Mater.* **2014,** *26* (24), 4013-30.

46.   Burschka, J.; Dualeh, A.; Kessler, F.; Baranoff, E.; Cevey-Ha, N.-L.; Yi, C.; Nazeeruddin, M. K.; Grätzel, M., Tris(2-(1H-pyrazol-1-yl)pyridine)cobalt(III) as p-Type Dopant for Organic Semiconductors and Its Application in Highly Efficient Solid-State Dye-Sensitized Solar Cells. *J. Am. Chem. Soc.* **2011,** *133* (45), 18042-18045.

47.   Ye, M. D.; Hong, X. D.; Zhang, F. Y.; Liu, X. Y., Recent advancements in perovskite solar cells: flexibility, stability and large scale. *J. Mater. Chem. A* **2016,** *4* (18), 6755-6771.

48.   Xiao, J.; Zhang, H. L., Recent Progress in Organic-Inorganic Hybrid Perovskite Materials for Luminescence Applications. *Acta Physico-Chimica Sinica* **2016,** *32* (8), 1894-1912.

49.   Kim, H.-S.; Seo, J.-Y.; Park, N.-G., Material and Device Stability in Perovskite Solar Cells. *ChemSusChem* **2016,** *9* (18), 2528-2540.

50.   Green, M. A.; Ho-Baillie, A.; Snaith, H. J., The emergence of perovskite solar cells. *Nat. Photonics* **2014,** *8* (7), 506-514.

51.   Brenner, T. M.; Egger, D. A.; Kronik, L.; Hodes, G.; Cahen, D., Hybrid organic—inorganic perovskites: low-cost semiconductors with intriguing charge-transport properties. *Nat. Rev. Mater.* **2016,** *1* (1), 15007.

52.   Stranks, S. D.; Eperon, G. E.; Grancini, G.; Menelaou, C.; Alcocer, M. J.; Leijtens, T.; Herz, L. M.; Petrozza, A.; Snaith, H. J., Electron-hole diffusion lengths exceeding 1 micrometer in an organometal trihalide perovskite absorber. *Science* **2013,** *342* (6156), 341-4.

53.   Xing, G.; Mathews, N.; Sun, S.; Lim, S. S.; Lam, Y. M.; Gratzel, M.; Mhaisalkar, S.; Sum, T. C., Long-range balanced electron- and hole-transport lengths in organic-inorganic $CH_3NH_3PbI_3$. *Science* **2013,** *342* (6156), 344-7.

54.   Miyata, A.; Mitioglu, A.; Plochocka, P.; Portugall, O.; Wang, J. T.-W.; Stranks, S. D.; Snaith, H. J.; Nicholas, R. J., Direct measurement of the exciton binding energy and effective masses for charge carriers in organic-inorganic tri-halide perovskites. *Nat. Phys.* **2015,** *11* (7), 582-587.

55.   Yin, W.-J.; Yang, J.-H.; Kang, J.; Yan, Y.; Wei, S.-H., Halide perovskite materials for solar cells: a theoretical review. *J. Mater. Chem. A* **2015,** *3* (17), 8926-8942.

56.   Yin, W.-J.; Shi, T.; Yan, Y., Unusual defect physics in $CH_3NH_3PbI_3$ perovskite solar cell absorber. *Appl. Phys. Lett.* **2014,** *104* (6), 063903.

57.   Yin, W.-J.; Shi, T.; Yan, Y., Unique Properties of Halide Perovskites as Possible Origins of the Superior Solar Cell Performance. *Adv. Mater.* **2014,** *26* (27), 4653-+.

58.   Game, O.; Singh, U.; Kumari, T.; Banpurkar, A.; Ogale, S., ZnO(N)-Spiro-MeOTAD hybrid photodiode: an efficient self-powered fast-response UV (visible) photosensor. *Nanoscale* **2014,** *6* (1), 503-513.

59.   Bera, A.; Das Mahapatra, A.; Mondal, S.; Basak, D., Sb_2S_3/Spiro-OMeTAD Inorganic– Organic Hybrid p–n Junction Diode for High Performance Self-Powered Photodetector. *ACS Appl. Mater. Interfaces* **2016,** *8* (50), 34506-34512.

60.   Enright, B.; Redmond, G.; Fitzmaurice, D., Spectroscopic determination of flatband potentials for polycrystalline TiO2 electrodes in mixed solvent systems. *J. Phys. Chem.* **1994,** *98* (24), 6195-6200.

61.   Snaith, H. J.; Grätzel, M., Enhanced charge mobility in a molecular hole transporter via addition of redox inactive ionic dopant: Implication to dye-sensitized solar cells. *Appl. Phys. Lett.* **2006,** *89* (26), 262114.

62.   Arkhipov, V. I.; Heremans, P.; Emelianova, E. V.; Bassler, H., Effect of doping on the density-of-states distribution and carrier hopping in disordered organic semiconductors. *Phys. Rev. B* **2005,** *71* (4), 045214.

63.   Arkhipov, V. I.; Emelianova, E. V.; Heremans, P.; Bassler, H., Analytic model of carrier mobility in doped disordered organic semiconductors. *Phys. Rev. B* **2005,** *72* (23), 235202.

64.   Shimotani, H.; Diguet, G.; Iwasa, Y., Direct comparison of field-effect and electrochemical doping in regioregular poly (3-hexylthiophene). *Appl. Phys. Lett.* **2005,** *86* (2), 022104.

65.   Schölin, R.; Karlsson, M. H.; Eriksson, S. K.; Siegbahn, H.; Johansson, E. M. J.; Rensmo, H., Energy Level Shifts in Spiro-OMeTAD Molecular Thin Films When Adding Li-TFSI. *J. Phys. Chem. C* **2012,** *116* (50), 26300-26305.

66.   Hawash, Z.; Ono, L. K.; Raga, S. R.; Lee, M. V.; Qi, Y. B., Air-Exposure Induced Dopant Redistribution and Energy Level Shifts in Spin-Coated Spiro-MeOTAD Films. *Chem. Mater.* **2015,** *27* (2), 562-569.

67.   Hagen, J.; Schaffrath, W.; Otschik, P.; Fink, R.; Bacher, A.; Schmidt, H. W.; Haarer, D., Novel hybrid solar cells consisting of inorganic nanoparticles and an organic hole transport material. *Synth. Met.* **1997,** *89* (3), 215-220.

68.   Liu, M.; Johnston, M. B.; Snaith, H. J., Efficient planar heterojunction perovskite solar cells by vapour deposition. *Nature* **2013,** *501* (7467), 395-8.

69.   Burschka, J.; Dualeh, A.; Kessler, F.; Baranoff, E.; Cevey-Ha, N. L.; Yi, C.; Nazeeruddin, M. K.; Gratzel, M., Tris(2-(1H-pyrazol-1-yl)pyridine)cobalt(III) as p-type dopant for organic semiconductors and its application in highly efficient solid-state dye-sensitized solar cells. *Journal of the American Chemical Society* **2011,** *133* (45), 18042-5.

70.   Snaith, H. J.; Moule, A. J.; Klein, C.; Meerholz, K.; Friend, R. H.; Grätzel, M., Efficiency Enhancements in Solid-State Hybrid Solar Cells via Reduced Charge Recombination and Increased Light Capture. *Nano Lett.* **2007,** *7* (11), 3372-3376.

71.   Dewalque, J.; Colson, P.; Thalluri, G. K. V. V.; Mathis, F.; Chêne, G.; Cloots, R.; Henrist, C., Pore-filling of Spiro-OMeTAD determined by Rutherford backscattering spectrometry in templated TiO_2 photoelectrodes. *Org. Electron.* **2014,** *15* (1), 9-15.

72.   Ariga, K.; Yamauchi, Y.; Rydzek, G.; Ji, Q.; Yonamine, Y.; Wu, K. C. W.; Hill, J. P., Layer-by-layer Nanoarchitectonics: Invention, Innovation, and Evolution. *Chem. Lett.* **2014,** *43* (1), 36-68.

73.   Wang, M. K.; Moon, S. J.; Zhou, D. F.; Le Formal, F.; Cevey-Ha, N. L.; Humphry-Baker, R.; Gratzel, C.; Wang, P.; Zakeeruddin, S. M.; Gratzel, M., Enhanced-Light-Harvesting Amphiphilic Ruthenium Dye for Efficient Solid-State Dye-Sensitized Solar Cells. *Adv. Funct. Mater.* **2010,** *20* (11), 1821-1826.

74.   Bi, D.; Yang, L.; Boschloo, G.; Hagfeldt, A.; Johansson, E. M. J., Effect of Different Hole Transport Materials on Recombination in $CH_3NH_3PbI_3$ Perovskite-Sensitized Mesoscopic Solar Cells. *J. Phys. Chem. Lett.* **2013,** *4* (9), 1532-1536.

75.   Kruger, J.; Plass, R.; Cevey, L.; Piccirelli, M.; Gratzel, M.; Bach, U., High efficiency solid-state photovoltaic device due to inhibition of interface charge recombination. *Appl. Phys. Lett.* **2001,** *79* (13), 2085-2087.

76.   Calvert, P., Inkjet printing for materials and devices. *Chem. Mater.* **2001,** *13* (10), 3299-3305.

77.   Veinot, J. G. C.; Marks, T. J., Toward the ideal organic light-emitting diode. The versatility and utility of interfacial tailoring by cross-linked siloxane interlayers. *Acc. Chem. Res.* **2005,** *38* (8), 632-643.

78.   Jolt Oostra, A.; Blom, P. W. M.; Michels, J. J., Prevention of short circuits in solution-processed OLED devices. *Org. Electron.* **2014,** *15* (6), 1166-1172.

79.   Abate, A.; Leijtens, T.; Pathak, S.; Teuscher, J.; Avolio, R.; Errico, M. E.; Kirkpatrik, J.; Ball, J. M.; Docampo, P.; McPherson, I.; Snaith, H. J., Lithium salts as "redox active" p-type dopants for organic semiconductors and their impact in solid-state dye-sensitized solar cells. *Phys. Chem. Chem. Phys.* **2013,** *15* (7), 2572-9.

80.   Ono, L. K.; Schulz, P.; Endres, J. J.; Nikiforov, G. O.; Kato, Y.; Kahn, A.; Qi, Y. B., Air-Exposure-Induced Gas-Molecule Incorporation into Spiro-MeOTAD Films. *J. Phys. Chem. Lett.* **2014,** *5* (8), 1374-1379.

81.   Hock, R.; Mayer, T.; Jaegermann, W., p-Type Doping of Spiro-MeOTAD with WO_3 and the Spiro-MeOTAD/WO_3Interface Investigated by Synchrotron-Induced Photoelectron Spectroscopy. *J. Phys. Chem. C* **2012,** *116* (34), 18146-18154.

82.   Ng, T.-W.; Chan, C.-Y.; Yang, Q.-D.; Wei, H.-X.; Lo, M.-F.; Roy, V. A. L.; Zhang, W.-J.; Lee, C.-S., Charge interaction and interfacial electronic structures in a solid-state dye-sensitized solar cell. *Org. Electron.* **2013,** *14* (11), 2743-2747.

83.   Chen, D. Y.; Tseng, W. H.; Liang, S. P.; Wu, C. I.; Hsu, C. W.; Chi, Y.; Hung, W. Y.; Chou, P. T., Application of F4TCNQ doped spiro-MeOTAD in high performance solid state dye sensitized solar cells. *Phys. Chem. Chem. Phys.* **2012,** *14* (33), 11689-94.

84.   Burschka, J.; Kessler, F.; Nazeeruddin, M. K.; Graetzel, M., Co(III) Complexes as p-Dopants in Solid-State Dye-Sensitized Solar Cells. *Chem. Mater.* **2013,** *25* (15), 2986-2990.

85.   Nguyen, W. H.; Bailie, C. D.; Unger, E. L.; McGehee, M. D., Enhancing the Hole-Conductivity of Spiro-OMeTAD without Oxygen or Lithium Salts by Using Spiro(TFSI)(2) in Perovskite and Dye-Sensitized Solar Cells. *J. Am. Chem. Soc.* **2014,** *136* (31), 10996-11001.

86.   Fantacci, S.; De Angelis, F.; Nazeeruddin, M. K.; Grätzel, M., Electronic and Optical Properties of the Spiro-MeOTAD Hole Conductor in Its Neutral and Oxidized Forms: A DFT/TDDFT Investigation. *J. Phys. Chem. C* **2011,** *115* (46), 23126-23133.

87.   Cappel, U. B.; Daeneke, T.; Bach, U., Oxygen-induced doping of spiro-MeOTAD in solid-state dye-sensitized solar cells and its impact on device performance. *Nano Lett.* **2012,** *12* (9), 4925-31.

88.   Yang, L.; Xu, B.; Bi, D.; Tian, H.; Boschloo, G.; Sun, L.; Hagfeldt, A.; Johansson, E. M., Initial light soaking treatment enables hole transport material to outperform spiro-OMeTAD in solid-state dye-sensitized solar cells. *J. Am. Chem. Soc.* **2013,** *135* (19), 7378-85.

89.   Jorgensen, M.; Norrman, K.; Krebs, F. C., Stability/degradation of polymer solar cells. *Sol. Energy Mater. Sol. Cells* **2008,** *92* (7), 686-714.

90.   Shirley, D. A., High-Resolution X-Ray Photoemission Spectrum of the Valence Bands of Gold. *Phys. Rev. B* **1972,** *5* (12), 4709-4714.

91.   Gilman, J. B.; Eliason, T. L.; Fast, A.; Vaida, V., Selectivity and stability of organic films at the air-aqueous interface. *J. Colloid Interface Sci.* **2004,** *280* (1), 234-43.

92.   Schulz, P.; Edri, E.; Kirmayer, S.; Hodes, G.; Cahen, D.; Kahn, A., Interface energetics in organo-metal halide perovskite-based photovoltaic cells. *Energy Environ. Sci.* **2014,** *7* (4), 1377.

93.   Dedryvere, R.; Leroy, S.; Martinez, H.; Blanchard, F.; Lemordant, D.; Gonbeau, D., XPS valence characterization of lithium salts as a tool to study electrode/electrolyte interfaces of Li-ion batteries. *J. Phys. Chem. B* **2006,** *110* (26), 12986-12992.

94.   Scofield, J. H., Hartree-Slater Subshell Photoionization Cross-Sections at 1254 and 1487ev. *J. Electron. Spectrosc. Relat. Phenom.* **1976,** *8* (2), 129-137.

95.   Ensling, D.; Stjerndahl, M.; Nyten, A.; Gustafsson, T.; Thomas, J. O., A comparative XPS surface study of Li_2FeSiO_4/C cycled with LiTFSI- and $LiPF_6$-based electrolytes. *J. Mater. Chem.* **2009,** *19* (1), 82-88.

96.   Du, P.; Lu, J.; Lau, K. C.; Luo, X.; Bareno, J.; Zhang, X.; Ren, Y.; Zhang, Z.; Curtiss, L. A.; Sun, Y. K.; Amine, K., Compatibility of lithium salts with solvent of the non-aqueous electrolyte in $Li-O_2$ batteries. *Phys. Chem. Chem. Phys.* **2013,** *15* (15), 5572-81.

97.   Tak, Y.; Park, D.; Yong, K., Characterization of ZnO nanorod arrays fabricated on Si wafers using a low-temperature synthesis method. *J. Vac. Sci. Technol. B* **2006,** *24* (4), 2047-2052.

98.   Tanaka, K.; Miyahara, K.; Toyoshima, I., Adsorption of Co2 on Tio2 and Pt/Tio2 Studied by X-Ray Photoelectron-Spectroscopy and Auger-Electron Spectroscopy. *J. Phys. Chem.* **1984,** *88* (16), 3504-3508.

99.   Carley, A. F.; Hawkins, G.; Read, S.; Roberts, M. W., Reactions of co-adsorbed carbon dioxide and dioxygen at the Mg(0001) surface at low temperatures. *Top. Catal.* **1999,** *8* (3-4), 243-248.

100.   Hawash, Z.; Ono, L. K.; Qi, Y. B., Moisture and Oxygen Enhance Conductivity of LiTFSI-Doped Spiro-MeOTAD Hole Transport Layer in Perovskite Solar Cells. *Adv. Mater. Interfaces* **2016,** *3* (13), 1600117.

101.   Krüger, J.; Plass, R.; Cevey, L.; Piccirelli, M.; Grätzel, M.; Bach, U., High efficiency solid-state photovoltaic device due to inhibition of interface charge recombination. *Appl. Phys. Lett.* **2001,** *79* (13), 2085.

102.   O'Regan, B. C.; Barnes, P. R. F.; Li, X.; Law, C.; Palomares, E.; Marin-Beloqui, J. M., Optoelectronic Studies of Methylammonium Lead Iodide Perovskite Solar Cells with Mesoporous TiO_2: Separation of Electronic and Chemical Charge Storage, Understanding Two Recombination Lifetimes, and the Evolution of Band Offsets during J–V Hysteresis. *J. Am. Chem. Soc.* **2015,** *137* (15), 5087-5099.

103.   Wojciechowski, K.; Saliba, M.; Leijtens, T.; Abate, A.; Snaith, H. J., Sub-150 °C processed meso-superstructured perovskite solar cells with enhanced efficiency. *Energy Environ. Sci.* **2014,** *7* (3), 1142.

104.   Heo, J. H.; Im, S. H.; Noh, J. H.; Mandal, T. N.; Lim, C.-S.; Chang, J. A.; Lee, Y. H.; Kim, H.-j.; Sarkar, A.; NazeeruddinMd, K.; Gratzel, M.; Seok, S. I., Efficient inorganic-organic hybrid heterojunction solar cells containing perovskite compound and polymeric hole conductors. *Nat. Photonics* **2013,** *7* (6), 486-491.

105.   Yang, W. S.; Noh, J. H.; Jeon, N. J.; Kim, Y. C.; Ryu, S.; Seo, J.; Seok, S. I., High-performance photovoltaic perovskite layers fabricated through intramolecular exchange. *Science* **2015,** *348* (6240), 1234-1237.

106.   Guo, Y.; Liu, C.; Inoue, K.; Harano, K.; Tanaka, H.; Nakamura, E., Enhancement in the efficiency of an organic-inorganic hybrid solar cell with a doped P3HT hole-transporting layer on a void-free perovskite active layer. *J. Mater. Chem. A* **2014,** *2* (34), 13827-13830.

107.   Heo, J. H.; Im, S. H., CH$_3$NH$_3$PbI$_3$/poly-3-hexylthiophen perovskite mesoscopic solar cells: Performance enhancement by Li-assisted hole conduction. *Phys. Status Solidi RRL* **2014,** *8* (10), 816-821.

108.   Ryu, S.; Noh, J. H.; Jeon, N. J.; Chan Kim, Y.; Yang, W. S.; Seo, J.; Seok, S. I., Voltage output of efficient perovskite solar cells with high open-circuit voltage and fill factor. *Energy Environ. Sci.* **2014,** *7* (8), 2614.

109.   Du, Y.; Cai, H.; Ni, J.; Li, J.; Yu, H.; Sun, X.; Wu, Y.; Wen, H.; Zhang, J., Air-processed, efficient CH$_3$NH$_3$PbI$_{3-x}$Cl$_x$ perovskite solar cells with organic polymer PTB7 as a hole-transport layer. *RSC Adv.* **2015,** *5* (82), 66981-66987.

110.   Rong, Y.; Liu, L.; Mei, A.; Li, X.; Han, H., Beyond Efficiency: the Challenge of Stability in Mesoscopic Perovskite Solar Cells. *Adv. Energy Mater.* **2015,** *5* (20), 1501066.

111.   Leijtens, T.; Eperon, G. E.; Noel, N. K.; Habisreutinger, S. N.; Petrozza, A.; Snaith, H. J., Stability of Metal Halide Perovskite Solar Cells. *Adv. Energy Mater.* **2015,** *5* (20), 1500963.

112.   Kato, Y.; Ono, L. K.; Lee, M. V.; Wang, S.; Raga, S. R.; Qi, Y. B., Silver Iodide Formation in Methyl Ammonium Lead Iodide Perovskite Solar Cells with Silver Top Electrodes. *Adv. Mater. Interfaces* **2015,** *2* (13), 1500195.

113.   Ono, L. K.; Raga, S. R.; Remeika, M.; Winchester, A. J.; Gabe, A.; Qi, Y. B., Pinhole-free hole transport layers significantly improve the stability of MAPbI$_3$-based perovskite solar cells under operating conditions. *J. Mater. Chem. A* **2015,** *3* (30), 15451-15456.

114.   Liu, J.; Wu, Y.; Qin, C.; Yang, X.; Yasuda, T.; Islam, A.; Zhang, K.; Peng, W.; Chen, W.; Han, L., A dopant-free hole-transporting material for efficient and stable perovskite solar cells. *Energy Environ. Sci.* **2014,** *7* (9), 2963-2967.

115.   Mei, A.; Li, X.; Liu, L.; Ku, Z.; Liu, T.; Rong, Y.; Xu, M.; Hu, M.; Chen, J.; Yang, Y.; Gratzel, M.; Han, H., A hole-conductor-free, fully printable mesoscopic perovskite solar cell with high stability. *Science* **2014,** *345* (6194), 295-8.

116.   Wang, S.; Yuan, W.; Meng, Y. S., Spectrum-Dependent Spiro-OMeTAD Oxidization Mechanism in Perovskite Solar Cells. *ACS Appl. Mater. Interfaces* **2015,** *7* (44), 24791-24798.

117.   Chen, W.; Wu, Y. Z.; Yue, Y. F.; Liu, J.; Zhang, W. J.; Yang, X. D.; Chen, H.; Bi, E. B.; Ashraful, I.; Gratzel, M.; Han, L. Y., Efficient and stable large-area perovskite solar cells with inorganic charge extraction layers. *Science* **2015,** *350* (6263), 944-948.

118.   Dualeh, A.; Moehl, T.; Tétreault, N.; Teuscher, J.; Gao, P.; Nazeeruddin, M. K.; Grätzel, M., Impedance Spectroscopic Analysis of Lead Iodide Perovskite-Sensitized Solid-State Solar Cells. *ACS Nano* **2014,** *8* (1), 362-373.

119.   Jena, A. K.; Chen, H.-W.; Kogo, A.; Sanehira, Y.; Ikegami, M.; Miyasaka, T., The Interface between FTO and the TiO_2 Compact Layer Can Be One of the Origins to Hysteresis in Planar Heterojunction Perovskite Solar Cells. *ACS Appl. Mater. Interfaces* **2015,** *7* (18), 9817-9823.

120.   Liao, H.-H.; Yang, C.-M.; Liu, C.-C.; Horng, S.-F.; Meng, H.-F.; Shy, J.-T., Dynamics and reversibility of oxygen doping and de-doping for conjugated polymer. *J. Appl. Phys.* **2008,** *103* (10), 104506.

121.   Qi, Y. B.; Sajoto, T.; Kröger, M.; Kandabarow, A. M.; Park, W.; Barlow, S.; Kim, E.-G.; Wielunski, L.; Feldman, L. C.; Bartynski, R. A.; Brédas, J.-L.; Marder, S. R.; Kahn, A., A Molybdenum Dithiolene Complex as p-Dopant for Hole-Transport Materials: A

Multitechnique Experimental and Theoretical Investigation. *Chem. Mater.* **2010,** *22* (2), 524-531.

122.   Qi, Y. B.; Sajoto, T.; Barlow, S.; Kim, E.-G.; Brédas, J.-L.; Marder, S. R.; Kahn, A., Use of a High Electron-Affinity Molybdenum Dithiolene Complex to p-Dope Hole-Transport Layers. *J. Am. Chem. Soc.* **2009,** *131* (35), 12530-12531.

123.   Gao, W. Y.; Kahn, A., Controlled p doping of the hole-transport molecular material N,N '-diphenyl-N,N '-bis(1-naphthyl)-1,1(')-biphenyl-4,4 '-diamine with tetrafluorotetracyanoquinodimethane. *J. Appl. Phys.* **2003,** *94* (1), 359-366.

124.   Gao, W. Y.; Kahn, A., Controlled p-doping of zinc phthalocyanine by coevaporation with tetrafluorotetracyanoquinodimethane: A direct and inverse photoemission study. *Appl. Phys. Lett.* **2001,** *79* (24), 4040-4042.

125.   Poplavskyy, D.; Nelson, J., Nondispersive hole transport in amorphous films of methoxy-spirofluorene-arylamine organic compound. *J. Appl. Phys.* **2003,** *93* (1), 341-346.

126.   Qi, Y. B.; Mohapatra, S. K.; Kim, S. B.; Barlow, S.; Marder, S. R.; Kahn, A., Solution doping of organic semiconductors using air-stable n-dopants. *Appl. Phys. Lett.* **2012,** *100* (8).

127.   Anthopoulos, T. D.; Anyfantis, G. C.; Papavassiliou, G. C.; de Leeuw, D. M., Air-stable ambipolar organic transistors. *Appl. Phys. Lett.* **2007,** *90* (12), 122105.

128.   de Leeuw, D. M.; Simenon, M. M. J.; Brown, A. R.; Einerhand, R. E. F., Stability of n-type doped conducting polymers and consequences for polymeric microelectronic devices. *Synth. Met.* **1997,** *87* (1), 53-59.

129.   Yoo, S.-J.; Kim, J.-J., Charge Transport in Electrically Doped Amorphous Organic Semiconductors. *Macromol. Rapid Commun.* **2015,** *36* (11), 984-1000.

130.   Seemann, A.; Egelhaaf, H. J.; Brabec, C. J.; Hauch, J. A., Influence of oxygen on semi-transparent organic solar cells with gas permeable electrodes. *Org. Electron.* **2009,** *10* (8), 1424-1428.

131.   Song, Q. L.; Wang, M. L.; Obbard, E. G.; Sun, X. Y.; Ding, X. M.; Hou, X. Y.; Li, C. M., Degradation of small-molecule organic solar cells. *Appl. Phys. Lett.* **2006,** *89* (25), 251118.

132.   Hawash, Z.; Raga, S. R.; Son, D.-Y.; Ono, L. K.; Park, N.-G.; Qi, Y. B., Interfacial Modification of Perovskite Solar Cells Using an Ultrathin MAI Layer Leads to Enhanced Energy Level Alignment, Efficiencies, and Reproducibility. *J. Phys. Chem. Lett.* **2017,** *8* (17), 3947-3953.

133.   Ono, L. K.; Qi, Y. B., Surface and Interface Aspects of Organometal Halide Perovskite Materials and Solar Cells. *J. Phys. Chem. Lett.* **2016,** *7* (22), 4764-4794.

134.   Miller, E. M.; Zhao, Y.; Mercado, C. C.; Saha, S. K.; Luther, J. M.; Zhu, K.; Stevanovic, V.; Perkins, C. L.; van de Lagemaat, J., Substrate-controlled band positions in $CH_3NH_3PbI_3$ perovskite films. *Phys. Chem. Chem. Phys.* **2014,** *16* (40), 22122-22130.

135.   Olthof, S.; Meerholz, K., Substrate-dependent electronic structure and film formation of $MAPbI_3$ perovskites. *Sci. Rep.* **2017,** *7*, 40267.

136.   Li, L.; Liu, X. L.; Lyu, L.; Wu, R. S.; Liu, P.; Zhang, Y. H.; Zhao, Y.; Wang, H. Y.; Niu, D. M.; Yang, J. L.; Gao, Y. L., Modification of Ultrathin NPB Interlayer on the Electronic Structures of the $CH_3NH_3PbI_3$/NPB/MoO_3 Interface. *J. Phys. Chem. C* **2016,** *120* (32), 17863-17871.

137.   Olthof, S., Research Update: The electronic structure of hybrid perovskite layers and their energetic alignment in devices. *Apl Mater.* **2016,** *4* (9), 091502.

138.   Wang, Q.; Shao, Y.; Xie, H.; Lyu, L.; Liu, X.; Gao, Y.; Huang, J., Qualifying composition dependent p and n self-doping in $CH_3NH_3PbI_3$. *Appl. Phys. Lett.* **2014,** *105* (16), 163508.

139.   Emara, J.; Schnier, T.; Pourdavoud, N.; Riedl, T.; Meerholz, K.; Olthof, S., Impact of Film Stoichiometry on the Ionization Energy and Electronic Structure of $CH_3NH_3PbI_3$ Perovskites. *Adv. Mater.* **2016,** *28* (3), 553-559.

140.   Cheng, Y.; Li, H.-W.; Zhang, J.; Yang, Q.-D.; Liu, T.; Guan, Z.; Qing, J.; Lee, C.-S.; Tsang, S.-W., Spectroscopic study on the impact of methylammonium iodide loading time on the electronic properties in perovskite thin films. *J. Mater. Chem. A* **2016,** *4* (2), 561-567.

141.   Son, D.-Y.; Lee, J.-W.; Choi, Y. J.; Jang, I.-H.; Lee, S.; Yoo, P. J.; Shin, H.; Ahn, N.; Choi, M.; Kim, D.; Park, N.-G., Self-formed grain boundary healing layer for highly efficient $CH_3 NH_3 PbI_3$ perovskite solar cells. *Nat. Energy* **2016,** *1*, 16081.

142.   Cohen, B.-E.; Gamliel, S.; Etgar, L., Parameters influencing the deposition of methylammonium lead halide iodide in hole conductor free perovskite-based solar cells. *Apl Mater.* **2014,** *2* (8), 081502.

143.   Roldan-Carmona, C.; Gratia, P.; Zimmermann, I.; Grancini, G.; Gao, P.; Graetzel, M.; Nazeeruddin, M. K., High efficiency methylammonium lead triiodide perovskite solar cells: the relevance of non-stoichiometric precursors. *Energy Environ. Sci.* **2015,** *8* (12), 3550-3556.

144.   Jacobsson, T. J.; Correa-Baena, J.-P.; Halvani Anaraki, E.; Philippe, B.; Stranks, S. D.; Bouduban, M. E. F.; Tress, W.; Schenk, K.; Teuscher, J.; Moser, J.-E.; Rensmo, H.; Hagfeldt, A., Unreacted PbI_2 as a Double-Edged Sword for Enhancing the Performance of Perovskite Solar Cells. *J. Am. Chem. Soc.* **2016,** *138* (32), 10331-10343.

145.   Ahn, N.; Son, D. Y.; Jang, I. H.; Kang, S. M.; Choi, M.; Park, N. G., Highly Reproducible Perovskite Solar Cells with Average Efficiency of 18.3% and Best Efficiency of 19.7% Fabricated via Lewis Base Adduct of Lead(II) Iodide. *J. Am. Chem. Soc.* **2015,** *137* (27), 8696-8699.

146.   Lee, J. W.; Kim, H. S.; Park, N. G., Lewis Acid-Base Adduct Approach for High Efficiency Perovskite Solar Cells. *Acc. Chem. Res.* **2016,** *49* (2), 311-319.

147.   Malinkiewicz, O.; Yella, A.; Lee, Y. H.; Minguez Espallargas, G.; Graetzel, M.; Nazeeruddin, M. K.; Bolink, H. J., Perovskite solar cells employing organic charge-transport layers. *Nat. Photonics* **2014,** *8* (2), 128-132.

148.   Ono, L. K.; Wang, S.; Kato, Y.; Raga, S. R.; Qi, Y. B., Fabrication of semi-transparent perovskite films with centimeter-scale superior uniformity by the hybrid deposition method. *Energy Environ. Sci.* **2014**.

149.   Kim, T. G.; Seo, S. W.; Kwon, H.; Hahn, J.; Kim, J. W., Influence of halide precursor type and its composition on the electronic properties of vacuum deposited perovskite films. *Phys. Chem. Chem. Phys.* **2015,** *17* (37), 24342-24348.

150.   Endres, J.; Kulbak, M.; Zhao, L. F.; Rand, B. P.; Cahen, D.; Hodes, G.; Kahn, A., Electronic structure of the $CsPbBr_3$/polytriarylamine (PTAA) system. *J. Appl. Phys.* **2017,** *121* (3).

151.   Liu, L.; McLeod, J. A.; Wang, R.; Shen, P.; Duhm, S., Tracking the formation of methylammonium lead triiodide perovskite. *Appl. Phys. Lett.* **2015,** *107* (6).

152.   Jung, M.-C.; Lee, Y. M.; Lee, H.-K.; Park, J.; Raga, S. R.; Ono, L. K.; Wang, S.; Leyden, M. R.; Yu, B. D.; Hong, S.; Qi, Y. B., The presence of CH_3NH_2 neutral species in organometal halide perovskite films. *Appl. Phys. Lett.* **2016,** *108* (7), 073901.

153.   Zhou, X.; Li, X.; Liu, Y.; Huang, F.; Zhong, D., Interface electronic properties of co-evaporated MAPbI$_3$ on ZnO (0001): In situ X-ray photoelectron spectroscopy and ultraviolet photoelectron spectroscopy study. *Appl. Phys. Lett.* **2016,** *108* (12), 121601.

154.   Zou, Y.; Meng, Q.; Mao, H. Y.; Zhu, D. B., Substrate effect on the interfacial electronic structure of thermally-evaporated CH$_3$NH$_3$PbI$_3$ perovskite layer. *Org. Electron.* **2017,** *41,* 307-314.

155.   Juarez-Perez, E. J.; Hawash, Z.; Raga, S. R.; Ono, L. K.; Qi, Y. B., Thermal degradation of CH$_3$NH$_3$PbI$_3$ perovskite into NH$_3$ and CH$_3$I gases observed by coupled thermogravimetry-mass spectrometry analysis. *Energy Environ. Sci.* **2016,** *9* (11), 3406-3410.

156.   Da, P.; Zheng, G., Tailoring interface of lead-halide perovskite solar cells. *Nano Research* **2017**, 1-27.

157.   Jung, M. C.; Raga, S. R.; Ono, L. K.; Qi, Y. B., Substantial improvement of perovskite solar cells stability by pinhole-free hole transport layer with doping engineering. *Sci. rep.* **2015,** *5,* 9863.

List of Publications during PhD at OIST

[8]   **Hawash, Z.**†; Ono, L. K.†; Qi, Y. B.,* Recent Advances in Spiro-MeOTAD Hole Transport Material and Its Applications in Organic-inorganic Halide Perovskite Solar Cells. *Adv. Mater. Interfaces,* 2017. (Accepted)

[7]   **Hawash, Z.** Ono, L. K.; Raga, S. R.; Son, D. Y.; Park, N. G.;* Qi, Y. B.,* Interfacial Modification of Perovskite Solar Cells Using an Ultrathin MAI Layer Leads to Enhanced Energy Level Alignment, Efficiencies, and Reproducibility, 2017, 3947.

[6]   Juarez-Perez, E. J.; **Hawash, Z.**; Raga, S. R.; Ono, L. K.; Qi, Y. B.,* Thermal degradation of CH3NH3PbI3 perovskite into NH_3 and CH_3I gases observed by coupled thermogravimetry-mass spectrometry analysis. *Energy Environ. Sci.* 2016, 9, 3406.

[5]   **Hawash, Z**; Ono, L. K.; Qi, Y. B.,* Moisture and Oxygen Enhance Conductivity of LiTFSI-Doped Spiro-MeOTAD Hole Transport Layer in Perovskite Solar Cells. *Adv. Mater. Interfaces* 2016, 3, 1600117.

[4]   Juarez-Perez, E. J.; Leyden, M. R.; Wang, S.; Ono, L. K.; **Hawash, Z**.; Qi, Y. B.,* Role of the Dopants on the Morphological and Transport Properties of Spiro-MeOTAD Hole Transport Layer. *Chem. Mater.* 2016, 28, 5702.

[3]   **Hawash, Z.**; Ono, L. K.; Raga, S. R.; Lee, M. V.; Qi, Y. B.,* Air-Exposure Induced Dopant Redistribution and Energy Level Shifts in Spin-Coated Spiro-MeOTAD Films. *Chem. Mater.* 2015, 27, 562.

[2]   Singh, V.; Grammatikopoulos, P.; Cassidy, C.; Benelmekki, M.; Bohra, M.; **Hawash, Z.**;
       Baughman, K. W.; Sowwan, M.,* Assembly of Tantalum Porous Films with Graded
       Oxidation Profile from Size-Selected Nanoparticles. *J. Nanopart. Res.* 2014, 16, 2373.

[1]   Singh, V.; Cassidy, C.; Bohra, M.; Galea, A.; **Hawash, Z**; Sowwan, M.,* Surface
       Morphology of Films Grown by Size-Selected Ta Nanoparticles. *Adv. Mat. Res.* 2013, 647,
       732.